J/ψ production study at the LHCb experiment

W. Qian

LAL 10-108
Septembre 2010

THÈSE

présentée le 2 Septembre 2010 par

Wenbin Qian

pour obtenir le grade de
Docteur en sciences de l'Université Paris XI Orsay

J/ψ Production Study at the LHCb Experiment

soutenue devant la commission d'examen composée de:

M.	GAO Yuanning	Co-directeur de thèse
Mme	ROOS Lydia	Présidente
M.	ROBBE Patrick	
Mme	SCHUNE Marie-Hélène	Co-directrice de thèse
M.	SCHNEIDER Olivier	Rapporteur
M.	YUAN Changzheng	Rapporteur

博士论文

于2010年9月2日答辩

钱文斌

申请清华大学理学博士学位

J/ψ Production Study at the LHCb Experiment

LHCb实验上J/ψ粒子产生的研究

答辩委员会成员如下:

赵光达	院士	主席
陈国明	研究员	论文评阅人
陈少敏	教授	论文评阅人
高原宁	教授	指导老师
吕才典	研究员	论文评阅人
SCHNEIDER Olivier	教授	论文评阅人
SCHUNE Marie-Hélène	教授	指导老师

Contents

摘要

位于日内瓦欧洲核子中心 (CERN) 的大型强子对撞机 (LHC) 是目前世界上能量最高的质子质子加速器， 它的设计对撞能量为14 TeV，它将对现有物理理论中的许多基础问题进行研究。 LHCb 为LHC上四个大型探测实验之一，它主要用于底夸克物理的研究。 LHCb通过对含粲夸克或底夸克的强子的稀有衰变，CP破坏等的精确测量来对超出标准模型的新物理进行研究。 在实验初期LHCb上将采集大量的J/ψ粒子，这些粒子将被用于粲夸克产生的研究以解决粲偶素产生中存在的一些疑难问题。

本文基于完全模拟样本对J/ψ的产生进行研究，其中完全模拟样本是在$\sqrt{s} = 14$ TeV，$2 \times 10^{32}\,\mathrm{cm}^{-2}\mathrm{s}^{-1}$的亮度下产生的约为0.79 pb^{-1}的数据。当积累了足够的实验数据之后，我们将采用相同的方法对其进行研究。

本文首先对J/ψ离线选择条件进行优化并据此重建出双μ的不变质量谱。 我们得到J/ψ的质量分辨率约为11 MeV/c^2，在3倍分辨率区间内的信噪比可达18。 我们预期在每个pb^{-1}的数据中可以重建出6.5×10^6个J/ψ粒子。

瞬时J/ψ和从底夸克衰变来的J/ψ的反应截面将在$0 < p_T < 7$ GeV/c，$3 < \eta < 5$间的28个区间内分别进行测量。 其中我们通过定义时间变量t_z来区分瞬时J/ψ和从底夸克衰变来的J/ψ两种组分。 分析结果表明在几乎所有相空间子区间内，两种组分的反应截面的统计误差将小于10%。实验的系统误差也将在这个水平。

在对反应截面测量时我们发现J/ψ的极化对其产生测量影响很大，在某些相空间区间内可以达到30%。 为了给出更精确的测量我们有必要对J/ψ的极化进行研究。 我们通过联合拟合t_z和角度空间变量来给出两个组分的极化参数。 为了减小对模拟数据量的依赖，本文通过对似然函数的简化将整个空间的效率归结为3个效率参数，极化测量的误差由这3个效率参数和数据统计量完全决定。 基于从相同数据量的模拟数据中估计出来的效率参数，绝大多数相空间区域的瞬时J/ψ的极化参数的误差约为0.1，从

底夸克衰变来的J/ψ的误差约为0.2.

现在LHCb实验已经积累了$14\,\mathrm{nb}^{-1}$的数据，利用这些数据，我们对J/ψ进行了分析。其中有约3000个J/ψ粒子被重建出来，其质量分辨率为16 MeV/c^2，在三倍误差窗口内的信噪比约为1. 基于这些J/ψ粒子，我们给出了其产生截面随横动量变化的分布并测量了横动量在$[0, 9]$ GeV/c，y在[2.5, 4]相空间区域内的总截面为：7.6 ± 0.3 μb，这里的误差仅为统计误差。

Résumé

Le LHC (Large Hadron Collider) situé au CERN (Conseil Européen pour la Recherche Nucléaire) à Genève est le plus grand accélérateur pour la physique des particules. Les collisions proton-proton à des energies dans le centre de masse pouvant aller jusqu'à 14 TeV qui seront produites au LHC vont offrir la possibilité de s'intéresser aux questions les plus fondamentales en Physique. L'expérience LHCb est l'une des quatre expériences principales au LHC. Dédiée aux études de physique du b, le but principal de l'expérience LHCb est d'explorer d'éventuels modèles de Nouvelle Physique au-delà du Modèle Standard à travers l'étude des désintégrations rares des hadrons charmés ou beaux, et à travers des mesures de précision des observables de la violation de CP.

Même lors de sa phase de fonctionnement initial, un nombre important de J/ψ va être collecté par le détecteur LHCb et va nous permettre de réaliser des études très intéressantes sur la production du charmonium. Ces mesures pourront apporter un éclairage nouveau pour la compréhension des méchanismes de production des quarkonia dans les collisions de hadrons.

Dans cette thèse, les études de la production de J/ψ à LHCb est presentée, basée sur un échantillon d'événements Monte Carlo complétement simulés. La procédure dévelopée dans cette thèse sera utilisée pour analyser les données réelles lorsque suffisamment de statistique sera accumule.

L'analyse a été effectuée en utilisant des événements Monte Carlo générés à une énergie dans le centre de masse égale à 14 TeV, et à une luminosité de $2 \times 10^{32}\,\mathrm{cm}^{-2}\mathrm{s}^{-1}$. La taille du lot de données simulées correspond à une luminosité intégrée de 0.79 pb^{-1}. Les événements J/ψ sont reconstruits en utilisant des critères de sélection optimisés pour atteindre la meilleure discrimination contre les processus de bruit de fond. L'étude réalisée montre que $6.5{\times}10^6$ J/ψ peuvent être reconstruits par pb^{-1} de données avec une

résolution en masse de 11 MeV/c^2 et un rapport signal sur bruit $S/B \sim 18$ dans une fenêtre de masse de $\pm 3\sigma$.

La section efficace de production des J/ψ prompt et des J/ψ de désintégrations de b est mesurée dans 28 bins en p_T et η recouvrant la région $0 < p_T < 7$ GeV/c et $3 < \eta < 5$. Dans chaque bin, une variable est définie pour distinguer les J/ψ prompt de ceux de désintégrations de b. Pour 0.79 pb^{-1} de données, une précision de 10% peut être obtenue pour la majorité des bins. Les erreurs systématiques sont estimées à un niveau équivalent.

L'analyse montre également que la polarisation du J/ψ joue un rôle important dans la détermination de la section efficace. Elle peut contribuer à une erreur systématique jusqu'à 30% dans certains bins. Un tel effet peut être grandement réduit si une analyse de la polarisation du J/ψ est effectuée simultanément. La mesure des paramètres de polarisation aidera aussi grandement pour la compréhension du méchanisme de production du J/ψ. Dans le but de réduire la quantité de données simulées nécessaire pour les estimations d'efficacité, une méthode est dévelopée pour prendre en compte les efficacités 2-D par trois paramètres, et toutes les erreurs à part les erreurs statistiques ne dépendront que de ces trois paramètres. A partir des trois paramètres estimés avec les mêmes données Monte Carlo, les erreurs sur les paramètres de polarisation pour la majorité des bins sont d'environ 0.1 pour les J/ψ prompt et d'environ 0.2 pour les J/ψ de désintégrations de b.

L'expérience LHCb ayant déjà enregistré 14 nb^{-1} de données, une partie de l'analyse peut être effectuée. Environ 3000 candidats J/ψ sont reconstruits avec une résolution en masse de 16 MeV/c^2 et un rapport signal sur bruit $S/B \sim 1$ dans une fenêtre en masse de $\pm 3\sigma$. En se basant sur cet échantillon, la section efficace en fonction de p_T est mesurée. La mesure préliminaire de la section efficace des J/ψ dans la région $p_T \in [0, 9]$ GeV/c et $y \in [2.5, 4]$ est 7.6 ± 0.3 μb où seule l'erreur statistique est donnée.

Abstract

The large hadron collider (LHC) at Conseil European Pour Recherches Nucleaires (CERN) in Geneva is the largest particle physics accelerator. Proton-proton collisions up to a center-of-mass energy of 14 TeV to be produced at the LHC will offer great opportunity to address most fundamental questions in physics. The LHCb experiment is one of the four main experiments at the LHC. Dedicated to b physics studies, the primary goal of the LHCb experiment is to explore possible New Physics beyond the Standard Model through the studies of rare decays of charm and beauty-flavoured hadrons and precision measurements of CP-violating observables. Even at its first running phase, the enormous number of J/ψ particles to be collected by the LHCb detector will allow us to realize some very interesting physics studies on charmonium productions. The measurement may shed new light on the long standing puzzle in understanding the mechanism of quarkonia production in hadron-hadron collisions.

In this thesis, studies of J/ψ production at LHCb are presented based on the fully-simulated Monte Carlo events. The procedure developed in the thesis will be used to analyze real data once enough statistics are accumulated.

The study has been performed using a fully-simulated Monte Carlo sample generated at a center-of-mass energy of 14 TeV and a luminosity of $2 \times 10^{32}\,\mathrm{cm}^{-2}\mathrm{s}^{-1}$ to simulate multiple interactions. The sample size corresponds to an integrated luminosity of $0.79\ \mathrm{pb}^{-1}$. J/ψ events are reconstructed according to selection criteria optimized to achieve the best discriminating power against background processes. The study shows that $6.5{\times}10^6$ J/ψ events can be reconstructed in every pb^{-1} of data, with a mass resolution of 11 MeV/c^2 and a $S/B \sim 18$ in a $\pm 3\sigma$ mass window.

The production cross-sections of the prompt J/ψ and the J/ψ from b decays are measured in 28 bins of p_T and η covering the region of $0 < p_T < 7$ GeV/c

and $3 < \eta < 5$. In each bin, a time-like variable is defined to distinguish the prompt J/ψ mesons from those of b decays. With the 0.79 pb^{-1} of data, we can achieve a 10% precision for majority of the bins. Possible systematic errors are estimated to be at the same level.

The study also shows that the polarization of the J/ψ plays an important role in the cross-section determinations. It may contribute a systematic uncertainty up to 30% in some p_T and η bins. Such an effect can be well reduced once an analysis on the J/ψ polarization is performed simultaneously. The measurement of the polarization parameters will also help in the understanding of the J/ψ production mechanism. In order to reduce the amount of simulated data needed for the efficiency estimations, a method is developed to describe the 2-D efficiency by three parameters and all the errors except statistic errors from data will depend on the three parameters. Based on the three parameters estimated from the same Monte-Carlo data, errors on the polarization parameters for the majority of the bins are determined to be around 0.1 for the prompt J/ψ and around 0.2 for the J/ψ from b decays.

As the LHCb experiment has already collected 14 nb^{-1} of data, part of the J/ψ analysis can be performed. Around 3,000 J/ψ candidates are reconstructed with a mass resolution of 16 MeV/c^2 and a $S/B \sim 1$ in a $\pm 3\sigma$ mass window. Based on the above sample, the cross sections as a function of p_T are obtained. The preliminary cross section for J/ψ in the region $p_T \in [0, 9]$ GeV/c and $y \in [2.5, 4]$ is 7.6 ± 0.3 μb where only the statistical error is quoted.

Chapter 1

Introduction

After more than two decades of intensive work, the Large Hadron Collider (LHC) [1] achieved its first beam circulation on September 10th, 2008. Unfortunately, a problem with bus-bars of one superconducting magnet caused a helium release and resulted in a whole year's stop of LHC operation.

But now, "The LHC is back" as announced by CERN Director General Rolf Heuer on November 21st, 2009. The first beam in 2009 was injected on November 20th. Three days later, the first collisions were recorded in ATLAS (A Toroidal LHC ApparatuS) [2], CMS (The Compact Muon Solenoid) [3], ALICE (A Large Ion Collider Experiment) [4] and LHCb (The Large Hadron Collider beauty experiment) [5]. The energy of the first beam was 450 GeV and on November 30th, the LHC accelerated its two proton beams to an energy of 1.18 TeV. The first period of the LHC running finished for the Christmas break with several hundred thousands of collisions recorded in each experiment.

During this period of running, LHCb also showed great success with the detector performance. With the 550,000 collected events (35,000 collision events), it obtained very nice mass peaks for the π^0, η, K_S and Λ with mass resolutions equal to 16 ± 1 MeV/c^2, 25 ± 5 MeV/c^2, 4.1 ± 0.1 MeV/c^2, 1.4 ± 0.1 MeV/c^2 respectively. The invariant mass distributions of $\pi^+\pi^-$ and $p(\bar{p})\pi^-(\pi^+)$ are shown in Figure 1.1 and Figure 1.2 respectively. The figures show that LHCb has already understood the detector very well. But due to the small statistics collected ($\sim 7\mu\text{b}^{-1}$), there was no J/ψ candidate found in this sample.

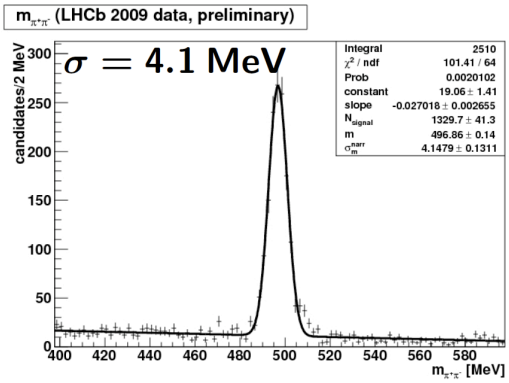

Figure 1.1: Invariant mass distribution of $\pi^+\pi^-$ for LHCb data collected in 2009, where a clear K_S mass peak is visible.

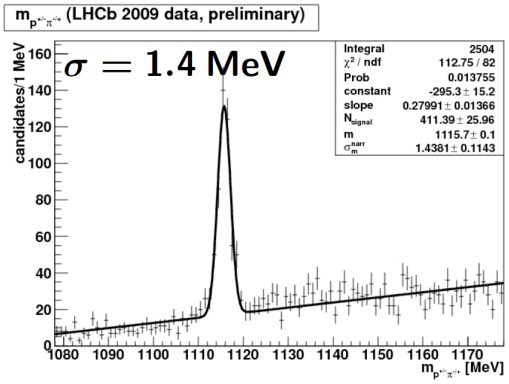

Figure 1.2: Invariant mass distribution of $p(\bar{p})\pi^-(\pi^+)$ for LHCb data collected in 2009, where a clear Λ ($\bar{\Lambda}$) mass peak is visible.

The LHC experiment restarted in March 2010. In the early morning of March 19th, both beams were accelerated to 3.5 TeV and were circulated together in the tunnel. Later on March 30th, the four detectors at the LHC observed their first collisions at $\sqrt{s} = 7$ TeV. Since then, running at $\sqrt{s} = 7$ TeV went on smoothly and with the data collected during the first 10 days, different working groups at the LHC announced their first J/ψ mass peaks on April 7th. This begins the study of J/ψ with real data. Till the end of May, LHCb has collected around 14 nb^{-1} of data with around 3,000 J/ψ reconstructed but it is not yet enough for a full analysis of the differential cross section and polarization measurements. It is foreseen that with further running in the next months, LHCb will collect enough J/ψ for various studies, like J/ψ differential cross section, polarization and b production measurements.

After the first observation of the J/ψ in 1974 [6, 7] and of the b quark in 1977 [8], the production mechanism for heavy hadrons has been studied over the last 30 years. Both the theory and the experimental knowledge improved a lot in their prediction power and measured precision. Concerning the b production, the theoretical predictions [9] now agree with the experimental results very well [10, 11, 12]. The interesting history between the interaction of the two can be found in [13]. For the J/ψ production, the results came from nearly an order of magnitude difference [14, 15, 16] to currently a very good agreement [10, 17, 18, 19, 20, 21] in the differential cross section. But for the J/ψ polarization, different theories give different polarization scenarios [17,

22, 23, 24, 25, 26] and none of them agree with the measured values [27]. This means the production mechanism of the J/ψ is not yet fully understood. Measurements at the LHC may offer further information on the production with its center-of-mass energy of $\sqrt{s} = 7$ TeV during the first two years and $\sqrt{s} = 14$ TeV in the later running. LHCb may play a special role amongst the four experiments as it covers a special acceptance region (forward region) which the other experiments cannot reach. This may further help in the understanding of the production mechanism.

Besides the theory aspects for the cross section measurement, a well measured J/ψ cross section and b-hadron cross section [1] are important for other measurements in LHCb, like absolute branching ratio measurements. The measured spectra can be used later for the Monte Carlo tuning. It is also important to understand the b production because a lot of important new physics signal analyses suffer from large b background.

In this thesis, the perspective for the J/ψ differential cross section and polarization measurements in LHCb are discussed. The thesis is divided into four parts. The first part gives a review of the production mechanism for heavy hadrons. Their comparison with the experimental results is also given in this part. In the second part, the experimental setup of the LHCb detector is presented together with the description of the software structure. The strategy for the J/ψ differential cross section and polarization measurements are shown in the third part using Monte Carlo simulation data. Some results from recent real data are given in the last part.

[1] The b-hadron cross section can be measured simultaneously with the J/ψ cross section.

Chapter 2

Review of Production Mechanism and Experimental Status

In 1974, the J/ψ particle was discovered almost at the same time by two groups led by Ting [6] and Richter [7]. This was called November Revolution because at that time, the fourth flavor (charm) was predicted by the theory [28, 29] but the experimental results on the R value [30] (Ratio of the hadronic cross section to the μ cross section in e^+e^- collisions) did not show any obvious evidence of it. The observed narrow $\mu^+\mu^-$ mass peak of J/ψ offered the direct proof of the existence of the fourth quark and two years later Ting and Richter shared the Nobel Prize for Physics.

The J/ψ has a similar structure than the positronium, it is composed of a charm quark and a anti-charm quark. Particles having the same composition as the J/ψ are called charmonium [31]. Due to its relatively simple structure, the mass spectrum and decay properties of the charmonium can be well predicted and the comparison with the experimental results improves our understanding of the underlying strong interaction properties.

The charmonium system can be considered as a non-relativistic system because the calculation shows that the square of charm quark velocity v^2 is ~ 0.3 [32] in the charmonium center-of-mass frame. A non-relativistic Schrödinger equation is used to describe a charmonium system:

$$-\frac{1}{2\mu} \bigtriangledown^2 \psi(\vec{x}) + V(r)\psi(\vec{x}) = E\psi(\vec{x}), \tag{2.1}$$

here $\mu = m_c/2 \sim 0.6$ GeV/c^2 [33] is the reduced mass (m_c is the mass of the

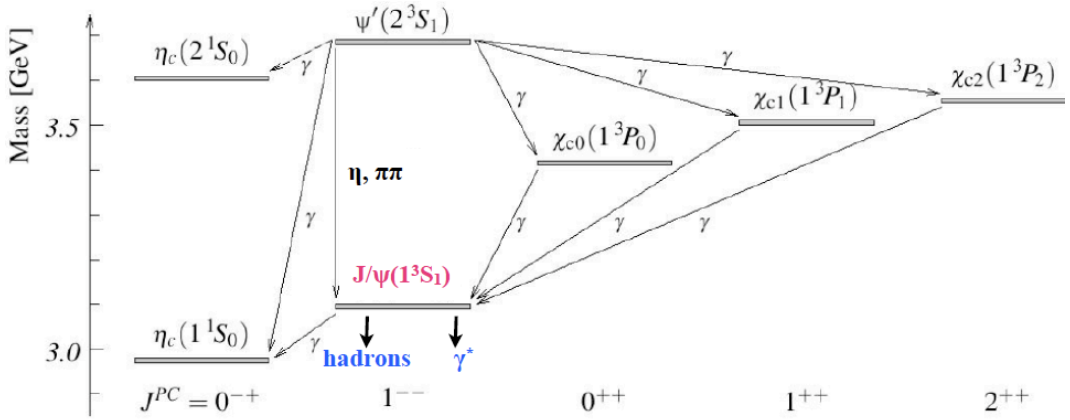

Figure 2.1: Charmonium states and their decays.

constituent charm quark), $r = |\vec{x}|$ is the distance between the c and $\bar{c}$ quarks, $\psi(\vec{x})$ is the $c\bar{c}$ wave function in the center-of-mass frame of the charmonium, and E is the characteristic energy. An usually used potential function $V(r)$ is:

$$V(r) = -\frac{4}{3}\frac{\alpha_s(\mu)}{r} + Kr, \tag{2.2}$$

where K is about 1 GeV/fm and sets the confinement scale. The mass of the system can be calculated as

$$M_{c\bar{c}} = 2m_c + E(m_c, V). \tag{2.3}$$

With further corrections such as relativistic effects or spin effects, the mass of the experimentally observed states shown in Figure 2.1 can be reproduced by the theory.

The total angular momentum (J), parity (P), charge conjugation (C) are commutative with the Hamilton operator and the particles can be categorized with their J^{PC} values as shown in Figure 2.1. Here P and C have the following relationships with the orbital angular momentum (L) and spin (S):

$$P = (-1)^{L+1} \qquad C = (-1)^{L+S}. \tag{2.4}$$

The ground state of the charmonium system is $\eta_c(1S)$ which is in a spin singlet state with its quantum number J^{PC} equal to 0^{-+}. The J/ψ is in a spin triplet state and its quantum number J^{PC} is 1^{--}. At e^+e^- colliders, the charmonium states like J/ψ or $\psi(2S)$ can be produced directly through a

virtual photon as they have the same quantum number as the photon. Other charmonium states are either directly produced at hadronic colliders or from decays of other particles.

As the mass of the J/ψ (~ 3.1 GeV/c^2) falls below the open-charm threshold (~ 3.8 GeV/c^2), the conservation of J, P, C forces it to annihilate mainly through off-shell photon or through gluons. Since the J/ψ is colorless, the leading QCD Feymann diagrams are through three gluons ($1/\alpha_s^3$) or two gluons with an additional radiative photon (lower rate, but important for the J/ψ study) and this makes the hadron decay rate at the same level as the electromagnetic decay rate, thus the J/ψ can be easily identified as a narrow resonance. The relatively high electromagnetic decay rate ($\sim 25.4\%$ [33]) also gives J/ψ a high di-leptonic decay branching ratio ($\sim 11.9\%$ [33]) and decay channels like $J/\psi \to \mu^+\mu^-$, $J/\psi \to e^+e^-$ are the golden channels for the J/ψ production study. This is especially important at hadronic colliders to achieve a high S/B (signal to background) ratio. In this thesis, the decay channel $J/\psi \to \mu^+\mu^-$ is used for the cross section and polarization measurements.

2.1 J/ψ Production at Hadron Colliders

At high-energy hadron collider experiments, the J/ψ is produced mainly through the following processes:

1. Direct production through the interactions of partons or decay product of charmonium excited states produced directly: J/ψ produced in this way originate from the primary vertex and are named "prompt J/ψ" in this thesis. The experimental results from CDF [1] show that J/ψ from the decays of charmonium states contribute 30% of the prompt J/ψ production in proton-antiproton collisions at $\sqrt{s} = 1.96$ TeV [14]. Table 2.1 lists some branching ratios for the charmonium excited states decaying into J/ψ.

2. Decay product of b hadrons: Table 2.2 lists the branching ratios for b hadrons to J/ψ. The branching ratio for the mixture of b hadrons (H_b)

[1] CDF (the Collider Detector at Fermilab) is one of the detectors at Fermilab proton-antiproton collider (Tevatron) [34, 35].

Table 2.1: Branching ratios of charmonium excited states decaying into J/ψ.

Process	Branching Ratio
$\chi_{c0} \to J/\psi\gamma$	$(1.30 \pm 0.11)\%$
$\chi_{c1} \to J/\psi\gamma$	$(35.6 \pm 1.9)\%$
$\chi_{c2} \to J/\psi\gamma$	$(20.2 \pm 1.0)\%$
$\chi_{c2} \to J/\psi\pi^+\pi^-\pi^0$	$< 1.5\%$
$\psi(2S) \to J/\psi X$	$(56.1 \pm 0.9)\%$

Table 2.2: Branching ratios of b hadrons to J/ψ.

Process	Branching Ratio
$B^{\pm}/B^0 \to J/\psi X$	$(1.094 \pm 0.032)\%$
$B_s \to J/\psi\phi$	$(0.13 \pm 0.04)\%$
H_b(mixture of b-hadrons) $\to J/\psi X$	$(1.16 \pm 0.10)\%$

to J/ψ is obtained from a combination of LEP, Tevatron and $Sp\bar{p}S$ results [2] [33]. As b hadrons decay through weak processes, they have a relatively longer lifetime and can be distinguished from prompt J/ψ using their distance of flight with respect to the primary vertex.

3. J/ψ from bottomonium, top quark, electro-weak processes, *etc*: only few J/ψ are produced from these processes and they are ignored in this analysis.

As said above, using the difference in the distance between the decay vertex and the primary vertex, the contributions of prompt J/ψ and J/ψ from b to the total J/ψ production can be distinguished and so do polarization properties of the two components. Polarization properties of the two components can then be measured after the distinction. These results can be used to test QCD predictions. For the prompt part, the contributions from charmonium excited state decays should be considered before comparing experimental measurements with the predictions. The H_b production at LHCb can also be deduced from the branching ratio listed in Table 2.2 using J/ψ

[2] If a branching ratio is measured by several experiments, the one with highest center-of-mass energy is used.

from b-hadron decays.

2.2 Direct J/ψ Production Mechanism

QCD calculations for the direct J/ψ production at high energy hadron colliders are based on the factorization assumption [36, 37, 38, 39]. It assumes that the production process can be factorized, i.e. understood in two distinct steps: the production of $c\bar{c}$ and the $c\bar{c}$ hadronization into a charmonium. The first step is calculated perturbatively in an expansion in powers of α_s. The second step includes the "long distance" effects and the matrix elements are assumed to be universal.

2.2.1 Parton Distribution Function

Due to the asymptotic freedom property of QCD, quarks and gluons in the high-energy protons can be regarded as point-like constituents without interactions and are usually referred to as partons. The momentum distribution of the partons can be described by the parton distribution function (PDF). Noting the proton momentum as $\vec{P}$, the parton momentum parallel to the proton momentum $\vec{p}_{\parallel}$ can be written as

$$\vec{p}_{\parallel} = x\vec{P} \tag{2.5}$$

where x is the fraction of the proton momentum taken by the parton. Eq. (2.5) gives the description for the momentum along the direction of the proton, if the parton transverse momentum is noted $\vec{k}_T$, the parton energy is

$$E = \sqrt{(x\vec{P})^2 + k_T^2}. \tag{2.6}$$

Here partons are assumed to be massless. The main process for the $c\bar{c}$ production at hadron colliders is through interactions of two partons from different protons and the square of the center-of-mass energy of the two partons is

$$s = (p_1 + p_2)^2 \approx x_1 x_2 S, \tag{2.7}$$

where S is the square of the center-of-mass energy of the two colliding protons:

$$S = (P_1 + P_2)^2. \tag{2.8}$$

The PDF is defined as the probability ($f(x, \vec{k}_T)$) to find a parton with a momentum fraction x and a transverse momentum $\vec{k}_T$ in the proton. $\vec{k}_T$ represents effects from soft gluons. For some special processes, it should be taken into account. For other processes, the PDF $f(x, \vec{k}_T)$ is usually integrated over $\vec{k}_T$ and the obtained PDF $f(x)$ is assumed to describe the physical phenomena of interest very well.

According to its definition, the PDF should satisfy the sum rule

$$\int_0^1 dx \sum_i x f_i(x) = 1, \tag{2.9}$$

where i represents different partons in the hadron. As the valence quarks for the proton are uud, other sum rules like:

$$\int_0^1 dx (f_u(x) - f_{\bar{u}}(x)) = 2; \tag{2.10}$$

$$\int_0^1 dx (f_d(x) - f_{\bar{d}}(x)) = 1; \tag{2.11}$$

$$\int_0^1 dx (f_q(x) - f_{\bar{q}}(x)) = 0 \qquad q = c, s, b, t \tag{2.12}$$

should also be satisfied.

As a common property of QCD calculations, the determination of a PDF depends on the factorization scale μ_F (see below for the description of factorization). The separation of the collinear emissions of soft gluons is parameterized by this scale. The evolution of the PDF as a function of μ_F is described by the Dokshitzer-Gribov-Lipatov-Altarelli-Parisi (DGLAP) function [40, 41, 42]. After transforming the PDF obtained from experiments like deep inelastic scattering at low energy to the energy considered for the cross section computation, it can be used to predict the process we are interested in. Besides the dependence on μ_F, we also need to define a certain renormalization scheme to fix the PDF (usually $\overline{\text{MS}}$) and all the calculations should be done within the same scheme.

After obtaining the momentum distribution functions of the partons, the production cross section can be written as

$$\sigma(P_1, P_2) = \sum_{i,j} \int dx_1 dx_2 f_{1,i}(x_1, \mu_F^2) f_{2,j}(x_2, \mu_F^2) \sigma_{i,j}(p_1, p_2, \mu_F^2, \mu_R^2). \tag{2.13}$$

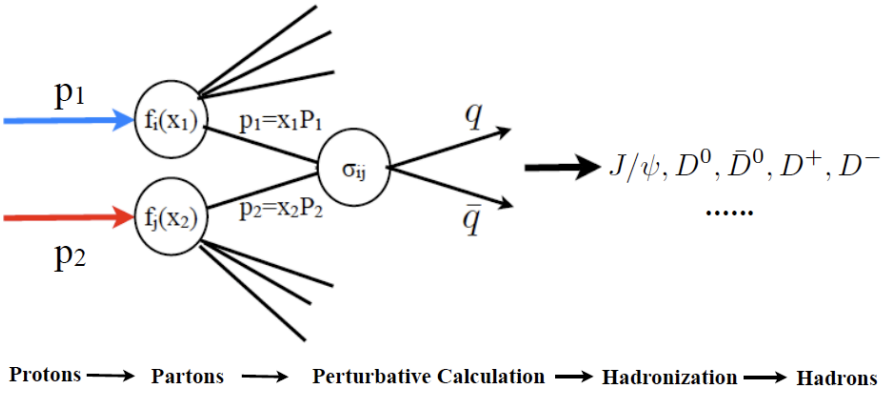

Figure 2.2: Schematic graph for the production of heavy quarks.

Here, i, j indicate different partons which produce the $c\bar{c}$ or $b\bar{b}$ pair. $f(x, \mu_F^2)$ is the parton density function at the energy scale μ_F. $\sigma_{i,j}(p_1, p_2, \mu_F^2, \mu_R^2)$ is the cross section for producing a $c\bar{c}$ or $b\bar{b}$ pair at the energy scale μ_F and renormalization scale μ_R [3]. In order to produce a $c\bar{c}$ or $b\bar{b}$ pair, the invariant mass of the two partons should be more than twice the produced quark mass:

$$\sqrt{s} > 3.5 \text{ GeV}/c^2 \text{ (charm)} \ , 8.5 \text{ GeV}/c^2 \text{ (bottom)} \tag{2.14}$$

This also ensures there is no divergence at leading order calculation for the s-channel. After the production of the $c\bar{c}$ or $b\bar{b}$ pair, c ($\bar{c}$) quarks or b ($\bar{b}$) quarks can either form quarkoniums or combine with other quarks to form hadrons like D^+, B^+. The schematic graph for the production is shown in Figure 2.2.

2.2.2 Perturbative Calculations and Hadronization

The main part for understanding the mechanism of charmonium production is the perturbative production of $c\bar{c}$ and its hadronization. As more and more experimental data are collected, theories improve a lot in describing the J/ψ production properties but still more information are needed for a better and complete understanding. Several models or effective theories together with their limitations are given in the following sections.

[3] μ_F is usually chosen to be equal to μ_R for simplicity.

Color Evaporation Model

The Color Evaporation Model (CEM) [43, 44, 45, 46] was proposed in 1977, three years after the J/ψ was discovered and was revived later [47, 48]. It is based on the following assumptions:

1. There is no connection between the produced $c\bar{c}$ pair and the final charmonium state, that is $c\bar{c}$ can hadronize into any charmonium state. Thus in the CEM, the produced $c\bar{c}$ can either be a color-singlet or a color-octet state, the color-octet state can neutralise its color by interacting with collision-induced color fields.

2. The produced $c\bar{c}$ hadronizes into different charmonium states with fixed fractions which do not depend on the production energy or process.

The production cross section for J/ψ can be written as:

$$d\sigma(J/\psi) = f_{J/\psi} \int_{2M_c}^{2M_D} dM_{c\bar{c}} \frac{d\sigma(c\bar{c})}{dM_{c\bar{c}}} \tag{2.15}$$

here $f_{J/\psi}$ is the hadronization fraction of $c\bar{c}$ into J/ψ and it is an universal parameter which can be determined experimentally.

The above simple model gives qualitative results on the J/ψ production, but it fails when more detailed, quantitative results are needed. In fact, even in the same experiment, the fraction between different charmonium states can vary as a function of p_T and the CEM cannot explain it correctly.

Color Singlet Mechanism

The Color Singlet Mechanism (CSM) [49, 50, 51, 52, 53, 54, 55, 56, 57] is the direct application of QCD to explain the J/ψ production, based on the following assumptions:

1. The $c\bar{c}$ pair should have the same quantum number as the produced charmonium state, so only $c\bar{c}$ paris in color-singlet states contribute to the charmonium production.

2. In the center-of-mass frame, the charmonium is produced with $c\bar{c}$ nearly at rest. The wave function and its derivatives are evaluated with zero separation ($r = 0$). This is called the "static assumption".

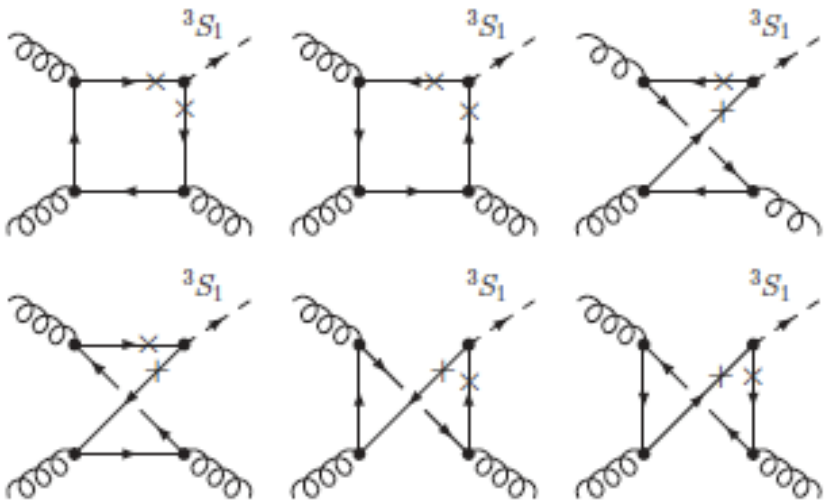

Figure 2.3: Leading-order Feymann diagrams for the CSM production.

In the CSM, all the contributions from low energy effects are absorbed into the wave function of the charmonium state and the hard parts are calculated by perturbative QCD. The wave function and its derivatives at origin are determined by comparing theoretical expressions for quarkonium decay rates in the CSM with experimental measurements. The only input needed for the CSM is the PDF. The cross section for all the charmonium states can be written as

$$\sigma(^{2S+1}L_J) = \sigma(c\bar{c}(^{2S+1}L_J))\left|\frac{d^L}{dr^L}R_{nL}(0)\right|^2 \tag{2.16}$$

where R_{nL} is the radial wave function. $\sigma(c\bar{c}(^{2S+1}L_J))$ is the cross section of the $c\bar{c}$ pair which can be calculated perturbatively. The main contribution to J/ψ production at leading order is $gg \to J/\psi g$. It was pointed out by Chang [52] that it may dominate the J/ψ production at high p_T. The leading order Feymann diagrams for the production are shown in Figure 2.3. The cross sections for $^3S_1$ states were then calculated and were compared with CERN ISR data [56] at $\sqrt{s} = 27$ GeV and later for other experiments.

In 1984, Halzen [58] and others [59] pointed out that in high energy collisions, J/ψ from b hadrons can contribute significantly to the total cross section. This idea was used later to explain the UA1 [60] measurements, however the p_T slope was not compatible with the prediction.

But in 1993, the new Tevatron data for the $\psi(2S)$ production showed clearly disagreement with the predictions [61]. Though the difference for

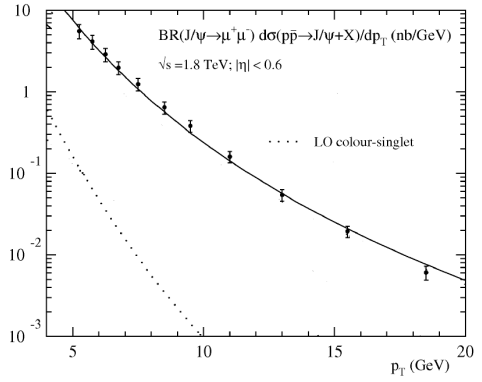

Figure 2.4: Comparison between the CDF cross sections [10] and the leading-order CSM prediction [62] as a function of p_T.

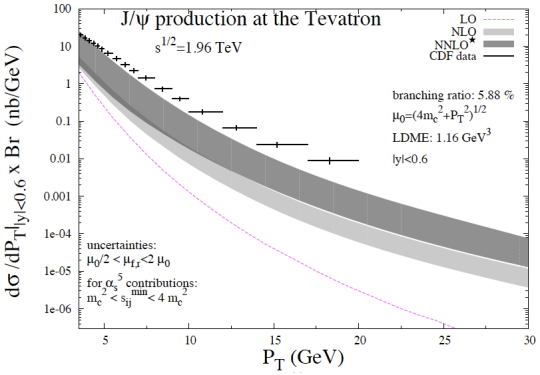

Figure 2.5: Comparison between CDF results [10] and the CSM prediction with higher order corrections [16, 63, 64, 65, 57, 66].

J/ψ was not as large as $\psi(2S)$, it was thought that this was due to the contributions from χ_c decays. After correctly considering the contributions from excited states, the predicted J/ψ should also be much smaller than the measured results. This was proven later by CDF results [14].

Figure 2.4 shows the comparison between CDF results for the direct J/ψ production and leading-order CSM prediction [52, 53, 54, 55, 56]. As can be seen in the figure, the prediction was really one orders of magnitude smaller than the measurements, and did not explain correctly the p_T shape either. The theory gives a dependence of $\alpha_s^3 \frac{(2m_c)^4}{p_T^8}$ (α_s is the strong coupling constant) while experimental results show a harder spectrum.

In order to explain the difference between the theory and the experimental results, Cacciari, Braaten *et al.* [16, 63] calculated the fragmentation contribution (Next-to-Leading Order, NLO). The result shows that in the high transverse momentum region, its dependence on the transverse momentum is $\alpha_s^4 \frac{(2m_c)^4}{p_T^4}$. This NLO result together with the Leading-Order (LO) calculation agrees with the experimental p_T shape but not with the global scale. It also gives the hint that when there are other scale dependences (like p_T), perturbative truncation according to the strong coupling constant may not work, as higher order Feymann diagrams can contribute dominantly in the high transverse momentum region. After the NLO calculation, further corrections like NNLO* (part of Next-to-Next-Leading Order) [64, 65, 57, 66] are also calculated; the results are shown in Figure 2.5. The dashed line is

the LO result and the solid lines represent different higher-order corrections. The theory predictions now get closer to the experimental results but there is still a small gap between the two while the NNLO* calculations for $\Upsilon(1S)$ agree with the measured distribution very well [65, 66].

Besides the study of higher-order corrections, theorists also revisited the different assumptions for the CSM like the "static assumption" and the color-singlet assumption. Bodwin *et al.* [67] showed that even at LO, the P-wave color-singlet term has no-elimination infrared divergence. This means that the CSM is not a self-consistent theory. Non-Relativistic Quantum Chromo Dynamics [68, 69] (NRQCD) encompasses the CSM, but goes beyond it.

NRQCD

NRQCD is a self-consistent Effective Field Theory (EFT), meaning that divergences at any order can be cancelled or absorbed into other parts. It is based on the assumption that the charmonium system can be treated in a non-relativistic way. The relativistic contributions are subtracted with the introduction of a ultraviolet cut-off which turns the full QCD into NRQCD. The relativistic effects are considered to be local and compensated by adding new local interactions to the Lagrangian. This represents a non-relativistic Schrödinger field theory for the heavy quark and anti-quark couplings to the relativistic fields of light quarks and gluons. In this case, the heavy particle and its antiparticle are de-coupled and can be described by a non-relativistic Pauli equation.

The effective Lagrangian of the NRQCD is written as

$$\mathcal{L}_{NRQCD} = \mathcal{L}_{light} + \mathcal{L}_{heavy} + \delta\mathcal{L}, \tag{2.17}$$

where $\mathcal{L}_{light}$ represents the Lagrangian of the light quarks and soft gluons, $\mathcal{L}_{heavy}$ describes the properties of the heavy quarks, and $\delta\mathcal{L}$ is the interaction term, which can be obtained by comparing with the full QCD. In order to be consistent with the full QCD theory, infinite terms should be added but this is impossible to handle. NRQCD uses Long Distance Matrix Elements (LDME) which can be obtained from experiments to describe the processes for a $c\bar{c}$ pair to form charmonium states. Due to the non-relativistic nature of the charmonium system, there is another variable – the velocity of the c ($\bar{c}$) quark in the center-of-mass frame, $v \sim \alpha_s(m_c v)$ which can be used

in the expansion of the effective theory: we can order the different LDME terms with the power of v and truncate them to the precision needed. The small inter-quark velocity v also sets different scales in the production of quarkonium together with the quark mass m_c.

1. $m_c v^0$: The mass of the charm quark represents the length scale to create a charm pair. It is also used to set the ultra-violet cut-off of the Lagranian which separates the non-pertubative, relativistic effects.

2. $m_c v^1 \sim \Lambda_{QCD}$: The momentum of the heavy quark in the center-of-mass frame of the bound state. It sets the scale of the radius of the produced charmonium. The formation of the quarkonium from the $c\bar{c}$ pair takes place at this scale.

3. $m_c v^2$: The typical kinetic energy of the heavy quark which sets the time scale for the heavy quark to form a quarkonium state.

4. p_T: In a hard scattering process, another scale enters the calculation, it is the momentum transfer in the production process. In the J/ψ production at hadron colliders, it is usually taken to be of the order of the transverse momentum p_T of the produced J/ψ. It is conjectured that NRQCD factorization is valid if this scale is of the order of m_c or larger.

The cross section prediction of NRQCD can be written as:

$$\sigma(H) = \sum_n \sigma(c\bar{c}, n) < \mathcal{O}_n^H > \tag{2.18}$$

here $\sigma(c\bar{c}, n)$ is the cross section for producing a $c\bar{c}$ pair with quantum numbers n (color). $< \mathcal{O}_n^H >$ is the LDME for a $c\bar{c}$ pair with quantum number n to form a charmonium state H. Here, as in the CSM, the high-momentum, perturbative terms go into $\sigma(c\bar{c}, n)$. The low-momentum non-perturbative parts go into the matrix elements $< \mathcal{O}_n^H >$. The CSM is just a special case of the theory when neglecting other contributions from different color, spin and orbital angular momentum states. Color-octet terms also contribute to the production in NRQCD, the leading order term is α_s^2 and more Feymann diagrams contribute to the production. The Feymann diagrams of the $c\bar{c}$ and $b\bar{b}$ are similar, we discuss them together with the b quark production mechanisms later.

In the NRQCD, the generation of a quarkonium state not only includes the Fock state $|Q\bar{Q}>$ but also includes the Fock states $|Q\bar{Q}g>$ and $|Q\bar{Q}gg>$. For some processes, $|Q\bar{Q}g>$ may significantly contribute to the production cross section. For example, in the generation of high p_T J/ψ at hadron colliders, the contributions from color-octet parts like $< \mathcal{O}_8^{J/\psi}(^3P_0) >$, $< \mathcal{O}_8^{J/\psi}(^3P_1) >$, $< \mathcal{O}_8^H(^3P_2) >$ could dominate the production, while in the e^+e^- annihilation to J/ψ, the $^3S_0$ color-singlet state contributes more to the total cross section.

For the Fock-state $|Q\bar{Q}g>$, the probability of going into the Fock-state $|Q\bar{Q}>$ is of the order v^2, i.e. an extra gluon introduces an extra v^2 dependence. Since the two states differ only by a dynamic gluon, the transition can only happen when the difference of orbital angular momentum ΔL is ± 1 or if it is the spin-flip transition $\Delta S = \pm 1$. For example, for the J/ψ production, the leading color-singlet LDME is $< O_1^H(^3S_1) >$, which is at the level of v^3. The color-octet matrix element $< O_8^H(^1S_0) >$ gives an order of v^5 while the emission of a gluon to flip the spin gives another contribution of order v^2. In all, it is at the level of v^7. After obtaining the v dependence, we can truncate high order terms according to the required precision. The obtained results is then compared with the experimental results and fitted to obtain the LDME numbers. These LDME values are then used for further predictions. Simplified relations between the matrix elements are used to roughly estimate the ratio of the cross sections. For example,

$$\begin{aligned}
&< \mathcal{O}_1^{J/\psi}(^3S_1) >= 3 < \mathcal{O}_1^{\eta_c}(^1S_0) > \\
&< \mathcal{O}_1^{\chi_{cJ}}(^3P_J) >= \frac{1}{3}(2J+1) < \mathcal{O}_1^{h_c}(^1P_1) > \\
&< \mathcal{O}_8^{\chi_{cJ}}(^3S_1) >= \frac{1}{3}(2J+1) < \mathcal{O}_8^{h_c}(^1S_0) >
\end{aligned} \tag{2.19}$$

From Eq. (2.19), we can obtain that the first order approximation for the ratio of J/ψ production to η_c production is 3.

Figure 2.6 compares the NRQCD prediction [19, 70, 71] with the CDF results [10]. The prediction agrees with the data both in shape and total cross section. But one should note that the values of the matrix elements used for this COM prediction come from the fit of CDF results. The agreement does not mean it is correct and further tests on COM are needed.

Though NRQCD predictions were successful for some processes like $\gamma\gamma \to J/\psi X$ [72], color-octet contributions are less required by other experimental

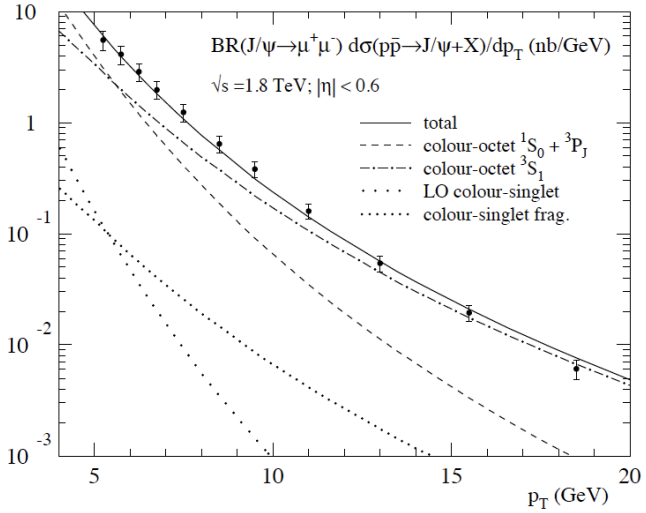

Figure 2.6: Comparison between the COM prediction [19, 70, 71] and CDF data. [10]

data [73, 74]. Even more seriously, they do not predict correctly the polarization [27]. In practice, sometimes the series in α_s and v converge slowly and the non-perturbative matrix elements are usually poorly determined. As a result the errors for the cross section estimates are large, sometimes 100% or even more. The ratio between two cross sections may be a good observable because some errors can cancel out. The fraction of J/ψ coming from higher charmonium states, the ratio between χ_{c1} and χ_{c2} or the J/ψ polarization are several examples [4].

2.2.3 Polarization

Besides the cross section measurements, the J/ψ initial polarization also contains information about the heavy quark production mechanism and it is usually studied through the angular distribution of the J/ψ decay products. The general form for the angular distribution of the J/ψ decaying to two

[4]Polarization parameters can indeed be written in the form of the ratio of two different cross sections.

muons is [75]:

$$P(\cos\theta,\phi) = \frac{1}{N}\frac{\mathrm{d}N}{\mathrm{d}(\cos\theta)\mathrm{d}\phi} \propto 1 + \alpha_1\cos^2\theta + \alpha_2\sin 2\theta\cos\phi + \alpha_3\sin^2\theta\cos 2\phi \tag{2.20}$$

where θ is the angle between the direction of μ^+ in the centre-of-mass frame and a dedicated axis or polarization axis (z' axis [5]). The plane formed by the two proton beams and the J/ψ momentum is called the "production plane". The y' axis is chosen to be perpendicular to the production plane as:

$$\hat{y}' = \frac{\hat{z}\times\vec{p}_{J/\psi}}{|\hat{z}\times\vec{p}_{J/\psi}|} \tag{2.21}$$

here $\hat{z}$ is the unit axis of the LHCb coordinate system, $\vec{p}_{J/\psi}$ is the J/ψ momentum. The x' axis is defined so that (x', y', z') is a right-handed coordinate system. ϕ is the corresponding azimuthal angle with respect to x' axis. The mixture of differently polarized states can be fully described by the spin density matrix:

$$(\rho) = \begin{pmatrix} \rho_{-1,-1} & \rho_{-1,0} & \rho_{-1,+1} \\ \rho_{0,-1} & \rho_{0,0} & \rho_{0,+1} \\ \rho_{+1,-1} & \rho_{+1,0} & \rho_{+1,+1} \end{pmatrix}$$

The information on the spin density matrix can be retrieved from the measurement of the angular distribution in Eq.(2.20). The relationships between the three parameters in Eq. (2.20) and the spin density matrix elements are:

$$\alpha_1 = \frac{\rho_{+1,+1}-\rho_{0,0}}{\rho_{+1,+1}+\rho_{0,0}}, \qquad \alpha_2 = \frac{\sqrt{2}\mathrm{Re}\rho_{+1,0}}{\rho_{+1,+1}+\rho_{0,0}}, \qquad \alpha_3 = \frac{2\rho_{+1,-1}}{\rho_{+1,+1}+\rho_{0,0}} \tag{2.22}$$

The last two terms in Eq.(2.20) exist because of the non-zero J/ψ transverse momentum p_T. If $p_T^{J/\psi}$ is 0, the angular distribution becomes

$$P(\cos\theta) = \frac{1}{N}\frac{\mathrm{d}N}{\mathrm{d}(\cos\theta)} \propto 1 + \alpha_1\cos^2\theta \tag{2.23}$$

where the meaning of α_1 can be easily seen by defining it using the cross section of transversely polarized J/ψ, σ_T and longitudinally polarized J/ψ, σ_L

$$\alpha_1 = \frac{\sigma_\mathrm{T}-2\sigma_\mathrm{L}}{\sigma_\mathrm{T}+2\sigma_\mathrm{L}} \tag{2.24}$$

[5]Here, we use z' axis to distinguish it from LHCb frame, referring to its definition below.

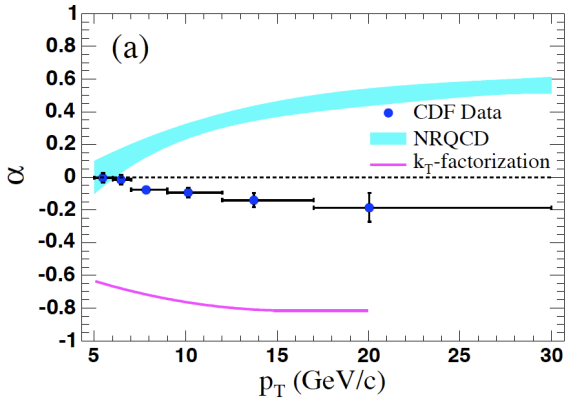

Figure 2.7: J/ψ polarization measurements at CDF [27] compared to theoretical predictions [25, 26].

There is no polarization if $\alpha_1 = 0$ since the two longitudinal and the transverse polarization states are equally produced. It is totally longitudinally polarized if $\alpha_1 = -1$ and it is totally transversely polarized if $\alpha_1 = +1$. The polarization measurement performed by CDF [27] used this simple notation. Based on this simple formula the CEM predicts that all charmonium states should be produced un-polarized since it predicts that all charmonium states are produced randomly. The CSM predicts a non-zero transverse polarization [24]. NRQCD gives similar results but with a more restrictive region: $0.31 < \alpha_1 < 0.63$ [25]. But after considering small-x effects with k_T factorization theory, NRQCD gives an opposite prediction [26]. Neither of the predictions agree with the latest CDF results [27] as shown in Figure 2.7 for J/ψ. We can see that only the k_T factorization theory shows a similar trend.

Before understanding the difference between the experimental results and theory predictions, we need first to have a clear understanding on the experimental results. Studies by Faccioli *et al.* [76] show that it is necessary to do a full angular analysis on ϕ and θ in at least two different reference frames to obtain a full understanding of the J/ψ polarization. Three definitions of the polarization axis (z' axis) are usually used in the litterature:

1. Gottfried-Jackson (GJ) frame: the direction of one of the beam momenta in the J/ψ rest frame.

2. Helicity frame (HX): the direction of the J/ψ momentum in the center-of-mass frame of the two beams. If there is no crossing angle between

the two beams and if the beams have the same energy, it is the direction of the J/ψ momentum in the laboratory frame.

3. Collins-Soper frame (CS): the bisector of the directions of the two beam momenta in the J/ψ rest frame.

The results obtained in one frame can be transformed into the other frames with the knowledge of the J/ψ spectrum. In LHCb, the polarization measurements will be done in all the three frames for different p_T and η bins. In this thesis, only the results in the helicity frame are shown. The results in the other frames can be obtained in a similar way.

2.3 b-hadron Production

The inclusive b-hadron production is another interesting topic to study heavy flavor production. In this thesis, we use J/ψ from b-hadron decays to measure the b-hadron production with the already known branching fraction to J/ψ: $\mathrm{Br}(b \to J/\psi X) = (1.16 \pm 0.10)\%$ [33].

The experimental and theoretical study of the b-hadron production cross section has already successfully led to the implementation of the color-octet mechanism and other general results in b-hadron physics. Further understanding both in experimental data and theoretical calculation can let us examine new dynamical regimes like small-x and other new phenomena, for example super-symmetry. A nice review of the saga of the b-hadron cross section measurements and theoretical predictions can be found in [13]. With the coming LHC data, new adventures will begin in a new energy region and a new pseudo-rapidity (η) region.

Four Feymann diagrams shown in Figure 2.8 contribute to the leading-order b-quark production in the perturbation theory,

$$q\bar{q} \to Q\bar{Q}, \qquad gg \to Q\bar{Q}. \tag{2.25}$$

The D_0 and D_3 processes go through a virtual gluon to produce the quark and the anti-quark; the produced states should then be in a color-octet state. The D_1 and D_2 processes can be either in a color-octet state or in a color-singlet state. There are no divergences at this level. When coming to the NLO calculations, divergences emerge in different diagrams. Divergences

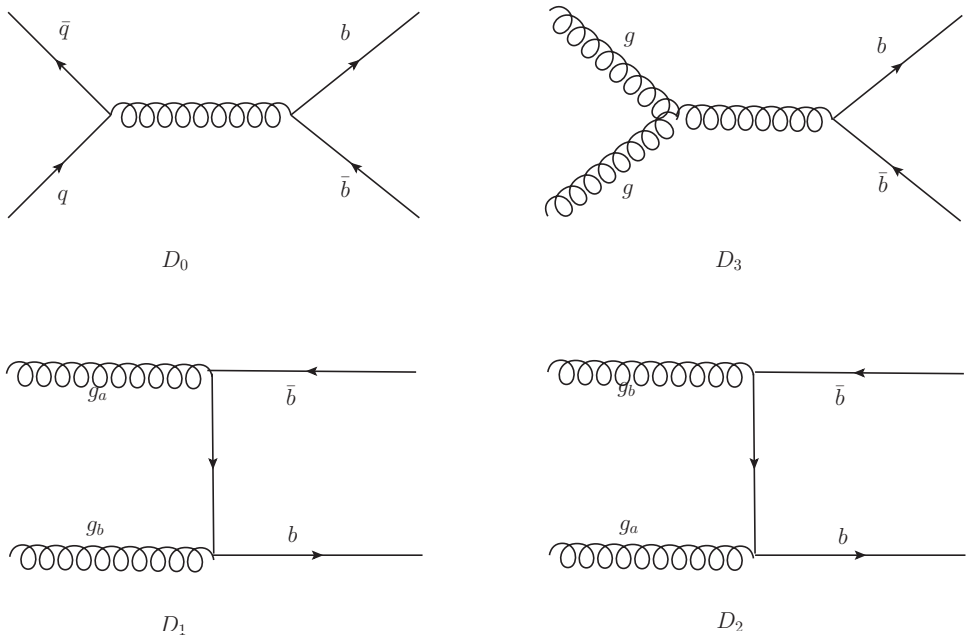

Figure 2.8: The leading-order Feymann diagrams for b production.

may come from virtual loops. The ultraviolet divergences can be absorbed by the renormalization process. The main idea of the renormalization is characterised by two steps: first, the divergences are isolated out from the calculation, and second, variables like α_s, mass or wave function are redefined so that the singularities are cancelled out. The renormalization process introduces a scale dependence (μ_R). As the renormalization process deals with the cancellation between two infinities, adding or subtracting a constant does not affect infinity, thus renormalization can be done in several different ways. The commonly used renormalization scheme is the Modified Minimal Substraction Scheme ($\overline{\text{MS}}$) [77]. In this method, we first calculate the results in dimension $4-\epsilon$. The diverging terms in $1/\epsilon$ and $\ln(4\pi-\gamma_E)$ are then subtracted. The dependence on the renormalization scale enters in the calculation through $g_s \to \mu_R^{\epsilon} g_s$ [6]. For α_s, its dependence is described by the β function

$$\mu\frac{\partial\alpha_s}{\partial\mu} = 2\beta(\alpha_s) = -\frac{11-2n_f/3}{2\pi}\alpha_s^2 - \frac{51-19n_f/3}{4\pi^2}\alpha_s^3 - .... \qquad (2.26)$$

where n_f is the number of flavors with masses up to the renormalization scale. With Eq. (2.26), α_s can be calculated at any energy scale except an

[6] g_s is the QCD coupling constant, the relationship between α_s and g_s is $\alpha_s = g_s^2/4\pi$.

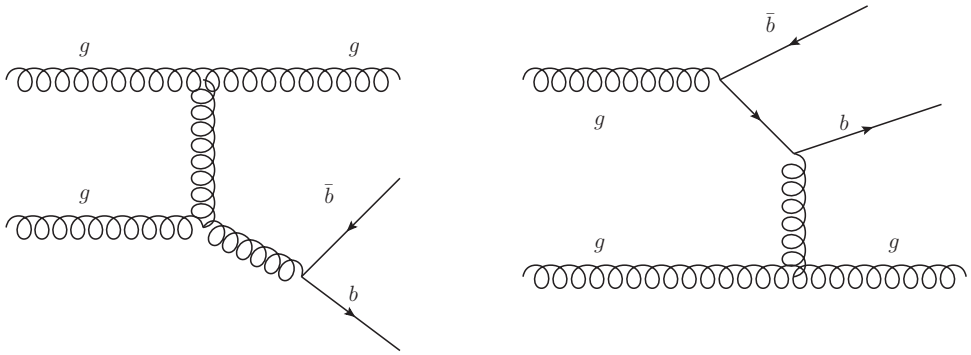

Figure 2.9: Left: NLO Feymann diagram for gluon splitting. Right: NLO Feymann diagram for flavor excitation.

integration constant which is defined by the α_s value at $\mu_0 = M_Z$, the Z mass. The current measured value for it is $\alpha_s(M_Z) = 0.1176 \pm 0.002$ [33].

Singularities may also be introduced by the collinear and soft emitted gluons. The divergences of this type can be cancelled by the infrared divergences or are absorbed into the PDF. This introduces another scale (μ_F) which appears both in the hadron cross section and in the PDF.

The study from NNLO shows that there are still strong scale dependences for the NLO calculation. Large corrections can be caused "accidentally" large coefficients like π^2 or by large logarithms due to other scales like $\log \frac{P_T^2}{m^2}$. For the first case, they do not depend on the scale. For the second case, they can be resummed. The resummation of the large logarithms capture all the essential features of the higher-order corrections and the remaining effects are small, thus we do not need to include NNLO in the computation.

Besides the new divergences, there are new diagrams introduced at NLO as shown in 2.9. They are called gluon splitting process and flavor excitation process. The contribution of these diagrams can be estimated using a fragmentation language, first the process is $gg \to gg(qg \to qg)$, then the final-state off-shell gluon evolutes into a $b\bar{b}$ pair. For the gluon splitting process, higher order corrections can be included in the $g \to b\bar{b}$ fragmentation function which can be calculated from first principles with the perturbative theory [78]. The estimated cross section for this process is proportional to $\log(p_T^2/m^2)$. This is one potentially large logarithm and it can be resummed by solving exactly the evolution equation for the fragmentation function. The flavor-excitation diagram can be treated in the same way.

Table 2.3: Fragmentation fractions for b-hadrons

b-Hadrons	Fragmentation fraction
$B^0/\bar{B}^0$	40.5 %
B^+/B^-	40.5 %
$B_s^0/\bar{B}_s^0$	10 %
$\Lambda_b^0/\bar{\Lambda}_b^0$	9 %

After the perturbative hard process, the produced heavy quarks hadronize into hadrons. This process is described by the non-perturbative fragmentation function:

$$\frac{d\sigma}{dP_T} = \int_{\frac{P_T}{E_{\text{beam}}}}^{1} \frac{dz}{z} D_Q^H(z, \mu_{\text{frag}}^2) \frac{d\sigma}{dp_t}(\mu_{\text{frag}}^2) \qquad (p_t = P_T/z) \tag{2.27}$$

Here, P_T is the hadron transverse momentum, p_t is the parton transverse momentum, $\frac{d\sigma}{dp_t}$ is the perturbative part of fragmentation function. z is the ratio between the produced hadron momentum and the heavy quark momentum. $D_Q^H(z)$ is a universal function for a given heavy quark Q hadronizing into a hadron H. This function contains the non-perturbative part of the fragmentation process. During the calculation, this function is usually parametrized. For example, the Peterson fragmentation function [79] can be used:

$$D_Q^H(z) = \frac{N_H}{z} \left(1 - \frac{1}{z} - \frac{\epsilon_Q}{1-z}\right)^{-2} \tag{2.28}$$

ϵ_Q is a variable depending on the quark flavor Q and N_H is a normalization factor to ensure the conservation of the heavy quark number:

$$\sum_H \int dz D_Q^H(z) = 1. \tag{2.29}$$

Other parameterization methods like the Kartvelishvili formula [80] are also used for the fragmentation phenomenology description. The parameters inside can be determined from the relations calculated from first principles and extracted from data (like data from e^+e^- collisions).

Table 2.3 lists the current measured fragmentation fraction for b-hadrons [33]. The results are measured at LEP energy. In the LHCb Monte Carlo, we assume the same fragmentation fractions but this should be tested when used for the prediction at LHC energy.

2.3.1 Fixed order calculations with next leading logarithm

The approach described above works very well when the heavy quark mass is the relevant scale. It fails for large transverse momentum p_T since we have another scale dependence. No matter what renormalization scale is chosen, mass or p_T, the large logarithm terms of p_T/m may spoil the convergence. The LO estimate is in terms of $\alpha_s^2(\alpha_s \log(p_T/m))^k$ which are called Leading Logarithm (LL) while the NLO terms $\alpha_s^3(\alpha_s \log(p_T/m))^k$ are called Next-to-Leading Logarithm (NLL).

During the calculation, the renormalization scale is chosen to be p_T instead of the heavy quark mass. The heavy flavor is set as an active, light degree of freedom and n_f is changed to $n_f - 1$ (it should be transformed back to n_f for the final results). The differential cross section of b-hadron can be written as:

$$\begin{aligned}\frac{d\sigma}{dp_T^2} =& A(m)\alpha_s^2 + B(m)\alpha_s^3 \\ &+ \left(\alpha_s^2 \sum_{i=2}^{\infty} a_i(\alpha_s \log(\mu_R/m))^i + \alpha_s^3 \sum_{i=1}^{\infty} b_i(\alpha_s \log(\mu_R/m))^i\right) G(m, p_T) \\ &+ \mathcal{O}\left(\alpha_s^4(\alpha_s \log(\mu_R/m))^i\right) + \mathcal{O}(\alpha_s^4 \times \mathrm{PST})\end{aligned}$$

here, $G(m, p_T)$ is quite arbitrary except that $G(m, p_T) \to 1$ when $m/p_T \to 0$. It describes the structure of power-suppressed terms in the NLL resummed calculations. PST stands for terms suppressed in the large p_T limit. The first two terms can be obtained with the already existing computation (fixed-order approach, FO) with NRQCD. The second line can also be calculated with the already available codes to evaluate the resummed cross section (resummation approach, RS) at massless limits. In order to avoid the double counting problems in the RS and FO, the contribution of FO should be subtracted in RS. The massless limit of FO is FOM0. Then, the final results are given by:

$$\mathrm{FONLL} = \mathrm{FO} + (\mathrm{RS} - \mathrm{FOM0}) \times G(m, p_T) \tag{2.30}$$

The notation of FONLL stands for the fixed-order results with Next-to-Leading logs. The detailed treatment of FONLL calculations can be found in [81]. The results of the FONLL on the calculation of b-hadron production together with the CDF measurement are shown in Figure 2.10. The two agree very well.

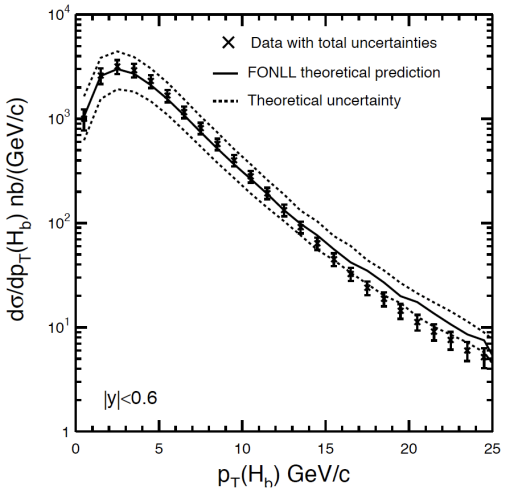

Figure 2.10: The comparison between FONLL and the measured data on the b-hadron production [10]

Table 2.4: LDME settings in the LHCb Monte Carlo.

LDME	Values
$< \mathcal{O}^{J/\psi}[^3S_1^{(1)}] >$	1.16
$< \mathcal{O}^{J/\psi}[^3S_1^{(8)}] >$	0.0119
$< \mathcal{O}^{J/\psi}[^1S_0^{(8)}] >$	0.01
$< \frac{\mathcal{O}^{J/\psi}[^3P_0^{(8)}]}{m_c^2} >$	0.01

2.4 Simulation at LHCb

After explaining the production mechanisms, we give a brief introduction of the J/ψ production simulation in LHCb. The current PYTHIA version adopted by LHCb is 6.418. This PYTHIA version contains both COM and CSM production mechanisms. Table 2.4 lists the LDME parameters used in the simulation and these parameters are obtained by fitting the CDF results [82, 83].

For both CSM and COM mechanisms, when $p_T \to 0$, it is very hard to perform the calculation. In order to avoid the above problem, a weight func-

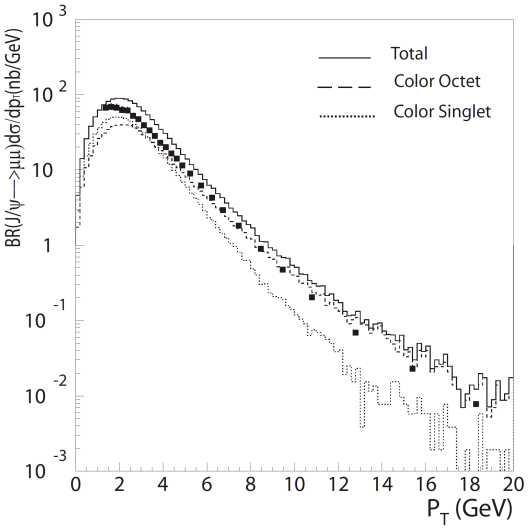

Figure 2.11: Simulation results when $p_{T_0} = 2.85$ GeV/c (Lines) and its comparison with the CDF measurement (Filled Box).

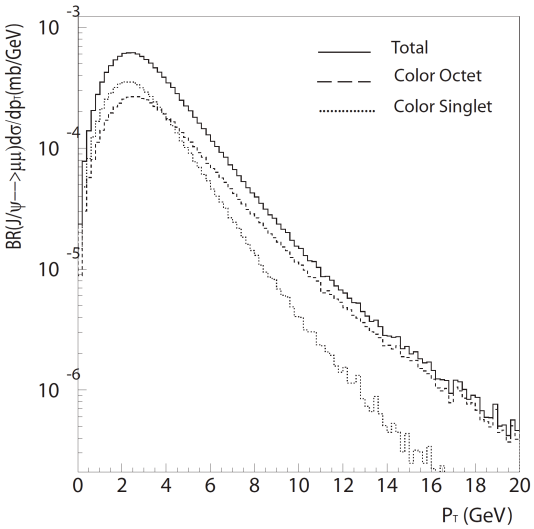

Figure 2.12: Simulation results for the differential cross section in LHCb ($1.8 < \eta < 4.9$) with parameters listed in the text.

tion is used to smooth the differential cross section [84] during the simulation:

$$W(p_T, p_{T_0}) = \frac{p_T^4}{p_T^2 + p_{T_0}^2} \tag{2.31}$$

The energy scale for the strong coupling constant becomes $p_T^2 + p_{T_0}^2$ instead of p_T^2. Figure 2.11 shows the simulation results when $p_{T_0} = 2.85$ GeV/c at $\sqrt{s} = 1.96$ TeV and its comparison with the CDF measurement , the two agree very well.

When moving to the LHC prediction ($\sqrt{s} = 14$ TeV), the energy dependence on p_{T_0} should be taken into account, it is described by the following relation:

$$p_{T_0} \to p_{T_0} \left(\frac{\sqrt{s}}{E_0} \right)^{\theta} \tag{2.32}$$

The parameter θ affects the simulated differential cross section and Figure 2.12 gives the results when $\theta = 0.1$. At $\sqrt{s} = 14$ TeV, the simulated total cross sections in 4π and in the LHCb acceptance are 158 μb and 39 μb respectively. In the above simulation, there are lots of free parameter to tune the production cross section and currently it is not yet fully studied. We still

need a lot of work to improve the heavy flavor production prediction at LHC energy.

Chapter 3

The LHCb Experiment

In this chapter, we first give an introduction to the LHC and then focus on the LHCb detector, its design philosophy and detector technologies, and explain why it is suitable for precise b physics measurements. We also give the expected physical performances together with the detector description. We introduce thereafter its trigger system which is a crucial point for operating at a hadron collider. A summary of the software implemented for the simulation, reconstruction and analysis is discussed at the end.

3.1 LHC

The LHC is located at CERN in Geneva, Switzerland. It is a proton-proton accelerator designed with a beam energy of 7 TeV which is the highest energy achieved ever. The purpose of the LHC is to test the Standard Model (SM) and furthermore, to probe signals of New Physics. Its physics programs lie on many aspects, from the search for the only undiscovered particle predicted by the Standard Model, the Higgs boson, to the quark-gluon plasma study. Theories from different areas show that New Physics should appear at the TeV scale and the LHC is the machine with which we will certainly observe something new. Designed for different physical purposes, there are four main detectors around the LHC beam line: ALICE, ATLAS, CMS and LHCb. The ALICE experiment is dedicated to the quark-gluon plasma physics with proton-proton and later Pb-Pb collisions. ATLAS and CMS are two detectors with the same physics programs, they aim at direct Higgs boson dis-

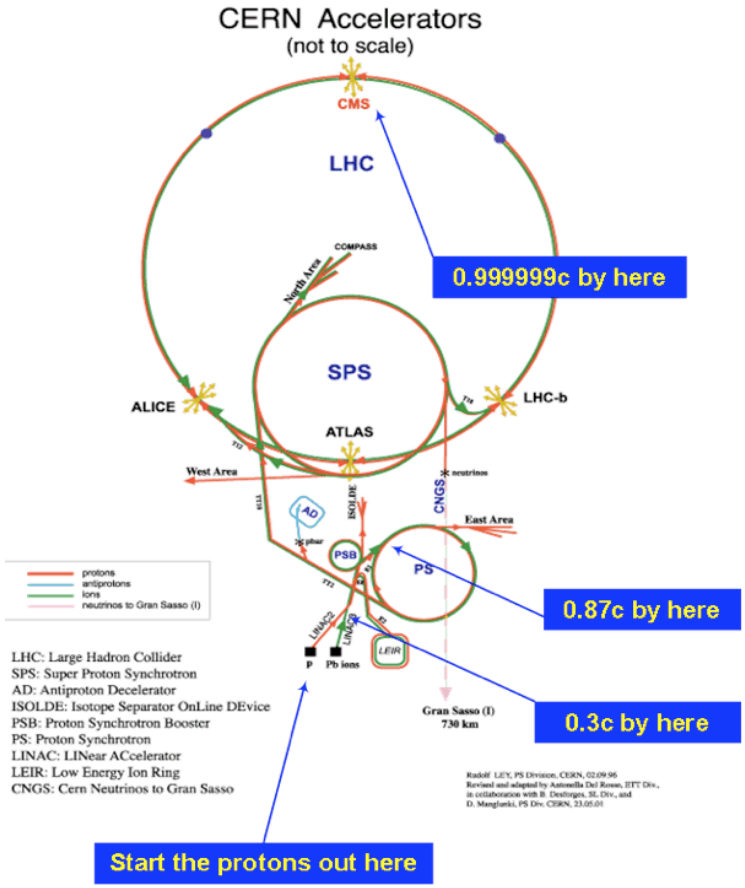

Figure 3.1: The layout of the LHC accelerator.

covery and New Physics search, like Super Symmetry particles, *etc.* LHCb is an experiment for b physics. With precise measurements in the b and c quark sectors, it can test the Standard Model through the CKM matrix and probe New Physics in loop diagrams. There are two other small experiments: TOTEM [85] and LHCf [86] for total cross section measurements and forward physics study respectively.

The layout of the LHC accelerator is shown in Figure 3.1. The generated proton beam is first pre-accelerated in a chain of accelerators and then injected in the Super Proton Synchrotron (SPS), which accelerates the proton beam further to 450 GeV energy. At the last stage, it is injected into the LHC. The LHC lies in an underground tunnel with 27 km length. It is designed to accelerate the proton beam to 7 TeV. In order to achieve such a high energy, a 8.33 T bending magnetic field is required to maintain the

protons in the accelerating tunnel. The magnetic field in the LHC is provided by superconducting magnets. The LHC accelerator uses super-fluid Helium with a temperature of 1.9 K to provide the low temperature needed for the magnets. The two proton beams circulate in the same tunnel with opposite directions. Two separate beam pipes with opposite magnetic fields are needed to bend the two beams. 1232 dipole magnets are used for this purpose and 392 quadupoles are used to focus the beams.

In each detector cavern, the two beams will cross and collide with a small angle. Each beam consists of 2808 bunches with 10^{11} protons each at design. The time between each bunch is 25 ns which means the collision rate is 40 MHz and this sets the detector electronics clock. During the collision, not all the bunches collide. The average bunch crossing rate is lower than 40 MHz and we indicate it as v_{fill}. The luminosity is another important parameter indicating the collision rate. It includes the information of the proton beam densities (n_1, n_2), the bunch profile (the area of the overlap between the two beams) and the crossing rate (f):

$$L = f\frac{n_1 n_2}{4\pi\sigma_x\sigma_y}. \tag{3.1}$$

The above function gives the luminosity when the two identical beams are head to head. σ_x and σ_y are the standard deviations of the proton beam densities in the x and y directions assuming the distributions to be Gaussian [1]. The maximal luminosity designed for the LHC is $L_{\text{max}} = 10^{34}$ cm^{-2}s^{-1}. The total number of collision events N_{pp} for a certain time t is calculated as

$$N_{pp} = \sigma_{\text{inel}} \int_t L dt, \tag{3.2}$$

where σ_{inel} is the inelastic cross section. It is expected to be 80 mb at $\sqrt{s}$ =14 TeV in full phase space [87]. The average number of collisions per bunch is

$$\overline{n_{pp}} = \frac{N_{pp}}{N_{bx}} = \frac{L\sigma_{\text{inel}}}{v_{\text{fill}}}, \tag{3.3}$$

where N_{bx} is the number of bunch crossing for the time period. At the maximal design luminosity (10^{34} cm^{-2}s^{-1}), $\overline{n_{pp}}$ is expected to be 27. The designed luminosity for LHCb is 2×10^{32} cm^{-2}s^{-1} and its design philosophy is discussed in the next sections.

[1] The z direction is the beam axis and x, y directions are perpendicular to the beam, the precise definition can be found in the following section.

3.2 The LHCb Detector

The LHCb detector is designed for precise measurements in the b and c quark sectors. Its primary goal is to look for indirect evidence of new physics in CP violation and rare decays. Even though the results from current experiments agree with the Standard Model predictions within errors, Many theories do suggest extra sources of CP violation. Especially the current CP violation magnitude cannot explain the matter-antimatter asymmetry in the universe. The LHCb experiment will increase a lot the statistics accumulated for precise measurements and will use new detector technologies. It is currently the most suitable place for b physics study.

The mean flight distance of b hadrons is approximately 1 cm [88] in LHCb. A good vertex resolution is needed to separate b decay products from particles produced directly at pp collisions and to reduce large prompt background. The other collisions in the same bunch crossing which are called pile-up can significantly reduce the separation power of b decays and prompt background especially when running at maximal luminosity where the average collision number is 27. For this reason, the luminosity in LHCb needs to be reduced, it is focused less in LHCb than ATLAS and CMS. This process will not affect other experiments. The optimization of the luminosity depends on many parameter. Figure 3.2 shows the probability for 0, 1, 2, 3 or 4 inelastic collisions per bunch crossing as a function of the luminosity together with the $b\bar{b}$ production rate. The currently optimized average value is $L = 2 \times 10^{32}$ cm^{-2}s^{-1} which gives $\overline{n_{pp}} = 0.53$ for inelastic collisons. The maximal luminosity in LHCb will be 5×10^{32} cm^{-2}s^{-1} for nominal running conditions. Moreover, the reduced luminosity helps to reduce the event sizes and LHCb can then have a relatively loose trigger since the reconstructing and recording of the particles is always a challenge for hadron collider experiments. It will also reduce the radiative damage to the detector which is especially important for forward detectors like LHCb.

The estimated cross sections in LHCb are given in Table 3.1 [87]. The cross sections are re-scaled values from former experiments and have very large uncertainties. Figure 3.3 shows the angular distribution of the produced b-hadrons which are correlated between each other according to their production mechanism. In LHCb, the main process for the b production is through the gluon-gluon fusion process explained in Chapter 2. The two b quarks are produced in opposite directions in their center-of-mass frame and

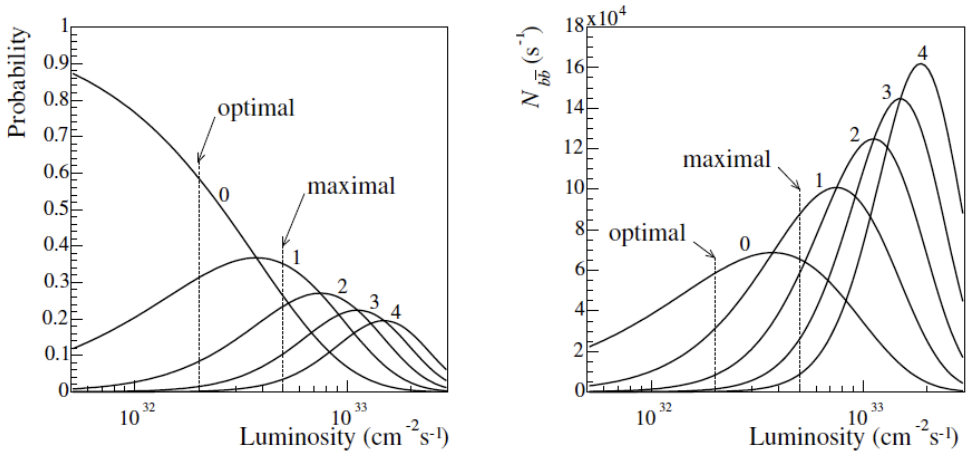

Figure 3.2: Left: Probability for 0, 1, 2, 3 or 4 inelastic collisions per bunch crossing versus luminosity. Right: The number of $b\bar{b}$ events per second with 0, 1, 2, 3, or 4 pile-up.

Table 3.1: Estimated cross sections at $\sqrt{s} = 14$ TeV [87]

Cross section	Value
Total	$\sigma_{\text{tot}} = 100$ mb
Inelastic	$\sigma_{\text{inel}} = 80$ mb
$c\bar{c}$	$\sigma_{c\bar{c}} = 3.5$ mb
$b\bar{b}$	$\sigma_{b\bar{b}} = 0.5$ mb

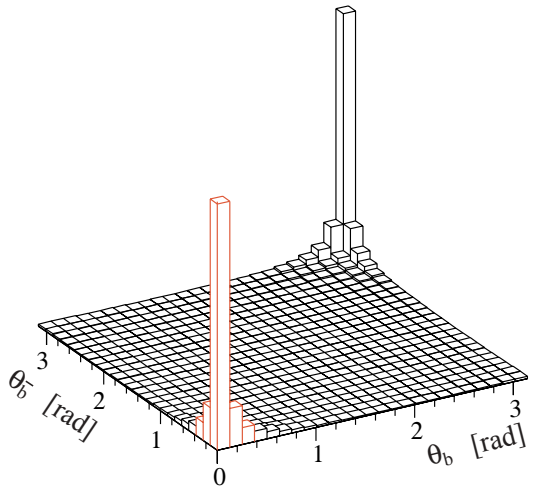

Figure 3.3: The angular distribution of the produced b-hadrons.

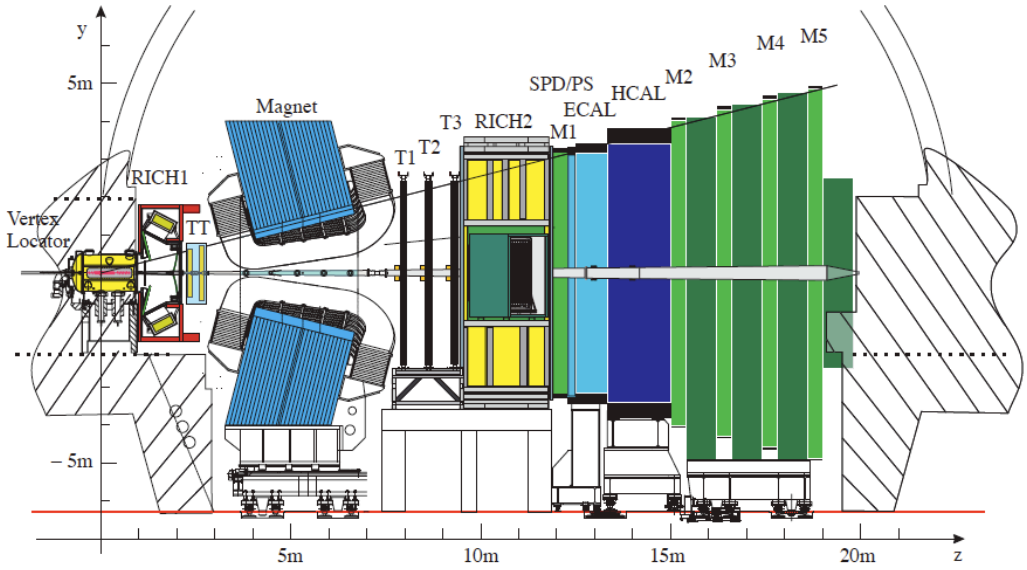

Figure 3.4: The LHCb detector layout, showing the Vertex Locator (VELO), the dipole magnet, the two RICH detectors, the four tracking stations TT, T1, T2, T3, the Scintillating Pad Detector (SPD), Preshower (PS), Electromagnetic calorimeter (ECAL) and Hadronic calorimeter (HCAL) and five muon stations M1–M5.

then strongly boosted in the same direction. The main regions for observing the two b hadrons are either in the forward region or in the backward region. The LHCb detector is thus designed as a forward spectrometer with only one arm. There are around 43% $b\bar{b}$ events with at least one b hadron in the LHCb detector. The experimental setup is shown in Figure 3.4 where the LHC beam "1" is coming from the left to the right.

The LHCb detector [89] consists of several subdetectors which can be categorized according to their functions:

- Tracking detectors: Vertex Locator (VELO), Tracker Turicensis (TT), Inner Tracker (IT), Outer Tracker (OT).

- Particle Identification (PID) detectors: two Cherenkov detectors (RICH1 and RICH2), the Scintillating Pad Detector (SPD), PreShower (PS), Electromagnetic CALorimeter (ECAL), Hadronic CALorimeter (HCAL) and Muon detectors (M1–M5).

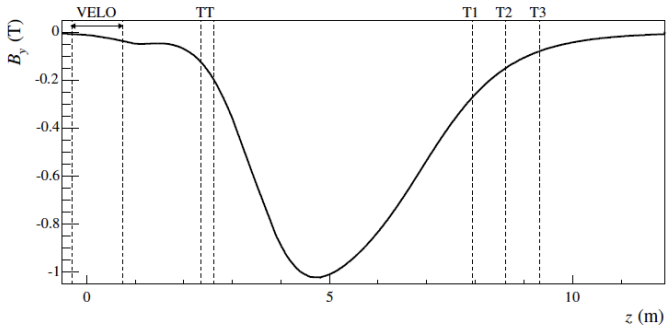

Figure 3.5: The main component of the magnetic field (B_y) in LHCb as a function of z.

Figure 3.4 also gives the description of the co-ordinate system used in LHCb. The z-axis is defined to be parallel to the beam pipe and the positive direction of the z axis is defined as pointing from the VELO to the muon detectors. The positive y-axis is pointing upwards while the positive x-axis is defined by the y-axis and z-axis to form a right-handed system. The acceptance of the LHCb detector is defined using the polar angle with respect to the z-axis. In the y-z plane (the vertical plane), the acceptance is 10–250 mrad while in the x-z plane (the horizontal plane), the acceptance is 10–300 mrad.

A magnetic field is needed to measure the momentum of the charged particles. It is provided by a magnetic dipole located after TT. The higher the momentum, the less bent is the track. To achieve a better precision for higher momentum, a strong B field is needed. The total integrated power of the magnet in LHCb is $\int Bdl \sim 3.7$ Tm on average. A relative precision of $\delta p/p \sim 0.4\%$ can be achieved for tracks with momentum $p \sim 40$ GeV/c [90]. The main component of the field is in the y direction and it is shown in Figure 3.5 as a function of z. The magnet can be reversed to study possible left-right detector-induced asymmetries. This motivates the choice of a warm magnet besides the cost and time needed for a superconducting magnet.

As mentioned above, the bunch crossing rate is 40 MHz while v_{fill} is approximately 30 MHz due to empty bunches in the LHC filling scheme. The rate is even lower since only inelastic pp collisions are interesting and furthermore, the events with b-hadrons are just a small part of these events as indicated in Table 3.1. A selective trigger is mandatory for experiments at a hadron collider otherwise the signal events may be lost due to the bottle neck for the event storage at the hardware level. Moreover, the rejection of

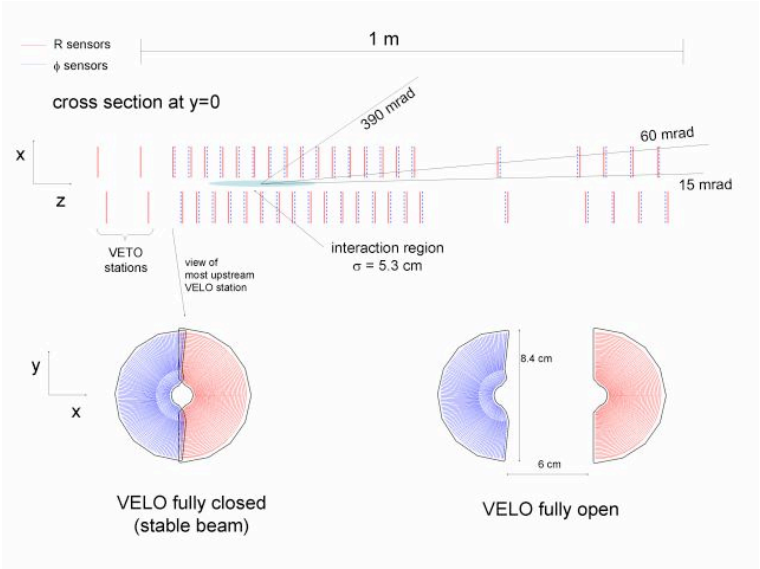

Figure 3.6: The arrangement of the VELO along the z-axis. Top: The cross section of the VELO to the plane $x - z$ at $y = 0$. The green region indicates the main collision region. Bottom: The cross section of the VELO to the plane $x - y$. During stable collisions, the left part overlaps with the right part while during the LHC beam injection, they will be retracted from the beam axis by 3 cm.

these non-b background events can largely reduce the data storage needs. In LHCb, the trigger is divided into two parts, Level 0 Trigger (L0) and High Level Trigger (HLT). L0 is a hardware trigger and HLT is a software trigger. They are discussed later on.

3.3 VELO

The VELO detector [91] is located around the collision point. It is dedicated to the separation between primary vertex and secondary vertexes. It is designed to be as close to the beams as possible to give a better reconstruction. In LHCb, the minimum distance of the VELO to the beam axis is 8 mm. The arrangement of the VELO detector is shown in Figure 3.6. The top figure shows the projection view from above. There are 21 VELO stations. Each station has one left and one right detector modules which consist of one R- and one ϕ-measuring sensors as shown in Figure 3.7. There are two

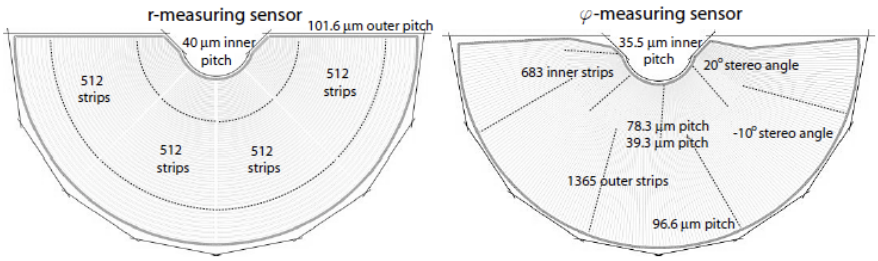

Figure 3.7: The lay-out of the r- and $\phi-$measuring sensors.

extra stations in the most negative part in the z direction with R-measuring sensors only. These two stations are called pile-up stations and they are used for the L0 trigger. The top figure shows the intersection of the VELO with the $y-z$ plane at $x=0$. The yellow region in the graph indicates the main interaction region. The probability density function for the interactions is approximately a Gaussian distribution with σ around 5.3 cm along the z axis. The VELO stations are arranged so that all the tracks coming from the region within 2σ range can be detected down to 15 mrad with respect to the z axis. A track in the LHCb spectrometer angular acceptance of 250 mrad $\times$ 300 mrad should cross at least three VELO stations. The 21 VELO stations are separated into two groups, 16 of them cover the central region and the rest cover these low angle tracks in the forward region for an optimized performance in the vertex reconstruction. The bottom figure in Figure 3.6 shows the cross section of the VELO to the plane $x-y$. During the normal running when the left parts overlap with the right parts, while in the LHC injection phase, the two halves are retracted from the beam axis by 3 cm for safety reason.

Two types of silicon sensors are used as indicated in Figure 3.7. One measures the R position of the tracks with strips circulating around the center. The inner pitch of the R$-$measuring sensor is 40 μm while the outer pitch is 101.6 μm. The R$-$sensor is divided into 4 regions of 45° which contain 512 strips in each. The $\phi-$sensor is separated into two regions. The inner regions of the sensor have a stereo angle of 20° for the edge strips. The pitch for the inner region varies from 35.3 μm to 78.3 μm. Each of the four regions of 45° contains 683 inner strips. The outer regions of the $\phi-$sensor have a stereo angle of $-10°$. The pitch varies from 39.3 μm (inside) to 96.6 μm (outside). Each of the four 45° regions contains 1365 inner strips. The variation of the pitch reflects the fact that there are fewer tracks when R

increases. The average occupancy per channel is well below 1%. The sensors are designed in the R$-\phi$ geometry so that it directly gives the projection in the $R - z$ plane which provides fast impact parameter information for the HLT1 trigger. The full impact parameter is only calculated in the HLT2 trigger and later during the analysis.

The whole VELO system is contained inside a vacuum vessel. The VELO vacuum is separated from the beam vacuum by a thin aluminum corrugated foil named RF foil. The RF foil provides protection against the electromagnetic pickup from the LHC beam.

3.4 Tracker Turicensis

The TT [92] is located after the RICH1 detector and in front of the magnet. It offers information for the HLT trigger and is used for the track reconstruction. As can be seen from Figure 3.5, particles in the TT are bent by a magnetic field of around 0.15 T and this can give a rough estimation of the track momentum with $20 - 40\%$ precision. Besides this, it also offers tracking information for long-lived particles like K_S^0, Λ which may decay outside the VELO.

The TT detector is housed in a detector volume with a temperature of 5°C. The TT covers the whole LHCb angular acceptance. It has four detection layers which are arranged into two pairs, (x, u) and (v, x). The two parts are separated from each other by approximately 27 cm along the LHCb beam line (z axis). The (x, u) and (v, x) are defined according to their angles with the y axis which are 0°, -5°, 5°, 0° respectively. This design is to make better spatial resolution in the horizontal plane for the track position.

The layout for the third TT layer (v) can be seen in Figure 3.8. Its dimension is 145 cm in the x direction and 132 cm in the y direction. The layout is composed of half modules which consist of a column of seven silicon sensors. In the region above and below the beam pipe, there is one half module on each side. From the middle to the edge, there are seven (first two layer) or eight (last two layer) half modules. According to different occupancies, the seven silicon sensors are divided into three groups labelled by different colors in Figure 3.8. The silicon sensors in the region labelled "M sector" have their own readout. The region closest to the beam pipe has

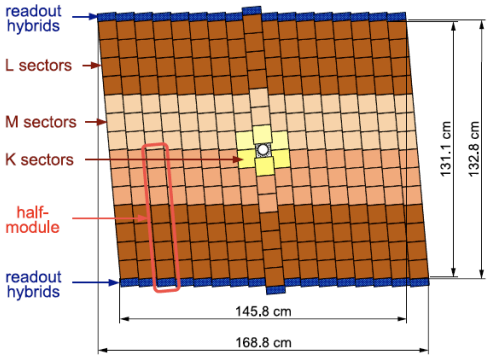

Figure 3.8: Layout of the third TT detection layer (v) with different readout indicated with colors.

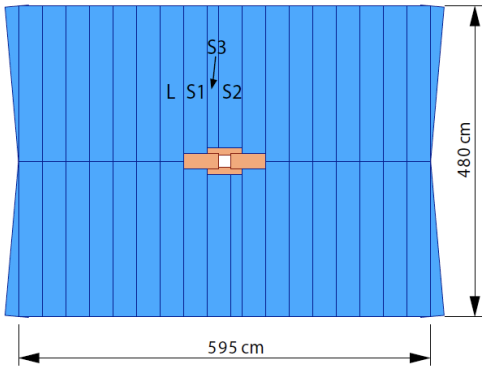

Figure 3.9: Layout of the T station with different colors for beam pipe, inner tracker, outer tracker.

a separate readout due to its high occupancy. The readout hybrids for all readout sectors are mounted at the end of the module.

3.5 T Stations

The T1–T3 stations are the main tracking system for LHCb. According to the different occupancies in different regions, each of them are divided into two parts: Inner Tracker (IT) and Outer Tracker (OT). The Inner Tracker also uses silicon sensors for the detection and together with TT, they are called Silicon Tracker (ST) [93]. The layout of one of the T stations is shown in Figure 3.9. The inner white box is the beam pipe region and the surrounding four orange boxes are the Inner Trackers. The outside region is the Outer Tracker. For each of the Inner Trackers, there are four layers. The stereo arrangement is the same as in TT, in a x-u-v-x topology. The Inner Tracker spans about 125 cm in width and 40 cm in height to cover the hottest region of the T stations. The average occupancy expected is less than 2%.

As for the IT and TT, the Outer Tracker has four layers for each station and has the same topology (x-μ-ν-x). For each layer, there are four different modules. In the region where there is no Inner Tracker, there are seven modules on each side. In the middle, there are three short ones (S_1, S_2, S_3) as indicated in the Figure 3.9. Each module has two monolayers of 64 gas-filled straw tubes except the S3 module (labelled in Figure 3.9) which has

only one monolayer. The OT is filled with a mixture of Argon (70%) and CO_2 (30%) with which a fast drift time less than two bunch crossings (50 ns), and a hit-coordinate resolution around 200 μm can be achieved.

3.6 Track Reconstruction

The track reconstruction program uses the hits in the VELO, TT, IT and OT to form particle trajectories. According to different locations of hits inside the detector, the tracks are defined into several categories:

1. Long tracks: Tracks that pass through the VELO to all the T stations. For our current study of J/ψ, only long tracks are used.
2. Upstream tracks: Tracks that traverse only the VELO and TT.
3. Downstream tracks: Tracks that pass through TT and T1–T3. These tracks are mostly from the decay of K_S^0 and Λ.
4. VELO tracks: Tracks that are only measured in the VELO. These tracks are used for the primary vertex reconstruction together with long tracks and upstream tracks.
5. T tracks: Tracks that only pass through T1–T3. They are mainly tracks from interactions with material.

A schematic illustration for the different types of tracks is shown in Figure 3.10. The track reconstruction starts from the seeding in the VELO and T1–T3 where the magnetic field is low. The VELO seeds are reconstructed by the measurement of R$-\phi$ values and they are considered to be straight lines. The initial track state without momentum information can be obtained from these track seeds. The T seeds are considered to be parabola since they still feel non-negligible magnetic field in the T stations. An initial state momentum can be estimated either from the bending of the tracks or assuming that the tracks come from the nominal interaction region. After having obtained the seeds, different algorithms are applied to form different types of tracks:

1. Long tracks: Two algorithms are applied for the long track search. The first one, called "forward tracking", starts from the VELO seeds [94].

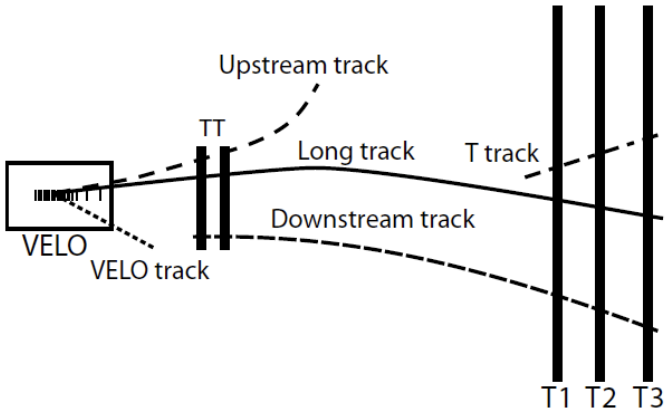

Figure 3.10: Schematic illustration of different types of reconstructed tracks.

The VELO seeds are combined with each hit in the T stations in turn to form a track. From the determined momentum and trajectory of this track, a search of hits in the other T and TT stations is applied. If enough hits are found in the defined window, a track is reconstructed and these hits are discarded before starting a new search. About 90% of the long tracks are found by this algorithm. Another algorithm then starts from the T seeds by extrapolating the track to the VELO [95, 96]. A track is found if they match the state of VELO seeds. 5% more long tracks can be found by this algorithm. The seeds and hits used are discarded before the next search.

2. Upstream and downstream tracks: The downstream and upstream tracks are found by relating the seeds in the VELO and T stations respectively to hits in the TT stations.

3. VELO and T tracks: The rest of the VELO and T seeds are stored as VELO and T tracks with poor momentum estimation.

After the track finding, a Kalman filter fit [97] is used to refine the parameter estimation. The quality of a track is defined by the χ^2 of the fit for a certain number of Degree of Freedom (nDoF). The resolutions on the momentum and impact parameters also reflect the quality of the tracks. The quality of the reconstruction algorithm is mainly defined by two parameters: reconstruction efficiency and ghost rate. The reconstruction efficiency in LHCb is normalized

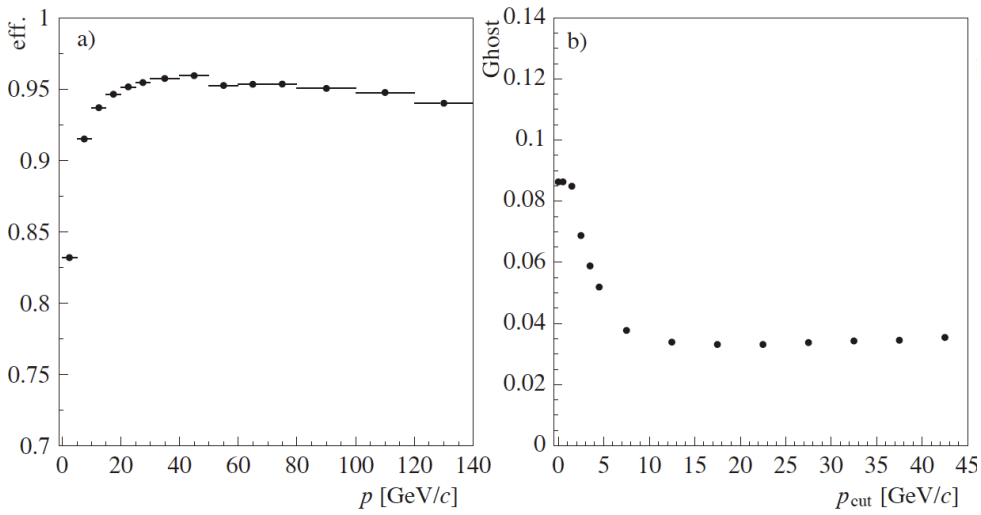

Figure 3.11: The reconstruction efficiency (left) and ghost rate (right) as a function of the track momentum (p) for long tracks.

to the number of reconstructible tracks. The requirements for each track type to be reconstructible are:

1. VELO tracks: Tracks that give at least 3 R$-\phi$ hits in the VELO.
2. T tracks: Tracks that give at least 1 x and 1 stereo hit in the T station.
3. Long tracks: Tracks that are reconstructible as VELO and T tracks.
4. Upstream tracks: Tracks that are reconstructible as VELO tracks and have at least 3 hits in the TT station.
5. Downstream tracks: Tracks that are reconstructible as T tracks and have at least 3 hits in the TT station.

A track is considered to be correctly reconstructed if 70% of its hits are related to a single Monte Carlo particle. Otherwise it is considered to be a ghost track. The reconstruction efficiency is defined as the fraction of correctly reconstructed tracks against all reconstructible tracks. The ghost rate is defined as the fraction of ghost tracks in the reconstructed tracks. The efficiency and ghost rate of long tracks are shown in Figure 3.11 as a function of the track momentum. It shows that the reconstruction efficiency is about 95% for long tracks while the average ghost rate is about 4%. The main inefficiency and large ghost rate are caused by the tracks with low p (or transverse

momentum p_T). These tracks have large multiple-scattering effects and it is less proable to find the hits within the window applied for the track finding. The relative momentum resolution ($\delta p/p$) is approximately 0.35% (0.5)% for long tracks with momentum of 10 (100) GeV/c. The impact parameter [2] resolution achieved for long tracks can be modelled as (14+35/p_T) μm with p_T in GeV/c.

In LHCb, the average number of reconstructed tracks in $b\bar{b}$ events is expected to be 72 while the average number of long tracks in $b\bar{b}$ events is expected to be 28. The long tracks contain 13.3 VELO hits, 3.7 TT hits and 11.7 (22.0) IT (OT) hits on average. Detailed information for other track types can be found in [89].

3.7 Vertex Reconstruction

The primary vertex in LHCb is reconstructed with the following iterative procedure:

1. A histogram with bin width 1 mm is filled with the z coordinate of the points on the VELO seed trajectories. The highest bin is chosen together with its four neighbours on each side. The barycenter is then calculated as the first estimation of the z coordinate of the primary vertex. The tracks in these bins form the original primary vertex.

2. Tracks with large χ^2 contribution to the vertex are eliminated and the remaining tracks are fitted again to a new vertex. This process is repeated until there is no track with a χ^2 contribution larger than 9 (225 for the first iteration to avoid losing proper tracks).

3. The above vertex with more than 6 tracks is kept as a primary vertex and the tracks which form the vertex are discarded. The process then iterates to search for the next primary vertex. The process stops if no more primary vertex can be found. If there is no vertex at all with more than 6 tracks, the original vertex is kept as the only primary vertex.

[2] The impact parameter is defined as the minimum distance from a primary vertex to a particle trajectory.

Table 3.2: Efficiencies for finding the $b\bar{b}$ production vertex in $b\bar{b}$ events as a function of the number of collisions producing at least two long tracks in the detector.

No. of collisions	1	2	3	4
Efficiency(%)	99	96	90	81

The efficiencies for finding the $b\bar{b}$ production vertex in $b\bar{b}$ events as a function of the number of collisions are listed in Table 3.2. The resolution for the reconstructed primary vertex is approximately 61 μm in the z direction and 10 μm in the x and y directions.

3.8 RICH

There are two Ring Imaging Cherenkov detectors (RICH) in LHCb designed mainly for π/K separation [98]. RICH1 is located after the VELO and before TT while RICH2 is located after T3 and before the calorimeters. The principle of the RICH detectors is based on the Cherenkov effect: light is emitted if the particle speed in the medium where it travels is larger than the speed of light in that medium. A light cone is formed around the traversing particle with an angle θ_c depending on the velocity of the particle:

$$\cos\theta_c = \frac{1}{n\beta}, \tag{3.4}$$

where n is the refraction index of the medium, β is the ratio between the velocity of the particle in the medium and the velocity of light c. The Cherenkov light is emitted only when $\beta > 1/n$. The speed of the particle is then measured from the angle of the light cone. Together with the momentum obtained from the tracking detectors, the mass of the particle can be calculated and so does the particle type. The velocity measurement is sensitive to the refraction index and different radiators are chosen for different momentum ranges. RICH1 covers the momentum range $2-60$ GeV/c with two different radiators. The first one is a 5 cm thick silica aerogel with $n = 1.03$ which is used for particle identification up to 10 GeV/c. The second radiator is a 85 cm long volume of C_4F_{10} gas with $n = 1.0014$. It provides the particle identification for the momentum range $10-60$ GeV/c. The RICH2 detector uses

CF_4 gas with even lower refraction index $n = 1.0005$. It can offer particle identification up to 100 GeV/c.

The RICH1 detector covers nearly the whole LHCb angular acceptance: from 25 mrad to 250 mrad in y direction and 25 mrad to 300 mrad in x direction. The RICH2 detector covers only up to 120 mrad in the horizontal plane and 100 mrad in the vertical plane. The light emitted by the medium in the detector is then reflected via spherical and flat mirrors with an efficiency around 85%. The light is then directed to photon detectors outside the detector angular acceptance region. The rings in the photon detectors are fitted in a global way. The fit procedure first assumes a pion mass hypothesis for each reconstructed track and then other mass hypotheses are tried (K, μ, p and e). The best fit amongst all mass hypotheses is used to reconstruct the rings.

3.9 Calorimeters

The LHCb calorimeter has four parts: SPD, PS, ECAL and HCAL [99]. It measures the energy deposits of the particles passing through or stopping inside and offers PID information. Furthermore, it is also one of the main parts of the L0 trigger which makes decisions according to the hit multiplicity in the SPD and the transverse energy deposited in the ECAL and HCAL.

The SPD (Scintillating Pad Detector) and PS (Pre-Shower) detectors are in front of the ECAL. Charged particles can ionise the scintillator of the SPD while neutral particles do not. This allows to distinguish between charged particles and neutral particles. After the SPD, there is a 12 mm thick lead wall which may initiate an electromagnetic shower. This shower is then detected by the PS detector which is also made of scintillators. The L0 trigger uses this information to distinguish between photons, electrons or π^0. The segmentations of the calorimeter detectors are similar according to the different particle fluxes in different detector regions. The layout is shown in Figure 3.12. The figure shows one quarter of the detector and is divided into 3 (2 for HCAL) regions with different granularities surrounding the beam pipe . The light emitted when charged particles cross the scintillators is collected by wavelength shifting (WLS) fibers and directed to photomultipliers (Multi-Anode Photomultipliers for SPD and PS) which are located outside the detector acceptance.

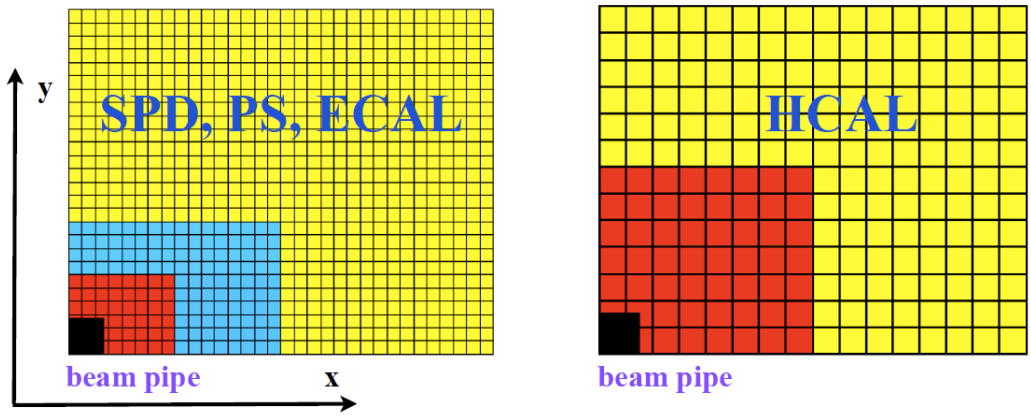

Figure 3.12: The segmentation of the calorimeters. Left: SPD, PS and ECAL. Right: HCAL. Only one quarter of the detector front face is shown.

The ECAL is a "shashlik" type detector. It consists of 4 mm thick scintillating tiles alternated with 2 mm thick lead plates. It offers a resolution given by

$$\frac{\sigma(E)}{E} = \frac{10\%}{\sqrt{E}} \oplus 1.5\%, \tag{3.5}$$

where E is in GeV. The HCAL is constructed out of 4 mm thick scintillator tiles alternated with 16 mm thick iron plates. The resulting resolution can be modelled as

$$\frac{\sigma(E)}{E} = \frac{80\%}{\sqrt{E}} \oplus 10\% \tag{3.6}$$

with E in GeV.

3.10 Muon Detectors

The muon detectors consists of 5 muon stations, M1−M5 [100]. They cover the acceptance region of $20 - 306$ mrad in the bending plane (x-z plane) and $16 - 258$ mrad in the non-bending plane (y-z plane). The detectors are instrumented with multiwire proportional chambers (MWPC) except the inner region of the M1 station where a triple-GEM foil is used. The MWPC is designed to satisfy the requirement of collecting signals within 25 ns.

The layout of the muon detectors is shown in Figure 3.13. The left part shows the side view of the muon detectors. M1 is placed in front of the

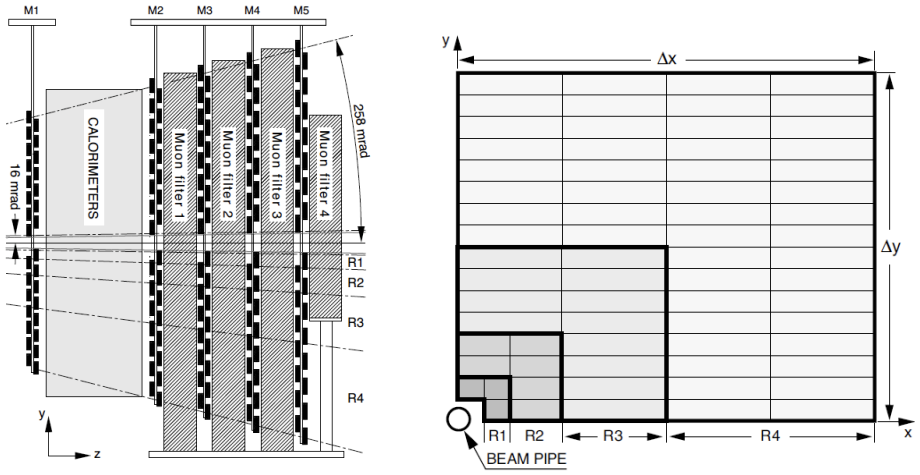

Figure 3.13: The layout of muon detectors. Left: Side view of the muon system. Right: Front view of a quadrant of a muon station.

calorimeter to achieve better resolution on the muon p_T measurement for both L0 trigger and full reconstruction. The p_T offered to the L0 trigger is reconstructed in a standalone and fast way. It uses the slope of the track between M1 and M2 with the assumption that muon tracks come from the interaction point. This gives a resolution $\delta p/p$ around 20%. The other four muon stations M2–M4 are located after HCAL and are separated by 80 cm thick iron plates filters. The iron plates are used to absorb hadrons which penetrate the whole detector. The minimum momentum of a muon to cross the whole muon stations is about 6 GeV/c since the number of interaction lengths from M1 to M5 is 20. The geometry of the muon stations is projective, meaning their transverse lengths scale with the distance to the interaction point as shown in Figure 3.13. This makes the reconstruction of muon tracks much easier.

The muon segmentation for one of the muon stations is shown in the right part in Figure 3.13. The layout shows one quarter of the muon station which is divided into four regions: R1–R4. The segmentation increases as the distance to the beam pipe increases like other LHCb detectors. The segmentation rate is 1:2:4:8 for R1–R4 and this offers approximately the same occupancy for each channel. The spatial resolution gets worse as the distance to the beam pipe increases. The spatial resolutions are also different for different muon stations. The first three muon stations offer better spatial resolutions which are used to measure the p_T and the direction of the tracks.

The M4 and M5 stations are mainly used for the particle identification with a little worse spatial resolution. They detect the particles penetrating through the whole detectors (these particles are usually muons) and this can distinguish the muons from other particles.

3.11 PID performance

The LHCb particle identification (PID) is achieved with the following subdetectors: RICH1, RICH2, calorimeters and muon detectors. In general, the two RICH detectors are used to distinguish hadrons like π, K; electrons are identified with the calorimeters and muons are identified by the muon detectors. The RICH detectors can also provide information for lepton identification; muons only deposit minimum ionisation energy in the calorimeters which can also be used as identification information. In LHCb, the PID likelihood is constructed by combining all the information from the PID detectors; for example the likelihood function for the muon hypothesis is

$$L(\mu) = L_{\mathrm{RICH}}(\mu) L_{\mathrm{CALO}}(\mu) L_{\mathrm{MUON}}(\mu), \tag{3.7}$$

where the subscripts of the different likelihood functions indicate different detectors.

The main contribution of the muon identification comes from the muon detectors. In the Monte Carlo sample used in our study, the MuonID algorithm consists of three main steps [101]:

1. Defining the field of interest (FOI): The sizes of the FOI are defined separately for each of the 4 regions of the muon system in all the four stations, M2–M5 [3]. The centers of the FOI are the points in the muon stations obtained by extrapolating the track direction in M1 to the rest of the stations. The size of the elliptic FOI around the center point is given by the momentum dependent function

   $$p_{0x,y} + p_{1x,y} \times \exp(-p_{2x,y} \times p). \tag{3.8}$$

   The parameters $p_{0x,y}, p_{1x,y}, p_{2x,y}$ are currently determined from Monte Carlo by maximizing the efficiency over the whole range while reducing

[3] Studies show that the M1 helps only a little in the muon identification. The M1 station is mainly used for the L0 Muon trigger and momentum measurement.

Table 3.3: Definition of IsMuon =1. For each given momentum range, at least one hit is required in each of the listed muon stations.

momentum range	muon stations
3 GeV/c < p < 6 GeV/c	M2+M3
6 GeV/c < p < 10 GeV/c	M2+M3+(M4 or M5)
p > 10 GeV/c	M2+M3+M4+M5

the misidentification rate to the percent level. The mean values and the RMS of the distance between the closest hits to the center points in each momentum bin for different events are obtained from Monte Carlo. The parameters are then extracted by fitting to the shape obtained by adding 3.5 RMS to the mean values in each momentum bin.

2. Setting a boolean value IsMuon: Each track is then marked with IsMuon according to their hits in the FOI for different muon stations. It is required to have at least one hit in the FOI in a number of stations which depends on the momentum of the tracks. The requirement is listed in Table 3.3.

3. Building the DLL (Delta Log-Likelihood function) for the muon identification: The misidentification rate is further reduced with the use of the average squared distance of the hits in the FOI to the center point which is defined as

$$D = \sum_{i=1}^{N} \frac{1}{N} \Big\{ (\frac{x_i - x_{\text{center}}}{\text{pad}_x})^2 + (\frac{y_i - y_{\text{center}}}{\text{pad}_y})^2 \Big\}. \tag{3.9}$$

The D distributions for muons and non-muons are currently obtained from Monte Carlo and are shown in the left part of Figure 3.14. They are noted as $\text{PDF}_{\mu}(D)$ and $\text{PDF}_{non-\mu}(D)$ separately. The probability for a track with the average squared distance D_0 to be compatible with the muon and non-muon hypothesis is then defined separately as

$$P_{\mu} = \int_0^{D_0} \text{PDF}_{\mu}(D)\text{d}D \qquad P_{non-\mu} = \int_0^{D_0} \text{PDF}_{non-\mu}(D)\text{d}D. \tag{3.10}$$

The DLL function is built as

$$\text{DLL} = \ln(P_{\mu}/P_{non-\mu}). \tag{3.11}$$

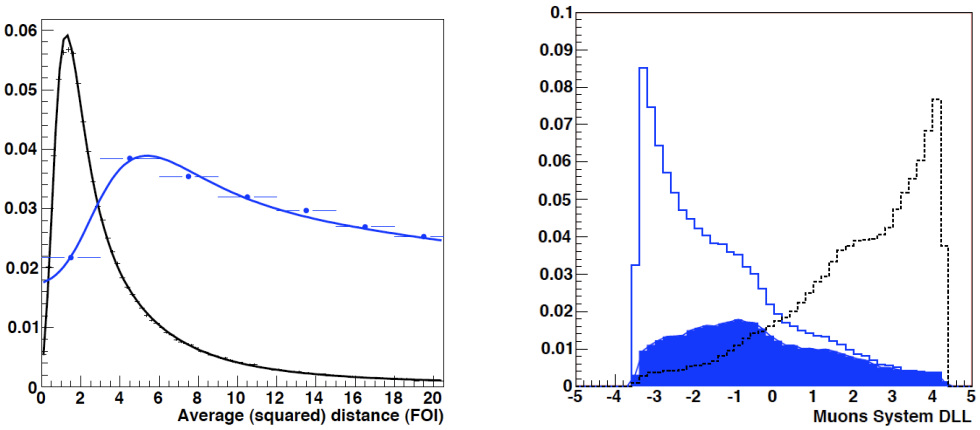

Figure 3.14: Left: Average squared distance from track extrapolation to hits inside the FOI, for muons (black cross) and non-muon tracks (blue circles). The fitted curves are superimposed on the graph. Right: DLL for muons (solid line) and non-muon tracks (dashed line) in the $B \to J/\psi K_S$ sample. The shaded area shows the contribution from the decays in flight.

The performance of the DLL algorithm is shown in Figure 3.15. The open and filled markers correspond to the results from a sample of $B \to J/\psi K_S$ and $b\bar{b}$ respectively. The upper curves give the efficiencies of the muon identification and the lower curves show the results of the muon misidentification ($\pi \to \mu$). For the $B \to J/\psi K_S$ sample, an efficiency of $(90.17 \pm 0.07)\%$ is obtained with a misidentification rate of $(1.41 \pm 0.01)\%$ when the cut DLL> -1.0 is applied.

After constructing the DLL of the muon detector [4], information from other sub-detectors is used to form a combined DLL. The identification of muon in the RICH detector is similar to the other particles. The velocity of the particle is measured in the RICH while the momentum is obtained from the track trajectory. The mass of the particle can be calculated and used as an identification for muon. In the calorimeters, the deposited energies in the ECAL and HCAL are also used for the muon identification. The distributions of the energy deposited in the ECAL and HCAL along the extrapolated particle trajectories for different particles are shown in Figure 3.16. The variables used for the ECAL and HCAL are $\tanh\frac{E_{\rm ECAL}}{5{\rm GeV}}$ and

[4]The DLL function described above is used in the DC06 simulation while for the data taken during the first running period, a more stable identification method [102] will be used for the muon PID due to the complicated running scenario.

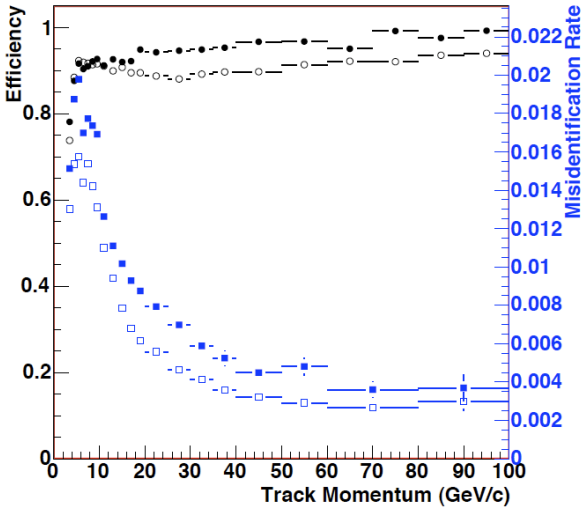

Figure 3.15: Muon identification efficiencies (circles) and pion misidentification rates (squares) as a function of momentum. The cut DLL> -1 was used to produce this plot. Open and filled markers correspond to the results from a sample of $B \to J/\psi K_S$ and $b\bar{b}$ respectively.

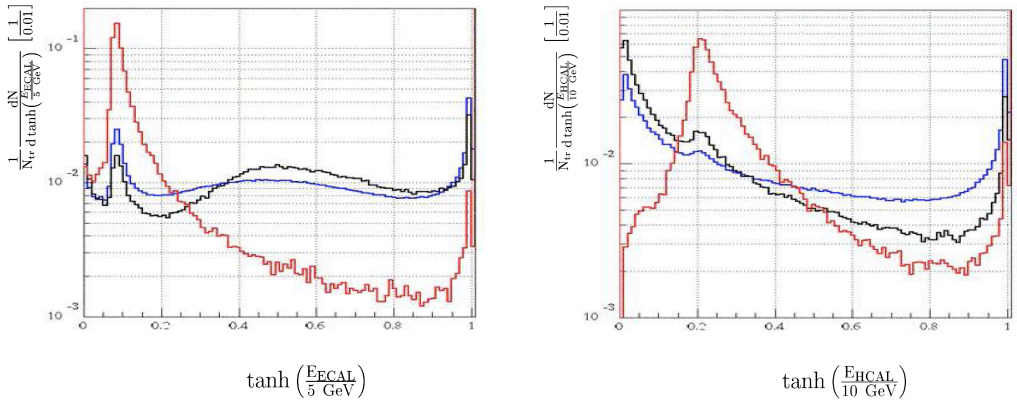

Figure 3.16: Distribution of the energy deposited along the extrapolated particle trajectory in the calorimeters, for muons (red line) and hadrons/electrons (blue line) and ghost (black histogram). Left: ECAL, Right: HCAL.

$\tanh\frac{E_{\mathrm{HCAL}}}{10\mathrm{GeV}}$ respectively. Clear minimum ionizing particle (MIP) peaks from muons can be found at $\tanh\frac{E_{\mathrm{ECAL}}}{5\mathrm{GeV}} \sim 0.1$ and $\tanh\frac{E_{\mathrm{HCAL}}}{10\mathrm{GeV}} \sim 0.2$. The DLL for muon and non-muon hypothesis in the calorimeters are then calculated on the basis of the two dimensional distributions of $\tanh\frac{E_{\mathrm{ECAL}}}{5\mathrm{GeV}}$ and $\tanh\frac{E_{\mathrm{HCAL}}}{10\mathrm{GeV}}$ as a function of $\tanh\frac{p}{25\mathrm{GeV}}$.

For the first data, taking into account that other sub-detectors may not be properly calibrated, a simple cut will be applied on the energy deposited in the ECAL and HCAL to improve the rejection power.

3.12 Trigger

The interaction rate in LHCb will be 40 MHz with an average data size of 35 kb. It is thus impossible to record all the events because of the time needed for the reconstruction and writing to the permanent disk storage. A trigger system [103] is needed to select the interesting events otherwise b events may be lost when writing minimum bias events. The event rate must be dramatically reduced since the b events we are interested in are just a small fraction as can be seen from the cross sections in Table 3.1. These b events have the following signatures:

1. Large transverse momentum of the B decay products due to the large mass of the B hadrons.

2. Large impact parameters of the B decay products due to the long lifetime of the B hadrons.

With these signatures different from the minimum bias events, the trigger will then be optimised according to the off-line selected events.

Since it is impossible to fully reconstruct the collision events at the rate of 40 MHz, a successive strategy is needed. The initial stage should use a fast algorithm to reconstruct several variables like p_T or E_T and then loose cuts on these events will be applied. This stage is aiming at reducing obvious background events and some very hot events with very high multiplicities. This part is realized at the hardware level and is called Level 0 trigger (L0). Events passing through L0 are sent to the LHCb computer farm, which makes further reductions. The trigger at this level is a software trigger and is called

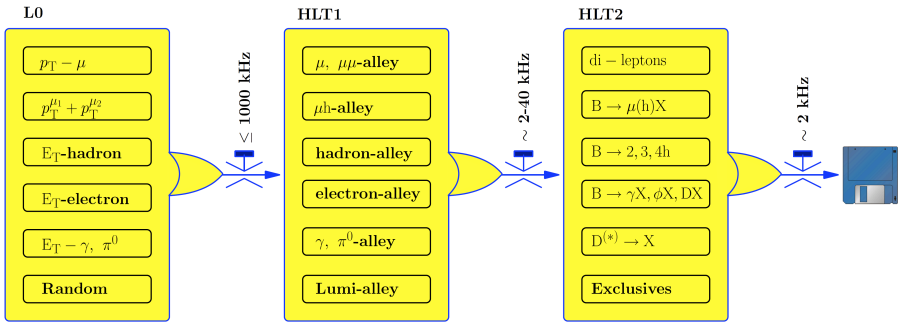

Figure 3.17: Architecture of the LHCb trigger.

Table 3.4: Trigger scenarios according to different running conditions.

Interaction rate	Trigger Scenario
< 2 kHz	L0: Minimum bias trigger + random trigger
< 0.3 MHz	L0: Loose, HLT1: nominal, HLT2: absent or very loose
0.3-1 MHz	L0: Depending on farm size, HLT1: nominal, HLT2: loose
> 1 MHz	L0: Hard cuts, HLT1: nominal, HLT2: nominal

High Level Trigger (HLT). There are two main procedures: first the results from L0 is further confirmed with better reconstruction of the selected events and then different exclusive selections are applied on the events passing the confirmation step. The two steps are called HLT1 and HLT2. The trigger principle under nominal running condition is shown in Figure 3.17. The L0 trigger reduces the output rate to about 1 MHz. The rate is further reduced by the HLT1 confirmation to about 2-40 kHz. The final output rate of HLT2 is around 2 kHz. During the first year, triggers will be set according to different running scenarios as shown in Table 3.4. At the very beginning with a low collision rate, only very loose selections on the transverse energy deposited in the calorimeters will be used to reject background events. Random trigger will also be applied for the efficiency study and luminosity measurement at this stage. As the rate increases, tighter triggers will be applied to decrease the rate to an acceptable value.

In this thesis, we only consider the effect of the L0 trigger (HLT trigger is treated in the same way, if applied). The detailed selections for the L0 trigger at the nominal running conditions are summarized below.

3.12.1 L0 Trigger

The input rate of the L0 trigger is 16 MHz of inelastic pp collisions with around 100 kHz of collisions with a $b\bar{b}$ pair. The maximum output rate of the L0 trigger is fixed to 1.1 MHz which means that the accepted events should be transmitted to the HLT within 900 ns. The L0 trigger decision is made 4 μs after the collision and during this time, up to 160 bunch crossings are stored in the front-end electronics. The L0 trigger receives information from three subsystems: the calorimeter trigger, the muon trigger and the pile-up trigger.

The pile-up system uses the two VELO stations in the upstream region with only R sensors. These two sensors have fast readout for the trigger and they record the R position of tracks passing through them. The z positions of these tracks are calculated by combining each hit in the two stations. The calculated z positions are histogrammed and the position of the primary vertex is the bin with the highest number of the entries. The pile-up trigger requires the number of tracks in the second vertex to be less than 3. This trigger then vetoes the bunch crossings with multiple collisions. Complicated events are also rejected if the pile-up multiplicity is more than 112 or the SPD multiplicity is more than 280. These events are rejected at the L0 trigger level because their offline reconstruction will fail.

The energy deposited in the ECAL and HCAL is also used to trigger interesting events. The clusters are identified as electrons, photons, or π^0 using the information from the SPD and PS. For the hadron clusters in the HCAL, the energy deposited in the ECAL in front of the HCAL cluster is added for the trigger. The calorimeter trigger requires the sum of the transverse energy for the HCAL (SumEt) to be more than 5 GeV, where SumEt is the sum of all highest 2×2 clusters found in the HCAL. This selection together with the three selections (2 pile-up and 1 SPD selections) are called Global Event Cuts (GEC) [5]. An event passing GEC is accepted if it contains a calorimeter cluster with E_t larger than 3.5 GeV for hadrons, 2.6 GeV for electrons, 2.3 GeV for photons or 4.0 GeV for neutral pions.

Additionally there is a di-muon trigger and a single muon trigger for triggering muon channels. The di-muon trigger accepts an event if it passes

[5]Current studies on the GEC show that GEC help only a little in reducing the background events; they may not be used for the real data.

GEC and the sum of the transverse momenta (p_T) of the two muons with the largest p_T exceeds $1.48\,\mathrm{GeV}/c$. The single muon trigger accepts an event either if it passes GEC and contains a muon with p_T larger than $1.28\,\mathrm{GeV}/c$ or if it passes SumEt selection and with p_T larger than $1.48\,\mathrm{GeV}/c$. The three muon triggers offer a robust selection of $J/\psi \to \mu\mu$ events. We summarize the L0 trigger in Table 3.5. For the current running in 2010, it uses looser selections.

Table 3.5: L0 trigger summary.

Trigger	selection criteria
Di-muon Trigger	GEC + sum of two largest muon $p_T > 1.48\,\mathrm{GeV}/c$
Single muon Trigger	GEC + p_T >$1.28\,\mathrm{GeV}/c$
Global single muon Trigger	SumEt + $p_T > 1.48\,\mathrm{GeV}/c$
Hadron Trigger	GEC + $E_t > 3.5\,\mathrm{GeV}$
Electron Trigger	GEC + $E_t > 2.6\,\mathrm{GeV}$
Photon Trigger	GEC + $E_t > 2.3\,\mathrm{GeV}$
Neutral Pion Trigger	GEC + $E_t > 4.0\,\mathrm{GeV}$

3.12.2 HLT

HLT is a C++ application which runs on a computer farm. In principle, the full detector information of each event can be accessed at this stage, but due to the limited computer power, only part of the information is used. However, since it is fully implemented in software, it is flexible and can be improved with more knowledge from the first real data.

As described above, HLT consists of two steps: HLT1 and HLT2. HLT1 confirms the results by reconstructing particles in the VELO and T stations. It consists of a series of alleys which correspond to different types of L0 trigger. If one of the alleys is fired, the event passes the HLT1 trigger and is sent to the HLT2 trigger.

The output rate of HLT1 is sufficiently low for an offline-track reconstruction except from the Kalman filter to obtain a full covariance matrix. Information like invariant mass, distance, *etc* can be used as discriminating variables. For common particles such as J/ψ, K_S, there are inclusive lines to

avoid duplication. Exclusive lines use loose selection criteria to reduce the total rate down to 2 kHz. The final trigger is the logical OR of the inclusive and exclusive selections.

3.13 Online System and Data Acquisition

The LHCb online system controls the data path between the Front-End boards in the various sub-detectors to the final storage [104]. It also makes sure different subdetectors are properly synchronized to the LHC clock. It consists of the following components:

1. The Data AcQuisition system (DAQ): The DAQ collects the zero suppressed data corresponding to triggered events. It also filters and fully reconstructs interesting events. It dispatches these events to the permanent storage.

2. The Timing and Fast Control (TFC): The TFC distributes the beam synchronous clock and various synchronous resets and fast control commands via optical fibers to the Front-End electronics.

3. The Experiment Control System (ECS): The ECS works in parallel to all the operations described previously. It configures the readout system and monitors the state of the subdetectors. It steers the actual data taking and provides checks of the quality of the data recorded for physics analysis.

3.14 LHCb Software

In LHCb, the software is now maintained through the Concurrent Versioning System (CVS) to record the history of source files [6]. Each package in LHCb is managed by the Configuration Management Tool (CMT [105]) which handles the compiling, linkers, *etc.* The LHCb framework which combines all the packages together and offers general applications for the users is called Gaudi which is also widely used by many other experiments like ATLAS,

[6]Currently the CVS service at CERN is being gradually dismissed and all the projects are being migrated to SubVersioN (SVN).

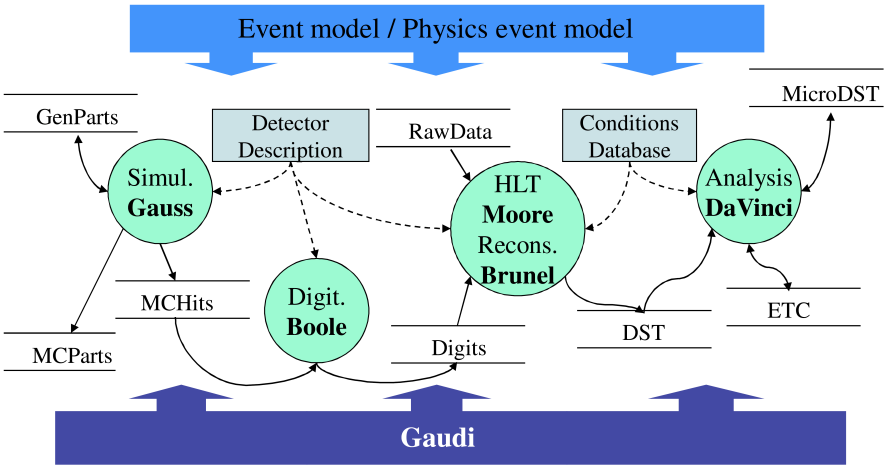

Figure 3.18: Schematic graph of the LHCb projects and their relationship.

Daya Bay. It is a framework for event-processing applications which is very suitable for high-energy physics analysis. It is an object-oriented framework written in C++. It offers a general interface to different dedicated packages and provides most of the common functionality. The packages with similar purpose are combined together and called a project. The schematic graph of the LHCb projects is shown in Figure 3.18. These projects are defined as follows:

1. Gauss [106]: The LHCb Gauss project handles the Monte Carlo simulation of the experiment. It includes two main part: event generator and detector simulation. The main generator in LHCb is PYTHIA [107]. It simulates the pp collision both in the inclusive mode like minimum bias events and in the exclusive mode like a dedicated B hadron production. Besides PYTHIA, other generators like HERWIG [108] are also implemented in LHCb and used for the Monte Carlo study. It is also possible to implement generators with dedicated purposes. In fact, the groups in Beijing and in Orsay work together and implement the BCVEGPY [109, 110] into Gauss for the B_c study [7]. The spillover from the previous bunch crossing is added in this stage [8]. After the generation of the interesting particles, the decay of B hadrons are handled by EVTGEN [111] which provides the possibility to deal with the complex

[7] Part of my thesis work is to implement the B_c excited states into the BCVEGPY and Gauss.

[8] It was done in Boole before.

B decays. The evolution of the generated particles is simulated by the GEANT4 toolkit [112]. It describes the detector structure, material used, magnetic field, *etc.* It also takes care of the interactions for the particles going through the detector.

2. Boole [113]: The Boole digitization is the final stage of the LHCb detector simulation. It converts the hits from GEANT4 simulation into a detector response. It takes care of the readout electronic response and the L0 trigger hardware emulation. The output data is the digitized data which has the same format as the one from the real detector.

3. Moore [114]: The Moore project is the application for the HLT. It is designed to work both online and offline. The data from Boole or from the LHCb DAQ system is sent to it. It runs on the trigger farm.

4. Brunel [115]: The Brunel processes the data output from the Boole software or from the LHCb DAQ system. It reconstructs the pp collision events from the digitized data. It contains the pattern recognition algorithm for the RICH detector, the tracking finding algorithms to reconstruct the charged tracks, *etc.* The simulated sample used in this thesis is reconstructed by Brunel.

5. DaVinci [116]: Physicists analyze the output of the Brunel software with DaVinci. The analysis programme is written in C++ and takes benefits from different libraries inside [9].

6. Panoramix [117]: The Panoramix application deals with the event display in LHCb.

7. Ganga [118]: The GRID distributed computing model is used for the LHCb analysis due to the large amount of data collected and due to the complicated analysis requirements from all over the world [119]. The Monte Carlo samples and the real data samples are delivered to all over the world (Tier-1, Tier-2). When a job is submitted, it is executed at the places where the data is located. The handling of the job submission and of the data retrieving process is done by Ganga.

[9] GaudiPython is also used in LHCb analysis depending on personal taste.

Chapter 4

Monte Carlo Study on J/ψ Cross Section Measurement

In this chapter, the strategy of the J/ψ differential cross section measurement is given using fully simulated Monte Carlo samples, together with a discussion of the possible systematic errors. At the beginning, the software environment settings and the parameters used for the production of the Monte Carlo samples are summarized. Then the J/ψ selection criteria based on a minimum-bias sample are chosen. The performance on the mass reconstruction and the production rate at $\sqrt{s} = 14$ TeV are estimated according to our selections. After the J/ψ reconstruction, the two components, J/ψ from b-hadron decays and prompt J/ψ, are separated according to their different properties described in Chapter 2. The distinction of J/ψ from charmonium excited state decays is not discussed in this thesis. After separating the two contributions, the cross sections (corrected with the efficiencies and with the integrated luminosity) and polarization (see Chapter 5) are given in different p_T and η bins.

The absolute production cross section of a particle is given by

$$\sigma_x = \frac{N_x}{\mathcal{L} \times \epsilon_x \times \mathcal{B}}, \tag{4.1}$$

where σ_x is the cross section to be measured, $\mathcal{L}$ is the integrated luminosity during the period of time analyzed, $\mathcal{B}$ is the branching ratio for the decay channel of the particle studied. This thesis uses the decay channel $J/\psi \to \mu^+\mu^-$ to measure the differential cross section since in hadron collider experiments, it is very easy to achieve a clean signal sample for it. The

currently measured branching ratio of $J/\psi \to \mu^+\mu^-$ is $(5.93 \pm 0.06)\%$ [33]. In order to obtain the b-hadron differential cross section, the branching ratio of the inclusive decay channel $H_b \to J/\psi + X$ should also be considered, the currently measured value is $(1.16 \pm 0.10)\%$ [33]. N_x is the number of the reconstructed events of the decay channel during the considered period of time. For the prompt J/ψ differential cross section measurement, it is the number of observed prompt decay $J/\psi \to \mu^+\mu^-$. For the J/ψ from b-hadrons, it is the number of observed $H_b \to J/\psi(\mu^+\mu^-) + X$. ϵ_x is the total efficiency of the decay channel. The total efficiency includes three parts: acceptance efficiency, reconstruction and selection efficiency and trigger efficiency. They are discussed separately in the following sections. After the efficiency discussion, the principles of the luminosity measurement together with their expected precisions are given. At the end, the final results of the differential cross section measurement and its comparison with the input values are given.

4.1 Monte Carlo Settings in Data Challenge in 2006

During the data challenge in 2006 (DC06), the Gauss simulation software (see Chapter 3) is based on the PYTHIA generator [107] (version 6.325 with the old multiple interaction model) to produce pp collisions and on the GEANT4 package [112] (version 7.1) for the detector simulation. Only color singlet terms are included in this PYTHIA version for the direct J/ψ production. At the leading-order terms, they are: $gg \to J/\psi\, g$ [56, 49, 50, 51] and $gg \to J/\psi\, \gamma$ [120]. The charmonium excited states are produced through the processes (leading order color singlet terms) $gg \to \chi_{c0}\, g$, $gg \to \chi_{c1}\, g$, $gg \to \chi_{c2}\, g$ [121], *etc.* In the above production, J/ψ from $\psi(2S)$ decays are not included due to the limitation of the LHCb simulation at that time that J/ψ and $\psi(2S)$ cannot be produced at the same time. As discussed in Chapter 2, the cross sections of J/ψ and charmonium excited states are determined by the square of the wave function at $\vec{x} = 0$ and the squared derivative of the wave function at the origin (for χ_c). The values chosen for the generation [59] in the DC06 simulations are:

$$|R(0)|^2 = 0.7\,\mathrm{GeV}^3; \tag{4.2}$$

$$\frac{|R'(0)|^2}{m^2} = 0.006\,\mathrm{GeV}^3, \tag{4.3}$$

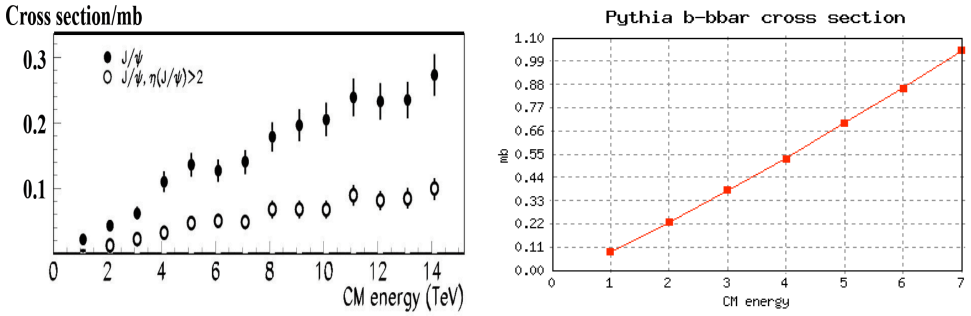

Figure 4.1: Production cross sections as a function of proton-proton center-of-mass energy: J/ψ (left) and $b\bar{b}$ (right)

where $R(r)$ is the radial wave function and m is the mass of the c quark. The generated cross sections of the different processes also depend on the parton density function (PDF) set used for the generation. In LHCb, it is the CTEQ6 PDF set from a fit with leading order hard cross sections using leading order α_s [122]. As only CSM terms contribute to the production, the total cross section simulated at $\sqrt{s} = 1.92$ TeV (Tevatron center-of-mass energy) is smaller than the CDF measurement and the p_T distribution decreases more quickly [1].

Table 4.1: The prompt charmonium cross sections at $\sqrt{s} = 14\,\text{TeV}$, in 4π, obtained with LHCb PYTHIA DC06 tunings.

process	cross section
$gg \to J/\psi\, g$	$65.0 \pm 1.2\,\mu$b
$gg \to \chi_{c0}\, g$	$609.3 \pm 3.7\,\mu$b
$gg \to \chi_{c1}\, g$	$151.6 \pm 1.9\,\mu$b
$gg \to \chi_{c2}\, g$	$654.2 \pm 3.8\,\mu$b
$gg \to J/\psi\, \gamma$	$1.2 \pm 0.2\,\mu$b

The cross sections of different contributing processes obtained with this configuration, at a center-of-mass energy of 14 TeV, and in 4π, are shown in Table 4.1. The results at $\sqrt{s} = 14$ TeV are extrapolated by PYTHIA, the change of J/ψ production cross section as a function of proton-proton center-of-mass energy is shown in Figure 4.1. In the simulation, the J/ψ production grows linearly as the proton-proton center-of-mass energy increases. The

[1] This is one of the reasons why $p_T \in [0, 7]$ GeV is set as our analysis range.

Table 4.2: Charmonium branching fractions of decays to J/ψ [123].

decay mode	branching fraction
$\chi_{c0} \to J/\psi\,\gamma$	2 %
$\chi_{c1} \to J/\psi\,\gamma$	38 %
$\chi_{c2} \to J/\psi\,\gamma$	19.9 %

relevant branching ratios used in the simulation are shown in Table 4.2. It is a little different from Table 2.1 shown in Chapter 2 as in the DC06 simulation, the values are from an earlier PDG version. Combining the numbers listed in Table 4.1 and Table 4.2, the total cross section obtained for the prompt J/ψ production is 256 μb in the DC06 simulations and the contributions from other charmonium states are around 75%. This number is different from the CDF measurement where the fraction of J/ψ from excited charmonium states is around 33%. The difference mainly comes from large cross sections of excited charmonium states. With further consideration of the contributions from b-hadron decays, the total cross section of J/ψ at $\sqrt{s} = 14$ TeV is 286 μb. For the 2010 data, as the LHC is running at $\sqrt{s} = 7$ TeV, the total cross sections of both J/ψ and b-hadron decrease and their dependence on the pp center-of-mass energy is shown in Figure 4.1. The cross sections for both of them are half the cross sections at $\sqrt{s} = 14$ TeV.

The J/ψ is produced as a mixture of different spin states and its initial polarization is determined by the spin density matrix. In the current DC06 simulation, the matrix is diagonal with the diagonal elements set to be 1 which means the produced J/ψ are un-polarized. In the LHCb simulation, the settings of different polarization states in different reference frames can be changed through the spin density matrix [82]. The decays of J/ψ and b-hadrons are controlled by the EvtGen package [111]. QED radiative corrections to the decay $J/\psi \to \mu^+\mu^-$ are generated using the PHOTOS package [124] (version 2.15), where the so-called exponentiation method is activated (see [124] for details about the implementation). The fraction of $J/\psi \to \mu^+\mu^- + n\gamma$ ($n > 0$) is around 30% [2]. Figure 4.2 shows the di-muon invariant mass distribution of radiative decays and non-radiative decays. The magenta data point is the di-muon invariant mass distribution of the non-

[2]A $J/\psi \to \mu^+\mu^-$ decay is considered to be a radiative decay if the decay products contain at least one γ in the simulation.

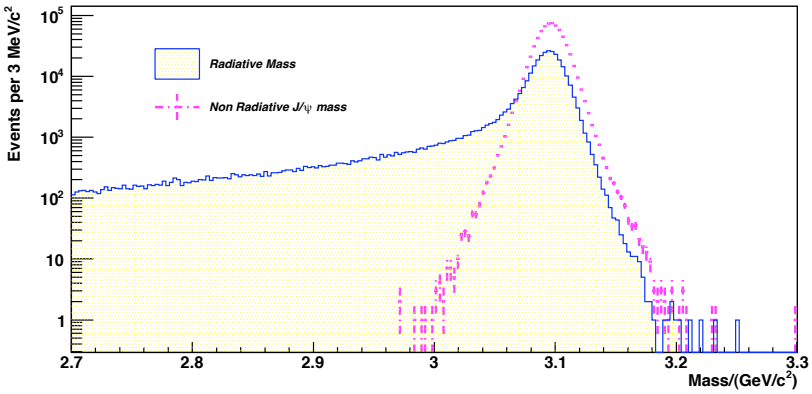

Figure 4.2: Di-muon invariant mass distributions of radiative decays and non-radiative decays after full simulation.

radiative decays and the yellow filled region is the one of radiative decays. The J/ψ events with a di-muon invariant mass smaller than 3 GeV/c^2 are all underwent radiative decays and this part must be taken into account during the fit of J/ψ mass distribution.

4.2 DC06 Simulation Results

According to the above settings, different distributions at the generator level are obtained. As the distributions depend on the selection criteria used, we list below some of the criteria mentioned in this thesis:

1. Full angular space: 4π angular space region without any restrictions on J/ψ and its decay products μ^+, μ^-.

2. J/ψ in the LHCb detector: the angle between the J/ψ momentum and z axis (defined in Chapter 3) is within [0, 400] mrad [3]. This selection requirement can largely reduce the simulated J/ψ sample size and the produced sample is sufficient enough to obtain the acceptance efficiency.

3. J/ψ $\eta \in [3, 5], p_T \in [0, 7]$ GeV/c: This is the phase space region where the study on the differential cross section and polarization is performed.

[3]The range is a little larger than the real detector acceptance to avoid losing possible J/ψ signal events, for example, some of the J/ψ with angle equal to 0 can be reconstructed by the LHCb detector while these J/ψ are outside the LHCb detector.

Table 4.3: $J/\psi \to \mu^+\mu^-$ production cross sections at $\sqrt{s} = 14\,\text{TeV}$ and b fractions in the J/ψ sample. The errors on the b fractions are less than 1%.

Selection criteria	Cross section	b fraction (event)	b fraction (J/ψ mother)
4π solid angle	17 μb	6.79%	5.54%
$\eta \in [3,5], p_T \in [0,7]\,\text{GeV/c}$	2.82 μb	5.80%	5.41%
$J/\psi \to \mu\mu$ in LHCb acceptance	2.19 μb	6.24%	5.85%
After selection (see Sec. 4.3)	0.81 μb	6.52%	5.70%

It only has restrictions on the J/ψ phase space and no restrictions on the decay products μ^+ and μ^-.

4. $J/\psi \to \mu^+\mu^-$ in the LHCb detector: the angle between the J/ψ momentum and the z axis is within [0, 400] mrad, and the angles between the μ momenta and the z axis are both within [10, 400] mrad.

For events with multiple J/ψ, only one of the J/ψ is required to be within the above defined region.

The b fractions in the J/ψ samples are listed in Table 4.3. There are two ways to define the b fraction:

- *b event fraction*: In the J/ψ event sample, it is the fraction of events containing a b-hadron, which can either come from the same pp interaction than the J/ψ or from a pile-up interaction in the same event,
- *Fraction of $b \to J/\psi + X$*: It is the fraction of J/ψ which come from the decay of a b-hadron.

The first definition not only includes events with $b \to J/\psi + X$, but also events with J/ψ and b produced together and b does not decay to J/ψ. The second definition is the one we are interested in and which is used as *b fraction* hereafter. From Table 4.3 we can see that the J/ψ from b-hadron decays are around 5–7% and they are different for different selection criteria due to the different phase space distributions of the prompt J/ψ and J/ψ from b decays.

Figure 4.3 shows the generator level distributions of the J/ψ transverse momentum p_T, pseudo-rapidity η, the cosine of the angle between the μ^+

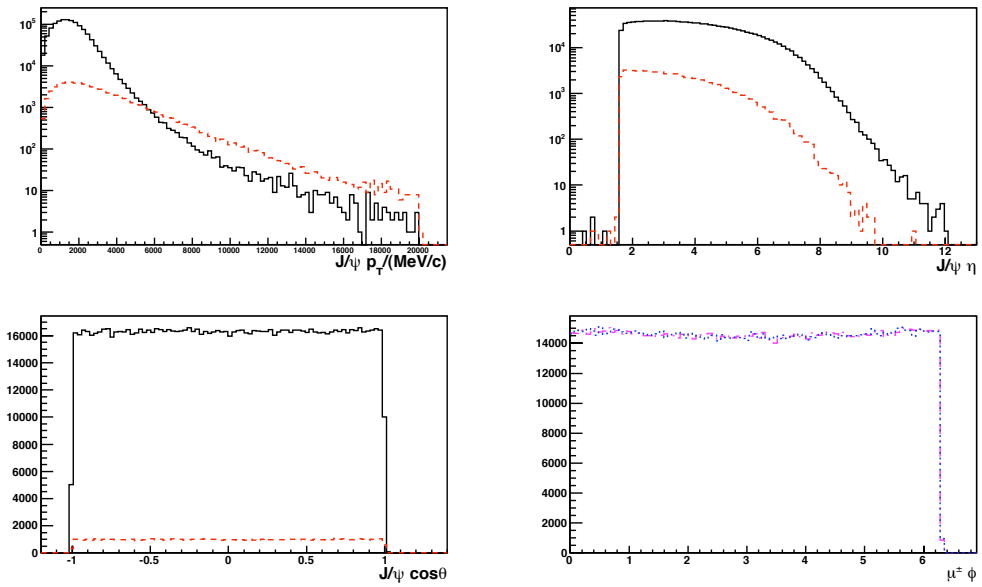

Figure 4.3: Various generator-level distributions including J/ψ transverse momentum p_T, pseudo-rapidity η, the cosine of the angle between the μ^+ momentum in the center-of-mass frame of J/ψ and J/ψ momentum in the proton-proton center-of-mass frame, and the azimuthal angles of μ^+ and μ^- in the laboratory frame. The sample is produced with J/ψ in the LHCb detector. In each graph, the red dashed line represents J/ψ from b-hadron decays and the black solid line represents prompt J/ψ. In the fourth graph, the blue dashed line represents the azimuth angle of μ^+ and the magenta dash-dot line represents the azimuth angle of μ^-. The prompt and retarded components are the same in this graph.

momentum in the center-of-mass frame of J/ψ and J/ψ momentum in the proton-proton center-of-mass frame and the azimuth angles of μ^+ and μ^- in the laboratory frame [4]. The sample is produced with J/ψ in the LHCb detector. The first three graphs show the distributions of the prompt J/ψ (red dashed lines) and J/ψ from b hadrons (black solid lines). As expected, J/ψ from b-hadron decays have a harder p_T distribution while they have a similar η distribution as the prompt J/ψ. The simulated J/ψ are mainly distributed in the region $\eta \in [2, 6]$. The $\cos\theta$ distributions of the prompt J/ψ and J/ψ from b-hadron decays are flat due to the non-polarization settings in the simulation. The last graph shows the azimuthal-angle distributions

[4] In the DC06 simulation, as there is no crossing angle between the two proton beams, the laboratory frame is the same as the center-of-mass frame of the two proton beams.

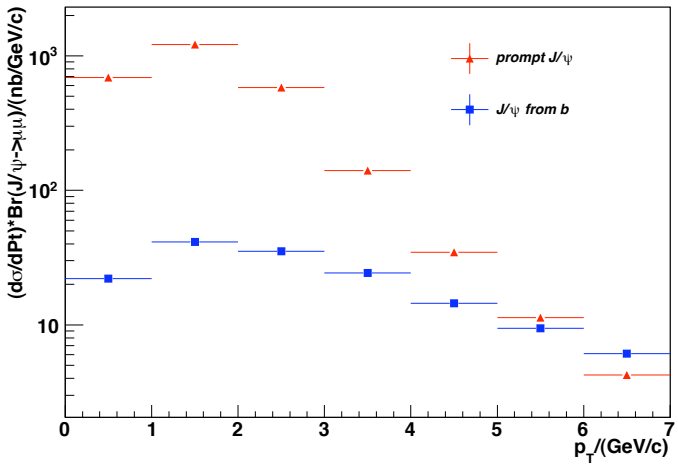

Figure 4.4: The differential cross section as a function of p_T for prompt J/ψ and J/ψ from b. Prompt J/ψ is shown with triangle while J/ψ from b is represented by a square.

of μ^+ (blue dashed line) and μ^- (magenta dash-dot line), since there are no restrictions on the decay products, both of them are flat. The prompt and retarded components are the same in this graph. Later we will see that due to the effect of the magnetic field and of the detector acceptance, the distributions of μ^+ and μ^- become quite different.

The differential distributions for the prompt J/ψ and J/ψ from b with pseudo-rapidity $\eta \in [3, 5]$ and $p_T \in [0, 7]$ GeV/c at generator level are shown in Figure 4.4 [5]. The red triangles represent the distribution for the prompt J/ψ and the blue boxes show the one for the J/ψ from b-hadron decays. In the following analysis, the above region is further divided into 28 sub-regions and the measurement for the cross section and polarization are performed in each of them. We divide the p_T range into 7 bins each of 1 GeV/c width and the η range into 4 bins each of 0.5 width. This reduces greatly possible systematic errors induced by the exact p_T and η shapes. The above analysis region is chosen so that in 5 pb^{-1} data at $\sqrt{s} = 14$ TeV, the statistical errors for the number of prompt J/ψ and J/ψ from b-hadrons in each bin are less than 10%. The analysis can also be performed for other p_T and η regions, such as those with high p_T and lower η which overlap with the CMS and

[5]Note that the LHCb simulation is not perfect in describing J/ψ production both in the shape and total cross sections. It can differ from real data by a factor 10.

ATLAS acceptances.

4.3 J/ψ Selection Criteria

The J/ψ selection is optimized using the DC06 minimum bias event sample passing the L0 trigger. The beam energy used in the Monte Carlo sample is 7 TeV. The version of the reconstruction software Brunel is v31r10. The software used for the whole selection algorithm is DaVinci v22r3.

4.3.1 J/ψ Pre-Selection

Before optimizing the selection criteria, we first need to select most of the J/ψ from the minimum bias event sample and reject the obvious non J/ψ events at the same time. This step is called preselection. We first require that the decay products μ are StdLooseMuons, this is the standard LHCb μ selection criteria (See Chapter 3). The StdLooseMuon requires the reconstructed track to be a long track and to have the "IsMuon" flag. Two μ with opposite charges are then combined to reconstruct J/ψ candidates. The reconstructed J/ψ candidates are required to be within a ± 400 MeV/c^2 mass window around the J/ψ nominal mass [33]. The selected dimuon events are fitted to make a vertex and the quality of the vertex, χ^2/ndof, is required to be less than 10.

After the above preselections, 16,117 J/ψ candidate events are selected from 5,246,747 simulated minimum bias events passing the L0 trigger. With these events, there are 18,895 J/ψ candidates reconstructed, which means that a significant fraction of the J/ψ events have more than one J/ψ reconstructed while at the generator level, only 3 of the reconstructed J/ψ events have more than 2 simulated J/ψ. In fact, most of the above J/ψ candidates (17,432) are background combinations and only 1,463 of them are matched to a true generated J/ψ. Here a reconstructed J/ψ candidate is matched to a true generated J/ψ if both the reconstructed J/ψ candidate and the decay products μ are matched to the true generated ones. For the muon matching algorithm, the particle to Monte Carlo particle associator is "Particle2MCMethod::Chi2" (a LHCb function, defined in [125]) and for J/ψ, the particle to Monte Carlo particle associator is "Particle2MCMethod::Composite". As different matching algorithms may

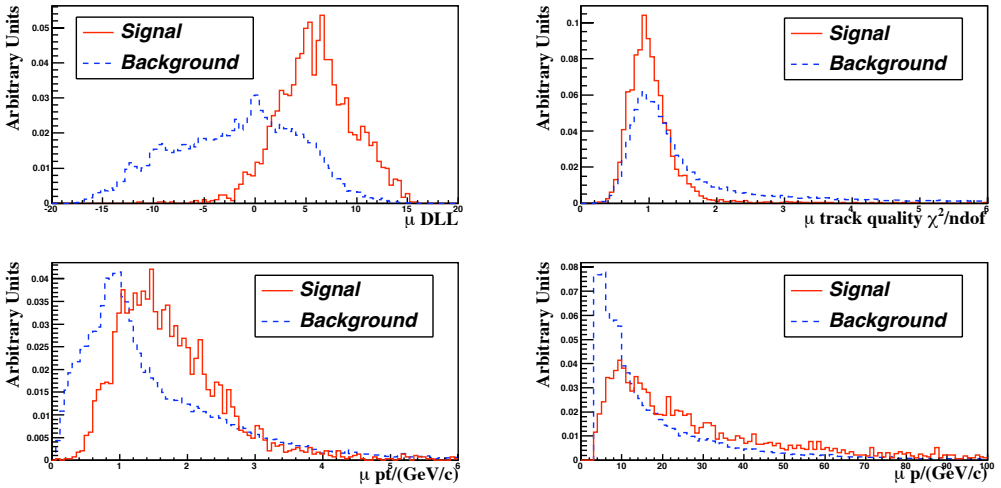

Figure 4.5: Difference between the logarithms of combined likelihoods computed for the muon and pion hypotheses (DLL), track quality (χ^2/ndof), p_T and p distributions of muons of the reconstructed J/ψ from the preselected sample. The distributions with solid line are for the muons from the reconstructed J/ψ matched to Monte Carlo particles (noted as signal) while the distributions with dashed line are muons which are either ghost particles or particles misidentified as muons (noted as background).

show different results, the IBackgroundTool (another matching algorithm tool, see [125]) is also used as a cross check and agrees with the above algorithm within statistical errors. Amongst the remaining 17,432 candidates (18,895 reconstructed candidates − 1,463 true generated J/ψ), only 147 have both muons matched to true muons but coming from other sources than a J/ψ. The other 17,285 candidates have at least one muon not matched to a true muon. These unmatched muons are either ghost particles which do not have any Monte Carlo particles matched to them or other particles misidentified as muons. More precisely, the muon candidates from events with at least one muon not matched to Monte Carlo truth can be ghost tracks (25 %), misidentified pions (53 %) or misidentified kaons (14 %). The misidentification is mainly due to the decays in flight of pions or kaons into muons. As StdLooseMuon only uses μ particle identification information from the Muon detector, it has little discriminating power for the above misidentified pions and kaons. In order to reduce this kind of background, the combined particle identification is needed with further information from the RICH detectors and from the calorimeters.

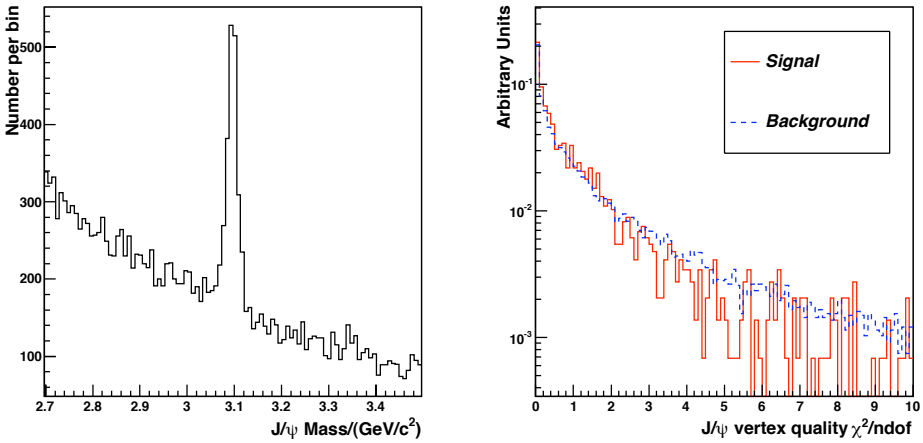

Figure 4.6: Left: mass distribution of the reconstructed J/ψ. Right: vertex quality distribution of the reconstructed J/ψ. The solid line is for the signal events while the dashed line is for the background.

The main background source comes from the combination of fake muons and further cuts are required on the muon selection. Figure 4.5 shows different variables for ghost particles and misidentified muons (noted as background, blue dashed line) compared with muons matched to true generated muons (noted as signal, red solid line), from the preselected sample obtained by applying the very loose selections. Because the main sources of misidentified particles are pions, the difference in the logarithms of the combined likelihoods (combined DLL) chosen in the analysis is $\Delta\ln(L_{\mu\pi})$ which is the difference of the combined DLL computed for the muon and pion hypotheses (see Chapter 3 for details). It shows that the fake muons are mainly low p_T tracks with bad track quality (χ^2/ndof where χ^2 and ndof are the χ^2 and number of degree of freedom from the track fit) and lower combined DLL.

The mass and vertex quality distributions of the reconstructed J/ψ from the preselected sample are shown in Figure 4.6. The vertex quality distributions of the reconstructed J/ψ matched and not matched to Monte Carlo particles show that the vertex quality is not a good variable for J/ψ selection optimization. In the analysis, we require the χ^2/ndof of the J/ψ vertex to be less than 6. In the final selection, p_T, track quality and combined DLL are chosen to optimize the J/ψ selection criteria.

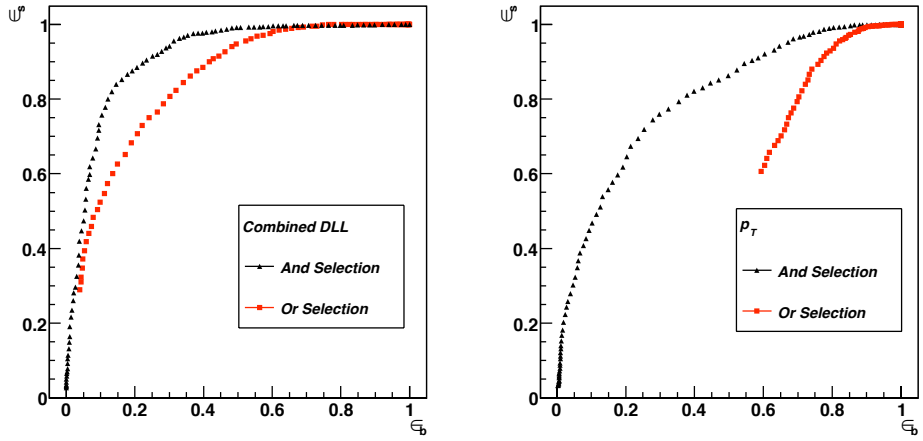

Figure 4.7: Left: efficiency of signal (vertical axis) and background (horizontal axis) after applying different combined DLL requirements on the preselected sample. Right: efficiency changes after applying different requirements for p_T. The triangles show the performance when applying the requirements on both muons and the squares show the performance when applying the requirements on only one of the muons.

4.3.2 J/ψ Selection Optimization

Since we have two muons for the J/ψ reconstruction, there are two possible combinations for the combined DLL and p_T variables. One is to require that both muons pass the criteria and another is to ask that one of the muons passes the criteria. The rejection power is compared for the two methods in Figure 4.7. The results show that selections applied to both muons help to further reduce the background. We will use it in the following analysis [6].

In order to maximize the statistical significance of the signal, the ratio $\frac{S}{\sqrt{S+B}}$ (S is the number of signal events and B is the number of background events) should be maximized. Figure 4.8 shows the $\frac{S}{\sqrt{S+B}}$ values as a function of the selection criteria within J/ψ mass region $[3.067, 3.127]$ GeV/c^2. As we will see later that the mass resolution for the di-muon invariant mass distribution is around 11 MeV/c^2, the above region is chosen to be a $\pm 3\sigma$ window range around the J/ψ nominal mass. From the plots we can see that when track χ^2/ndof ~ 1.7, DLL ~ 0 and p_T ~ 1 GeV/c^2, the ratio

[6] For other studies like particle identification, the second selection method may be used.

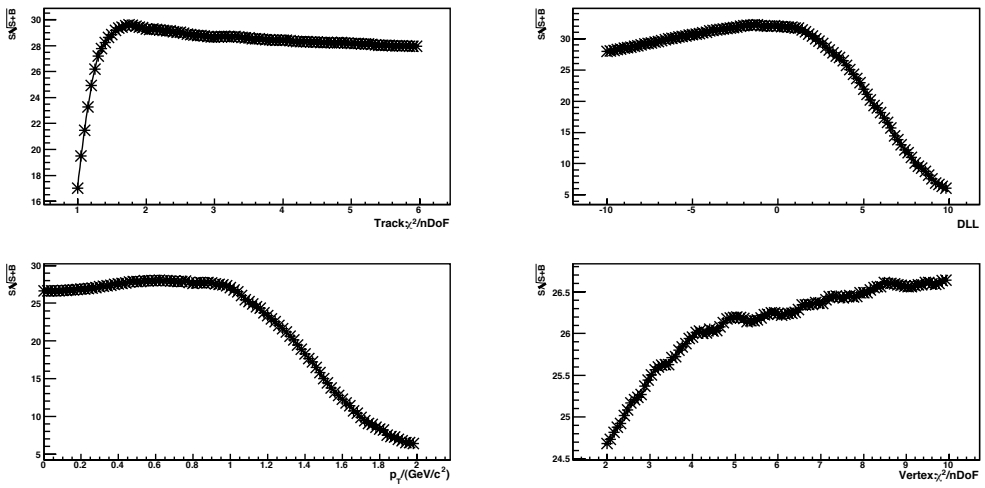

Figure 4.8: The $\frac{S}{\sqrt{S+B}}$ values within J/ψ mass region $[3.067, 3.127]$ GeV$/c^2$ as a function of cut values for: track quality χ^2/ndof, combined DLL, transverse momentum, and J/ψ vertex fit quality χ^2/ndof.

$\frac{S}{\sqrt{S+B}}$ is maximized. The efficiencies with respect to the preselected sample for the three requirements are around $90\%, 90\%, 71\%$ respectively. In order to reduce possible systematic errors due to the low efficiencies of different selection criteria and take into account the difference between simulated data and experiment data, we use a little looser selections as our optimal selection criteria and list them in Table 4.4. An additional requirement on the primary vertex is added because a primary vertex is needed to perform proper lifetime calculation to distinguish prompt J/ψ and J/ψ from b. The position of the primary vertex used later in the analysis is the refitted primary vertex position [7] after removing the muons tracks from the reconstructed J/ψ to reduce the correlation between the reconstructed J/ψ vertex and the primary vertex. After the above selections, we obtain a sample of 1975 events with 2004 J/ψ candidates. There are 27 events with multiple J/ψ reconstructed. The simulation shows that the multiple J/ψ inside 11 (0.5%) of these events are actually matched to the same true generated J/ψ. These events are reconstructed due to the clone effect where the same track is reconstructed more than once. The reconstructed μ tracks matched to the same true generated tracks are named "clone tracks" and the events with J/ψ reconstructed with

[7] The primary vertex is refitted using the rest of the tracks without the μ^+ and μ^- from the J/ψ to obtain the new position and errors instead of a new vertex finding and fitting, thus the number of primary vertices after refitting is the same as the one before refitting.

Table 4.4: $J/\psi \to \mu^+\mu^-$ selection criteria

Quantity	Cut value
μ track:	Long track with muon detector hits (StdLooseMuon)
μ: p_T	$> 0.7\,\mathrm{GeV}/c$
μ: $\Delta\ln(\mathrm{L}_{\mu\pi})$	> -1
μ: track quality χ^2/ndof	< 2
J/ψ: Mass Window	$\pm 0.4\,\mathrm{GeV}/c^2$
J/ψ: Vertex χ^2/ndof	< 6
Event: Number of primary vertices	> 0
Event: Multi-J/ψ	Clone selection criteria (See below)

clone tracks are named "clone events". In order to avoid multiple counting during the calculation, only one of the clone candidates is retained while the others are removed. In this thesis, the following selection is used to kill clone candidates:

$$(\cos\theta_+ > 0.9999) \quad \text{and} \quad (\cos\theta_- > 0.9999), \tag{4.4}$$

where θ_+, θ_- are the angles between the μ^+, μ^+ and μ^-, μ^- from two different reconstructed J/ψ candidates in the same event. If Eq. (4.4) is satisfied, the two J/ψ are considered to be clones to each other and the one with the best track quality (the one with smallest sum of track quality, χ^2/ndof) will be chosen. After the above selection, all the clone J/ψ are removed and there is no reduction on the non-clone J/ψ candidates.

4.4 Expected J/ψ Production

The expected number of J/ψ for a certain amount of data analyzed is obtained by fitting the mass distribution shown in Figure 4.9. As the decay width of the J/ψ is 93.4 ± 2.1 KeV [33] while the approximate mass width in Figure 4.9 is 10 MeV/c^2, the main contribution on the mass distribution comes from the resolution which can be described by a Gaussian function. As 30% of the di-muons come with a radiative photon, a Crystal Ball function [126] is used to fit the signal distribution instead of a Gaussian function and a first order polynomial function is used to fit the background distribu-

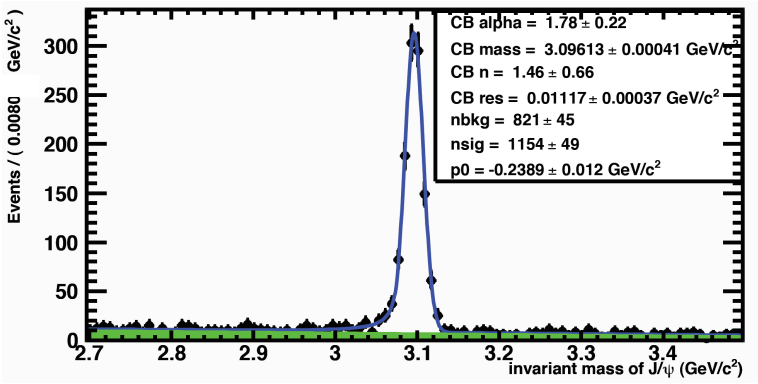

Figure 4.9: The mass distribution of the reconstructed J/ψ after selection. A Crystal Ball function is used for the signal and a linear function for the background (green filled area).

tion. [8] The Crystal Ball function is defined as:

$$f(m,\mu,\sigma,\alpha,n) = \begin{cases} \dfrac{\left(\frac{n}{|\alpha|}\right)^n e^{-\frac{1}{2}\alpha^2}}{\left(\frac{n}{|\alpha|} - |\alpha| - \frac{m-\mu}{\sigma}\right)^n} & \dfrac{m-\mu}{\sigma} < -|\alpha| \\ \exp\left(-\dfrac{1}{2}\left(\dfrac{m-\mu}{\sigma}\right)^2\right) & \dfrac{m-\mu}{\sigma} > -|\alpha|, \end{cases} \tag{4.5}$$

where m is the measured mass, μ is the mean J/ψ mass, σ is the mass resolution, and n, α are the parameters of the Crystal Ball function. Due to the strong correlation between n and α, we use the following procedure in the mass-lifetime combined fit below: we first fit the mass distribution with all the parameters from the Crystal Ball function free [9]. The parameter n is then fixed in the combined mass-lifetime fit. This is done for each p_T and η bin which results in a bin-dependent value of n and α. An extended maximum log-likelihood method is used in the mass fit and there are in total 7 fit parameters including the signal number and background number.

The mass distribution together with its fit function are shown in Fig-

[8] In fact, the Crystal Ball function does not describe the J/ψ mass distribution very well. As the J/ψ sample grows larger, the fit quality becomes worse. Other mass distributions are also tried, but the Crystal Ball function is currently the best one and is used in the following analysis. Because of this non-perfect fit function, a bias may appear and is discussed below.

[9] An unbinned fit is used in the analysis. The mass resolution σ is a fit parameter instead of the values obtained from the measurement.

ure 4.9 where the green filled area shows the background component. The fitted mass is a little smaller than the PDG [33] value due to an incorrect description of the magnetic field [127]. Figure 4.9 also shows that the mass resolution of the reconstructed J/ψ is $11.1 \pm 0.4\,\mathrm{MeV}/c^2$ and the S/B ratio (ratio of signal events over background events) in the $\pm 3\sigma$ mass window is 17.6 ± 2.3. This can be compared to the one before the selection which is 1.03 ± 0.04. The fitted number of J/ψ is $1,154 \pm 49$. It agrees with the number of J/ψ matched to the true generated particles which is 1,167. From the above number, we can obtain that there is one J/ψ reconstructed for every 4,500 minimum bias events passing L0 defined in DC06, corresponding to around 7.3×10^4 minimum bias events before the trigger. It also means there are around 250 reconstructed J/ψ every second after L0. For $1\,\mathrm{pb}^{-1}$ of data at $\sqrt{s} = 14\,\mathrm{TeV}$, we expect approximately 1.3×10^6 reconstructed J/ψ.

A cross check on a minimum bias sample generated at $\sqrt{s} = 10\,\mathrm{TeV}$ (where the J/ψ production cross section is 60 % of that at $\sqrt{s} = 14\,\mathrm{TeV}$) with a more recent software version [10] shows similar results. The MC09 sample used contains 8,901,451 events without L0 trigger requirement. After analysis, around 181 events pass the selection criteria and the fit results show that there are around 124 ± 13 signal J/ψ reconstructed. That is one per every 5×10^4 minimum bias events. The S/B ratio obtained for the MC09 sample is 28.5 ± 14.5 (the large error is due to the lack of statistics, there are only 6 background events in the $\pm 3\ \sigma$ mass window).

4.5 Differential Cross Section Analysis

In this section, the strategy for the differential cross section measurement is given. In order to increase the J/ψ statistics, another sample is used for the following study, where signal events are from an inclusive J/ψ sample, instead of the minimum bias sample. The signal sample is the DC06 inclusive J/ψ sample after stripping with Brunel version v31r11. The J/ψ stripping criteria for DC06 are listed in Table 4.5. The analysis is based on DaVinci v22r3. The number of stripped events used is $1,255,896$ which corresponds to $2,664,809$ events before stripping. This represents $0.79\,\mathrm{pb}^{-1}$ of data at LHCb nominal running conditions ($\sqrt{s} = 14$ TeV). After applying the selection criteria obtained from the study of the minimum bias sample, we

[10] The color octet terms are implemented in this version

Table 4.5: $J/\psi \to \mu^+\mu^-$ selection criteria for DC06 stripping

Quantity	Cut value
μ track:	Long track with muon detector hits (StdLooseMuon)
μ: max p_T	$> 0.5\,\mathrm{GeV}/c$
J/ψ: Mass	$> 2.697\,\mathrm{GeV}/c^2$
J/ψ: Vertex χ^2/ndof	< 15

have in total 998,600 J/ψ events reconstructed (1,000,105 reconstructed J/ψ candidates) with 989, 362 of them matched to Monte Carlo truth (990,009 J/ψ candidates matched). There are 1,495 reconstructed events with 2 J/ψ candidates reconstructed and 5 events with 3 J/ψ candidates reconstructed. Within these multiple J/ψ events, only 16 of them have 2 J/ψ decaying to $\mu^+\mu^-$ at generator level which is around 0.001% of the selected events.

Due to the complexity of the matching procedure, different matching algorithms have different matching efficiencies and misidentification rates. For most of the current matching algorithms used in LHCb, the efficiencies are around 100%. But the loss of signal events due to the matching algorithm should still be considered as it may cause a bias on the efficiency. Figure 4.10 shows the mass distribution of the unmatched J/ψ candidates according to the matching algorithm described above. It shows that there is a mass peak around the J/ψ nominal mass and these J/ψ candidates should be counted as signal J/ψ. The number of these J/ψ events is around 0.1% of the total J/ψ signal events which means the effect caused by the matching algorithm is less than 0.1%.

The $p_T - \eta$ distributions of the signal events are shown in Figure 4.11, for the prompt J/ψ and J/ψ from b where the horizontal axis corresponds to p_T and the vertical axis corresponds to η. The distributions are the ones after selections and L0 trigger.

Since we do not have the corresponding statistics of minimum bias events, the background events are obtained from a toy Monte Carlo which simulates the behavior of minimum bias background events for most of the variables used [11]. The signal sample is then mixed with 7×10^5 toy Monte Carlo back-

[11]Due to the lack of statistics of the minimum bias sample , the p_T and η distributions

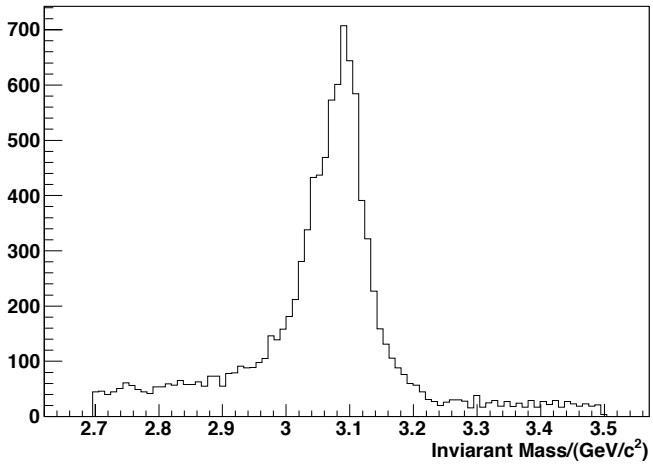

Figure 4.10: Mass distribution for the unmatched J/ψ candidates.

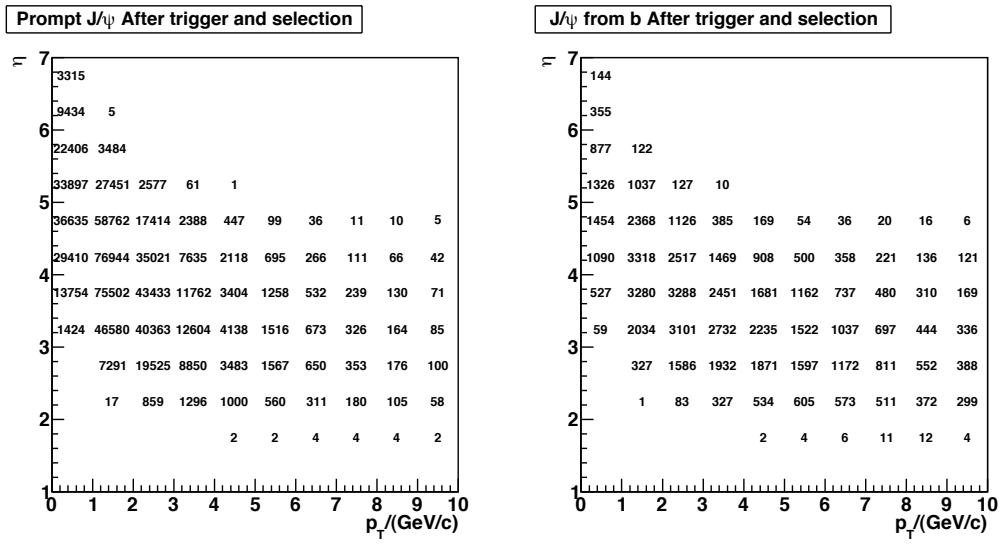

Figure 4.11: The $p_T - \eta$ distribution of the selected prompt J/ψ (left) and J/ψ from b (right). The number of events in each bin corresponds to $0.79\,\mathrm{pb}^{-1}$ of Monte Carlo data with $\sqrt{s} = 14\,\mathrm{TeV}$.

ground events to reproduce the S/B observed in the minimum bias sample.

4.6 Separation of prompt and delayed J/ψ

As has been said in the introduction, there are three main sources of J/ψ. The one from b tends to be far from the primary vertex while the two others (prompt J/ψ) are produced immediately at the primary vertex. In order to extract the prompt J/ψ and J/ψ from b cross sections separately, we need to find a variable to distinguish the two components.

4.6.1 Variable Optimization

In this note, the proper time of J/ψ (referred to the primary vertex) in the z direction (the z axis is along the beam, oriented from the VELO detector to the muon detector) is used since we have larger boost in the z direction than x, y directions. Because the b particles are not fully reconstructed, the J/ψ momentum and mass are used instead of the exact b-hadron momentum. The discriminating variable is defined as

$$t_z(J/\psi) = \frac{d_z \times M_{J/\psi}}{p_z^{J/\psi}}, \tag{4.6}$$

where p_z is the J/ψ momentum in the z direction and $M_{J/\psi}$ is the mass of J/ψ [12], d_z is the signed distance along the z axis between the J/ψ decay vertex and the primary vertex where it comes from. For events with several primary vertices, the one which is closest to the J/ψ vertex in the z direction is selected. Besides the above method, there are other ways to choose the primary vertex like minimum impact-parameter-significance method (The impact-parameter significance is defined as the ratio between impact parameter and its error [13]), but the differences between different methods are

are generated using the distributions of J/ψ signal events from the stripped sample instead of the background events from minimum bias sample.

[12] The chosen mass can either be the measured mass or the nominal mass from PDG. There are little difference between the t_z distribution calculated from the two definitions and in this thesis the nominal mass is chosen.

[13] An alternative definition is also used in LHCb: the impact parameter significance is defined as the χ^2 change when adding the track to the primary vertex fit. The two definitions are similar when the number of tracks in the primary vertex are large.

Table 4.6: Misidentification rates for different primary-vertex choosing algorithm (only for events with more than one primary vertex)

Selection methods	Minimum d_z	Minimum impact-parameter significance
b events	$12.9 \pm 0.2\%$	$5.0 \pm 0.1\%$
Prompt J/ψ events	$0.11 \pm 0.01\%$	$1.08 \pm 0.02\%$

small. The qualities of different methods are evaluated by the misidentification rate which is defined as the probabilities of choosing the wrong primary vertex in multiple primary-vertex events. The results of the two methods are listed in Table 4.6 for the prompt J/ψ events and J/ψ from b events. It shows that the minimum d_z method gives a lower misidentification rate for the prompt J/ψ events while the minimum impact-parameter significance method is more suitable for the J/ψ from b decays. In the current simulation, the events with more than 2 primary vertices are around 29.9% of the reconstructed J/ψ events (4.5% with more than 3 primary vertices) [14]. Thus for the prompt J/ψ, the misidentification rates are less than 1% of the total number of events and the difference between the two methods is around 0.2% which is negligible in our analysis. For these J/ψ from b-decays, the misidentification rate is less than 4% of the b events ($\sim$0.3% of the total events). The wrongly chosen primary vertex usually gives a smaller t_z than the real one since only the primary vertex with the smallest d_z is chosen to calculate t_z. The bias caused by it (less than 1%) is taken into account in the errors caused by the fit function description.

Figure 4.12 shows the generator level distributions for the b lifetime and for the t_z variable. The b-decay lifetime is shown by the black line which as expected should be the same as the one in the z direction. The distribution of t_z is shown by the blue squares and the b decay time in the z direction is shown by the red triangles. The two distributions are similar to each other. The fitted lifetime value for the t_z variable is 1.41 ± 0.03 ps while the fitted value for the average b lifetime is 1.48 ± 0.03 ps. For the prompt J/ψ, the t_z distribution is a peak at zero lifetime. The generator level t_z distribution after selection and trigger criteria shows similar results with a lifetime fit value equal to 1.49 ± 0.01 ps. Thus it is reasonable that an exponential function

[14]The fraction of events with more than one primary vertex depends on the running scenario (luminosity) and here only the DC06 values of the J/ψ sample are given.

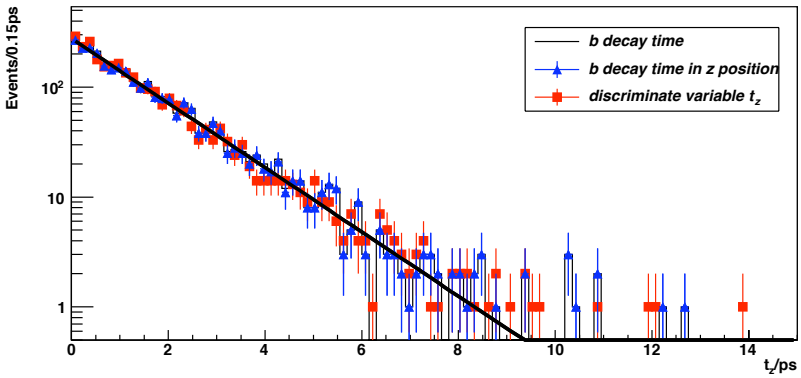

Figure 4.12: Generator level distributions of b lifetime and of t_z. The b decay lifetime is shown by the black line and the b lifetime in z direction is shown by the triangles while the discriminating variable t_z is shown by squares.

is used to describe the b component of the t_z distribution after selection and L0 trigger.

The reconstructed t_z distribution is shown in Figure 4.13. The blue component is the prompt J/ψ distribution and the red dots display the distribution of the J/ψ from b. Besides these two distributions, we also find an additional long tail. This component is indicated in Figure 4.13 by the green color. This tail is due to the association of the J/ψ candidate to a wrong primary vertex. The t_z distributions are a little different in different p_T and η bins due to the difference in the fractions of different components.

Besides the lifetime in the z direction, the one in the x-y plane can also be used as discriminating variable; in fact, the CDF experiment uses this variable. Figure 4.14 shows the distributions with similar definition:

$$t_{xy}(J/\psi) = \frac{d_{xy} \times M_{J/\psi}}{p_{xy}^{J/\psi}}. \tag{4.7}$$

Here the red curve shows the prompt J/ψ distribution and the blue curve gives the results for the J/ψ from b-hadrons. The left graph shows the result in the full p_T region and the right plot shows the distribution for J/ψ with $p_T > 0.75$ GeV/c. From the plots, we can see that in the low transverse momentum region, the t_{xy} distribution has very poor discriminating power for the prompt J/ψ and J/ψ from b decays while this region is very interesting for the LHCb measurement. In the z direction, although there

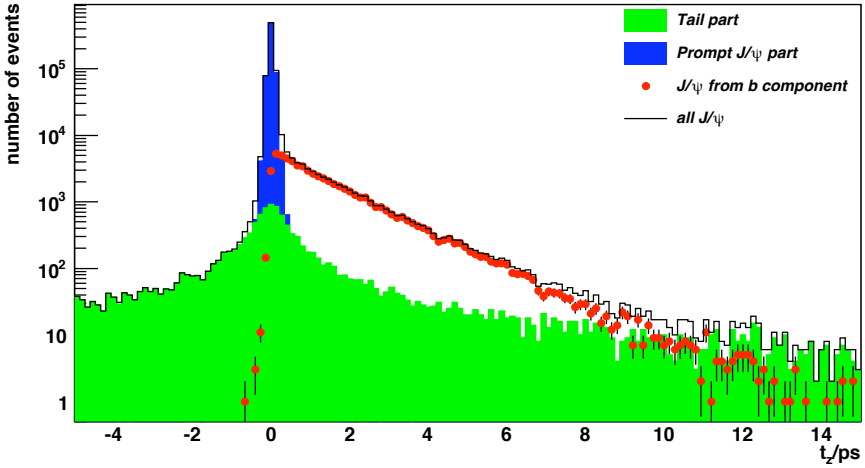

Figure 4.13: t_z distribution for J/ψ matched to Monte Carlo truth. The green component is from J/ψ related to a wrong primary vertex (tail component). The blue component is prompt J/ψ while the red dots show the J/ψ from b component.

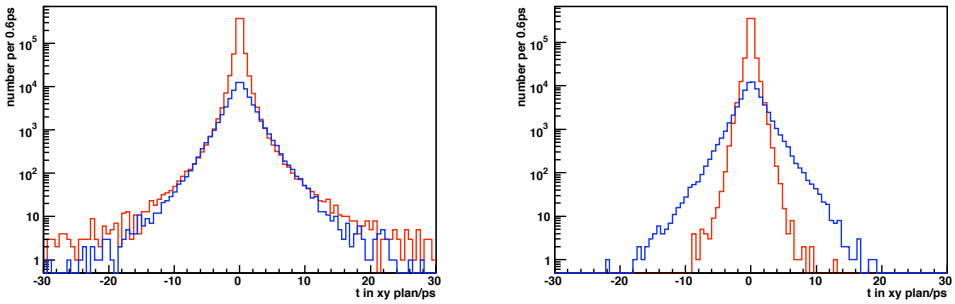

Figure 4.14: Reconstructed t_{xy} distributions for J/ψ matched to Monte Carlo truth (red for prompt J/ψ, blue for J/ψ from b-hadron decays). The left plot shows the result in full p_T region and the right plot shows the distribution for J/ψ with $p_T > 0.75$ GeV/c.

is the tail problem, the fractions in different p_T and η bins are similar and the measurement can still be well performed for the low p_T region. In fact, the LHCb detector is a forward detector and it has better measurement in the z direction while for the detectors like CDF, ATLAS, CMS, *etc* which are central detectors, they offer better measurements in the x-y plane, that is why they choose the time variable defined in the x-y plane and why we choose the one defined in the z direction. The time in 3-D space can also be used as a discriminating variable but since the J/ψ momentum is not exactly the direction of the b-hadron momentum and it does not offer much better discriminating power while requiring more complicated calculations, we use t_z for our final analysis.

4.7 Tail Distribution Estimation

The tail distribution in the above section is mainly due to the association of the J/ψ vertex to a wrong primary vertex. There are two reasons for the wrong association. One comes from the wrong choice of primary vertex amongst several primary vertices. In the above section, we point out that the misidentification rate affects our analysis little and that the t_z due to the wrong rate is smaller than the real t_z, so this is not the reason for the long tail. The main source of wrong association is from events where the primary vertex from which the J/ψ comes is not reconstructed. In this case, the calculated t_z can be larger than the real one. The fraction of the tail events is around 1.5 % of the total number of J/ψ events [15]. Since it is a long lifetime distribution which extends to the b component region and the number of the tail events is 10.2 % of the b component in the region $t_z \in [2, 15]$ ps, a good understanding of the tail distribution is important for the measurement of the J/ψ from b cross section.

According to the primary vertex reconstruction algorithm described in Chapter 3, there are two main reasons why a primary vertex is not reconstructed:

1. There are not enough tracks reconstructed for this primary vertex; the

[15]For the prompt J/ψ events, it is $1.62 \pm 0.02\%$. For b-hadron events, it is $0.37 \pm 0.03\%$. This also means that the fraction of J/ψ from b-hadrons is smaller in the tail events. In our analyzed phase space region, the b fraction in the tail events is around 1.7%

minimal number of tracks required to form a primary vertex in the LHCb software is 6.

2. Two primary vertices are close to each other and only one of them is reconstructed with tracks belonging to the other primary vertex while the second primary vertex is not reconstructed.

In the second case, the positions of the reconstructed and un-reconstructed primary vertices are correlated. This category of events is distributed around $t_z = 0$, with a larger width than the t_z distribution of correctly reconstructed primary vertices. This component of the tail event will be included in the description of the prompt J/ψ t_z distribution.

For the first case, the position of the un-reconstructed primary vertex is independent of the position of the reconstructed primary vertex used to compute t_z. The long tail (events in the tail with $|t_z| > 5\,\text{ps}$) is dominantly composed of events in this category: the correct primary vertex is not reconstructed because not enough tracks coming from it are reconstructed. In order to estimate the shape of the t_z distribution of this category of tail events, we can simulate the position of an un-correlated reconstructed primary vertex using an independent event, for example the next event in the J/ψ sample. Then the t_z distribution of the tail events is estimated from the distribution of

$$\frac{(z_{J/\psi} - z_{\text{PVnext}}) \times M_{J/\psi}}{p_z^{J/\psi}}, \tag{4.8}$$

where $z_{J/\psi}$ is the z position of the J/ψ vertex and z_{PVnext} is the z position of the primary vertex in the "next event". The momentum used is from the current event. During the calculation of the estimated tail distribution, we do not need to distinguish the prompt J/ψ events and J/ψ from b events because the average decay length for the b hadrons is just several millimeters while the distribution of the primary vertex is a Gaussian distribution with $\sigma = 50$ mm which is much larger than the b-decay length. Moreover the b fraction is around 7% of the total number of events and part of them also contribute to the tail distribution. In fact, since the b fraction in the tail events is a little different from that in all events, the p_z distribution may be different between the two and the p_z distribution of the background events may also affect the estimated tail distribution as they are also used when estimating the tail distribution. Figure 4.15 shows the ratios of the p_z distributions between different components (left: tail events, right: background events)

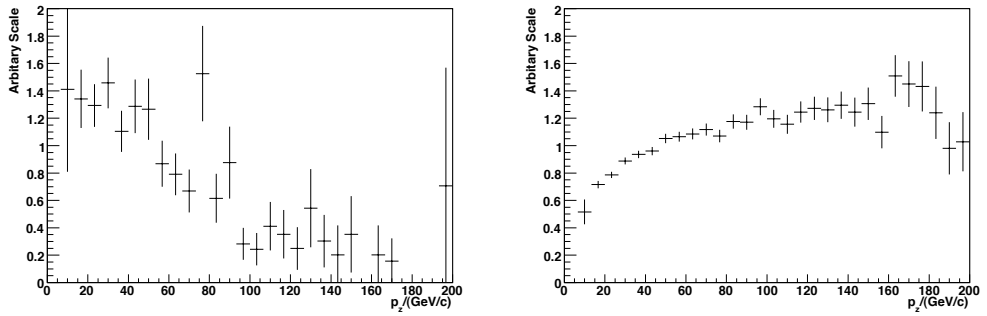

Figure 4.15: The ratios of p_z between different components (left: tail events, right: background events) and signal J/ψ.

and the total J/ψ signal events. It shows that the ratios depend a little on p_z and the bias caused is accounted for in the bias by the fit function.

Using Eq.(4.8), we obtain the estimated tail distribution and show it in Figure 4.16 together with the real distribution. In the graph, the comparisons are given for different p_T regions in order to exclude possible dependence on it. The comparisons show that the two agree very well in the negative t_z region while not so for the positive region. In fact, the real distribution is asymmetric with respect to $t_z = 0$ while the obtained one is symmetric. This is due to the fact that the primary vertex reconstruction efficiency depends on z. There are less VELO stations at small z and the primary vertex reconstruction is slightly less efficient in this region [16].

To take into account this effect, Eq. (4.8) must be modified to incorporate the extra z dependence on the primary vertex reconstruction efficiency. More precisely, each t_z entry as defined in Eq. (4.8) must be assigned a weight, $\omega(z_{J/\psi})$ which depends on $z = z_{J/\psi}$ of the prompt J/ψ (which is equal to the z of the primary vertex from where the J/ψ comes from). This weight is the probability that a primary vertex at $z_{J/\psi}$ is not reconstructed, and satisfies the relationship $\omega(z_{J/\psi}) = 1 - \epsilon(z_{J/\psi})$, where $\epsilon(z)$ is the primary vertex reconstruction efficiency as a function of z.

The weight function $\omega(z_{J/\psi})$ is obtained from data. For a given interval $z_1 < z_{J/\psi} < z_2$, we plot the data t_z distribution (Eq. (4.6)) obtained for J/ψ

[16] In fact, these unreconstructed primary vertices usually have less tracks and as the vertices move to the negative region, less tracks are reconstructed. This affects a lot the reconstruction of primary vertex with less tracks.

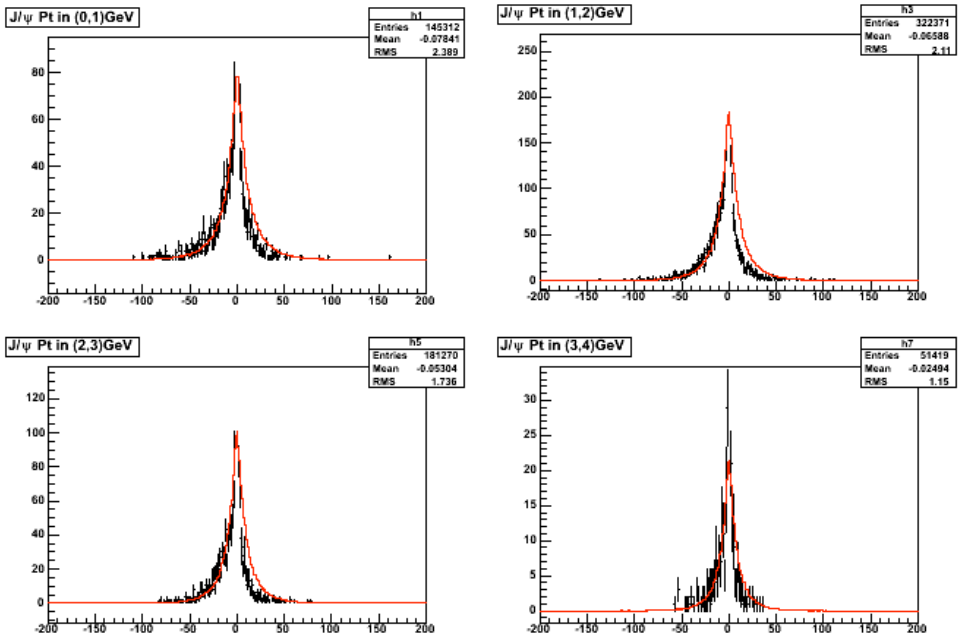

Figure 4.16: Estimated tail distribution (red histogram) obtained with Eq. (4.8) and real distribution (black points) in four different p_T regions.

with $z_1 < z_{J/\psi} < z_2$. Let us consider in this distribution only the region $t_z \in]-\infty, -3\,\text{ps}] \cup [10\,\text{ps}, +\infty[$. As can be seen from Figure 4.13, events in this region are all tail events, for which the primary vertex of the J/ψ is not reconstructed. Let $A(z_1)$ be the number of events in this region.

For the same fixed interval $z_1 < z_{J/\psi} < z_2$, we plot now the distribution of the variable defined in Eq. (4.8), using then the primary vertex of the next event, and again with J/ψ in $z_1 < z_{J/\psi} < z_2$. Let $B(z_1)$ be the number of events in this new distribution which are in the same region than the one defined above: $t_z \in]-\infty, -3\,\text{ps}] \cup [10\,\text{ps}, +\infty[$.

For small enough $z_{J/\psi}$ bins (20 mm bins are used in the analysis), the ratio $\frac{A(z_{J/\psi})}{B(z_{J/\psi})}$ is an estimate of $\omega(z_{J/\psi})$. In fact, in the small $z_{J/\psi}$ range, the distribution obtained from Eq. (4.8) is not affected by the reconstruction efficiency (as a function of $z_{J/\psi}$) and it should be the same as the tail distribution. Figure 4.17 shows the comparison between the two distributions in different $z_{J/\psi}$ regions. On the plots, the black points represent the tail distributions directly obtained from the simulation and the blue curves show the estimated tail distributions. The two agree very well and we can also see

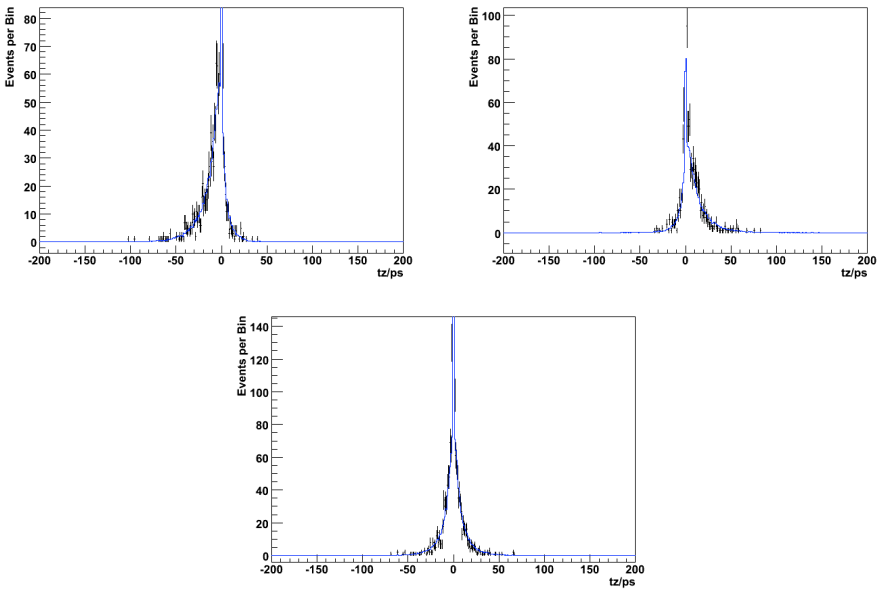

Figure 4.17: Estimated tail distributions (blue histogram) obtained from Eq. (4.8) and real tail distributions (blue points) in different z position of primary vertex. Left: $z_{J/\psi} \in (-45, -35)$ mm; Middle (bottom): $z_{J/\psi} \in (-5, +5)$ mm; Right: $z_{J/\psi} \in (+35, +45)$ mm.

that the distributions in different $z_{J/\psi}$ regions are quite different and different efficiencies as a function of $z_{J/\psi}$ may cause a large difference in the total shape. Since the two distributions are similar to each other, we can derive:

$$\omega(z_{J/\psi}) = \frac{\text{Events with } J/\psi \text{ primary vertex not reconstructed}}{\text{Total reconstructed } J/\psi \text{ events}} = \frac{A(z_{J/\psi})}{B(z_{J/\psi})}. \tag{4.9}$$

Figure 4.18 shows the weight $\omega(z_{J/\psi})$ as a function of $z_{J/\psi}$, estimated by the method described above (magenta points). The two other curves in Figure 4.18 represent the same quantity estimated using Monte Carlo truth information:

- *red points*: a Monte Carlo primary vertex is defined as reconstructed if there are tracks coming from it matched to the reconstructed primary vertex,
- *blue points*: on top of the previous definition, we require that the distance between the Monte Carlo primary vertex and the reconstructed primary vertex is less than 3 mm.

As expected, the second definition is more restrictive than the first one and the real distribution lies between the two curves. In the negative $z_{J/\psi}$ region, primary vertices have worse reconstruction efficiencies and the wrong ratio is around 3%.

The Monte Carlo tail distribution (magenta) of the reconstructed J/ψ and the distribution estimated from the method presented above (green) are shown on Figure 4.19. We observe that the tail distribution is correctly described by the estimated distribution at large t_z. The difference at t_z close to 0 is due to case 2 described above where the two primary vertices are close to each other and the positions of the two primary vertices are correlated with each other. This part will be included in the prompt J/ψ t_z distribution description.

4.8 t_z Distribution Fit Function

Besides the tail distribution, there are two other components for the J/ψ t_z distribution. One is the prompt J/ψ part. Its distribution reflects the

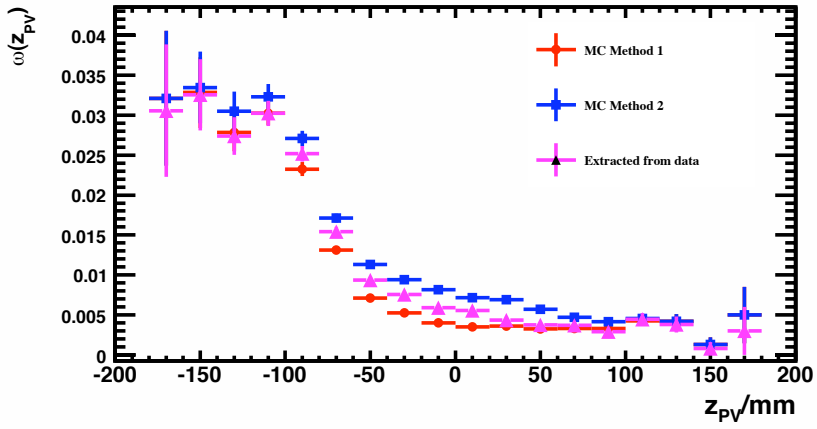

Figure 4.18: The magenta line shows the probability for a primary vertex to be not reconstructed, obtained by our method. The other two distributions are from different Monte Carlo definition of a reconstructed primary vertex. The red distribution shows the probability for a primary vertex to be not reconstructed when a Monte Carlo primary vertex is called not reconstructed if none of its tracks is matched to the tracks in the reconstructed primary vertices. The blue distribution shows the same quantity with requesting in addition that the distance between the reconstructed primary vertex and the Monte Carlo primary vertex is less than 3 mm.

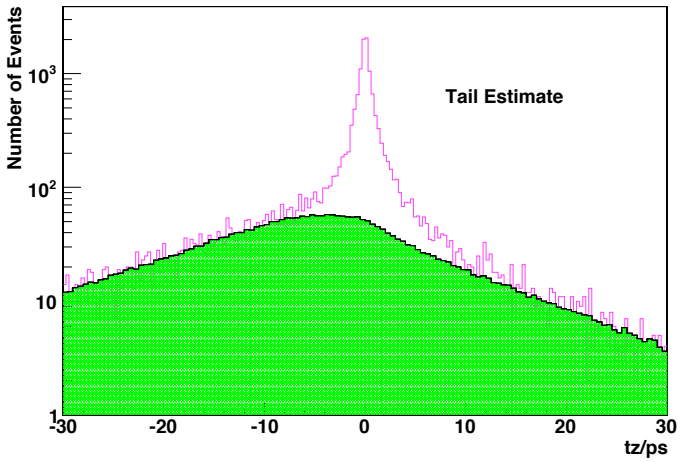

Figure 4.19: The magenta histogram shows the tail distribution from Monte Carlo and the green histogram shows the tail distribution estimated with the method described in this section.

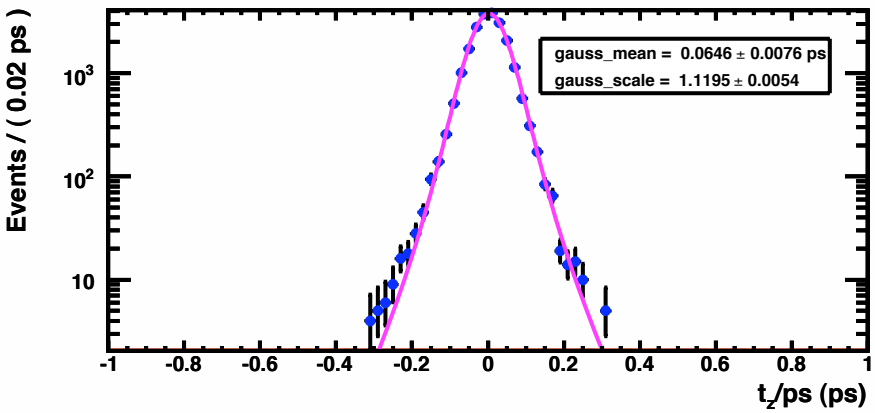

Figure 4.20: The prompt J/ψ distribution not including the tail distribution. The fit result using one Gaussian function are superimposed.

resolution of the t_z variable. We use a Gaussian distribution to parameterize it:

$$\text{Resolution}(t_z|t_{\text{err}}) = \frac{1}{\sqrt{2\pi}\sigma} e^{(-\frac{(t_z - t_{\text{mean}})^2}{2\sigma^2})} \qquad \sigma = s \times t_{\text{err}}, \tag{4.10}$$

where t_{mean} is the average value of the prompt t_z distribution, s is the ratio between the true t_z resolution and the measured resolution. If the primary vertex and the J/ψ vertex are well reconstructed, the above two parameters should be 0 and 1 respectively. Eq. (4.10) is the conditional probability function under t_{err} where t_{err} is the measured error of t_z (the main contributions of t_{err} come from the errors of the J/ψ momentum and of the z coordinate of the J/ψ vertex). The total distribution is the integral over the t_{err} distribution $\rho(t_{\text{err}})$:

$$\text{Resolution}(t_z) = \int \text{Resolution}(t_z|t_{\text{err}})\rho_p(t_{\text{err}})\mathrm{d}t_{\text{err}}, \tag{4.11}$$

here $\rho_p(t_{\text{err}})$ is the t_{err} distribution of the prompt J/ψ. As an example Figure 4.20 shows the fit results for the true prompt J/ψ events not including the tail distribution in the range $p_T \in [3, 4]$, $\eta \in [3, 4]$ [17] with Eq. (4.11). The fit results of the mean and scale are $t_{mean} = 0.0646 \pm 0.0076$ ps and $s = 1.1729 \pm 0.0067$ respectively. This means that the calculated t_z is slightly biased to the positive t_z and that the errors are underestimated.

In the above discussion, we mentioned that the tail distribution due to the second case of the un-reconstructed primary vertex is included in the

[17] The η range is chosen to be [3, 4] to increase the statistics.

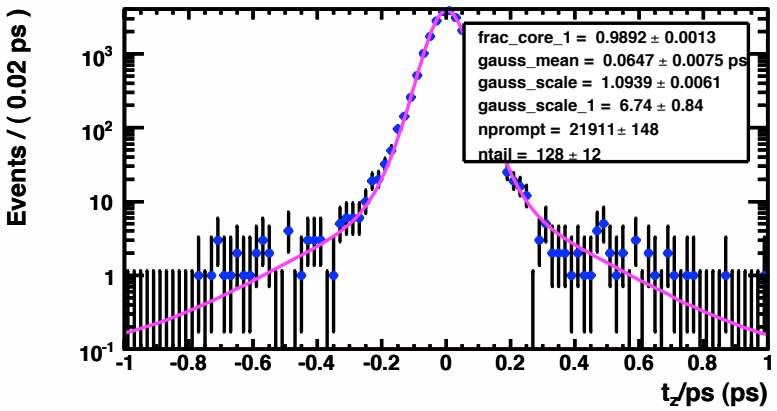

Figure 4.21: The prompt J/ψ distribution including the tail distribution. The fit result using double Gaussian and the estimated tail distribution are superimposed.

prompt J/ψ fit and they contribute to the distribution with larger errors and one Gaussian function may probably not describe the t_z distribution very well. Figure 4.21 shows the fit results in the region $p_T \in [3,4]$, $\eta \in [3,4]$ for the prompt J/ψ and tail distributions with the sum of the two Gaussian functions and the estimated tail distribution. It shows that the fraction of the second Gaussian is only $(1.08 \pm 0.13)\%$ (other bins have similar results). The correlations between the parameters of the two Gaussian functions and the fraction between them are large (around 64%). In the final fit function, we only use one Gaussian for the prompt J/ψ fit function. The difference between the real distribution and the fit function will be included in the systematic bias [18].

The second part of the t_z distribution is the displaced J/ψ which shows the average b lifetime distribution and we choose an exponential distribution convoluted with a resolution function to parameterize it [19]. The function for

[18]The difference between the fit results of one Gaussian and two Gaussian could also be used as estimate of the systematic error, but since we will include all the errors introduced by the fit function model by comparing the difference between the fitted numbers and Monte-Carlo input numbers, this method of systematic error estimation is not used here to avoid double counting.

[19]This choice is valid since we have checked that after the selection and L0 trigger, the Monte Carlo distribution for the t_z of b component can still be well described by an exponential function.

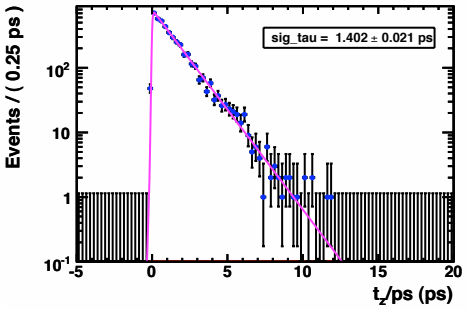

Figure 4.22: t_z distribution of J/ψ from b-hadron and fit results with one exponential function.

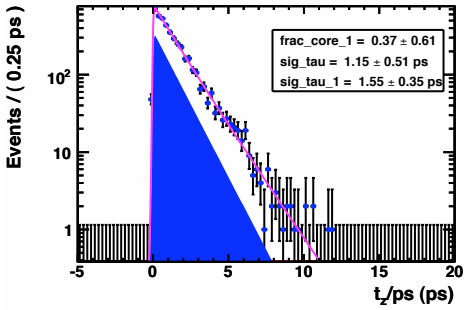

Figure 4.23: t_z distribution of J/ψ from b-hadron and fit results with two exponential functions.

fitting the b part is

$$F_b(t_z|t_{\rm err}) = e^{-t_z/\tau} \otimes \text{Resolution}(t_z|t_{\rm err}). \tag{4.12}$$

The resolution function is the same as the one used for prompt J/ψ. τ is the "average b lifetime" after selection and trigger. Similar to the prompt J/ψ term, the integration of Eq. (4.12) over the $t_{\rm err}$ distribution $\rho_b(t_{\rm err})$ (b component) is used for the total b distribution fit. Figure 4.22 shows the fit results where the resolution function comes from the prompt J/ψ fit. As different b-hadrons have different lifetimes (see Table 4.7), the single exponential function in Eq. (4.12) only describes the average behavior of the distribution. Moreover, during the calculation of t_z, the mass and momentum of J/ψ in z direction are used instead of the mass and momentum of the b-hadron in z direction:

$$t(H_b) = \frac{d_z \times M_{H_b}}{p_{z,H_b}}. \tag{4.13}$$

t_z is an approximation of $t(H_b)$. All these effects make the fit function not perfect for the J/ψ from b-hadron t_z distribution description. Since the single exponential function is only an approximation of the J/ψ from b-hadron t_z distribution, the sum of two exponential functions is also tried as shown in Figure 4.23. The fit results show that the fraction of one exponential is around $37 \pm 61\%$ (the filled area with color blue) and the correlations between the three parameters (the two lifetimes and the fraction between the two exponential functions) are more than 99%. Thus in the final fit, only one exponential function is used for the J/ψ from b-hadrons.

Table 4.7: Lifetime of the different b hadrons and their mixtures [33]

.

b hadrons	Lifetime (ps)
B^+	1.638 ± 0.011
B^0	1.530 ± 0.009
B_s^0	1.417 ± 0.042 (flavor specific)
B_s^0	$1.437\ ^{+0.031}_{-0.030}$ $(1/\Gamma_s)$
B_c^+	0.463 ± 0.071
Λ_b	$1.383\ ^{+0.049}_{-0.048}$
Ξ_b admixture	$1.42\ ^{+0.28}_{-0.24}$
$b-$baryon admixture	$1.319\ ^{+0.39}_{-0.38}$
b-hadron admixture	1.568 ± 0.009

In total, the fit function for the J/ψ signal events is written as

$$F_{J/\psi}(t_z|t_{\rm err}) = \left(n_p\delta(t_z) + n_b e^{-t_z/\tau}\right) \otimes \frac{1}{\sqrt{2\pi}\sigma} e^{(-\frac{(t_z-t_{\rm mean})^2}{2\sigma^2})} + n_{\rm tail}F_{\rm tail}(t_z|t_{\rm err}), \tag{4.14}$$

where n_p, n_b and $n_{\rm tail}$ are the numbers of prompt J/ψ, J/ψ from b-hadrons and tail events respectively, and $\sigma = s \times t_{\rm err}$. $F_{\rm tail}(t_z|t_{\rm err}) = F_{\rm tail}(t_z)$ is the tail distribution described in the above section, assumed to be independent of $t_{\rm err}$. Fig 4.24 shows the $t_{\rm err}$ distributions for all J/ψ signal events (blue triangles), prompt J/ψ events ($\rho_p(t_{\rm err})$), J/ψ from b events ($\rho_b(t_{\rm err})$), tail events ($\rho_{\rm tail}(t_{\rm err})$), and background events ($\rho_{\rm bkg}(t_{\rm err})$). The different components are indicated by red rectangles. We can see that there are differences between the different components while when dealing with the fit function, they are assumed to be the same:

$$\rho_p(t_{\rm err}) = \rho_b(t_{\rm err}) = \rho_{\rm tail}(t_{\rm err}) = \rho_{\rm bkg}(t_{\rm err}) = \rho(t_{\rm err}). \tag{4.15}$$

The bias caused by this assumption will also be included in the bias introduced by the total fit function.

Figure 4.25 shows the t_z distribution for J/ψ signal events in $p_T \in [3,4]\,{\rm GeV}/c$, $\eta \in [3,4]$ and the fit results according to Eq. (4.14), where the blue points represent Monte Carlo data and the green part shows the prompt J/ψ distribution, the yellow part shows the distribution of J/ψ from b-hadrons, the red histogram shows the tail distribution, and the pink part shows the total fit function. We can see that due to ignoring the contributions from the tail events caused by the second case where the primary vertex

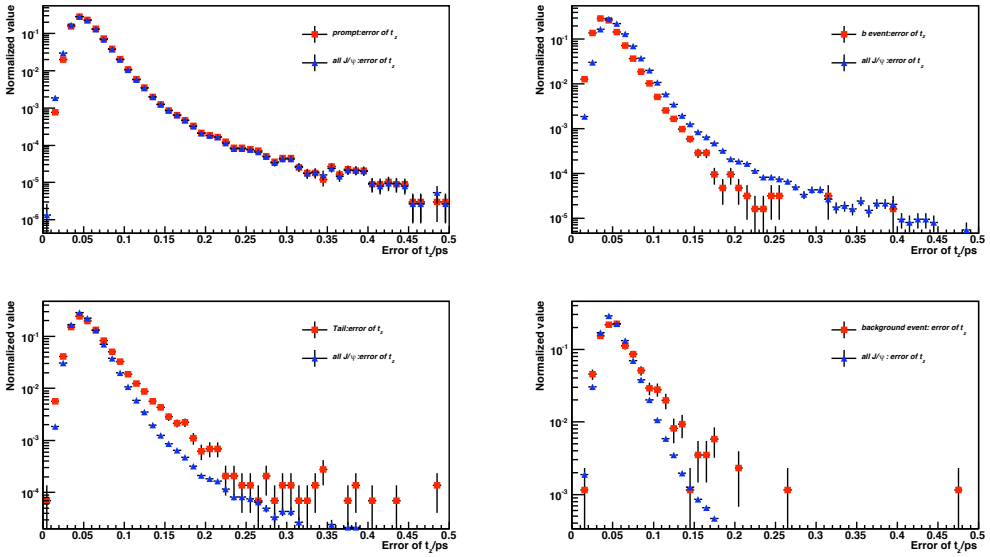

Figure 4.24: The comparison of the $t_{\rm err}$ distributions between the prompt J/ψ (top left), J/ψ from b-hadrons (top right), tail events (bottom left), background events (bottom right) and all J/ψ signal events.

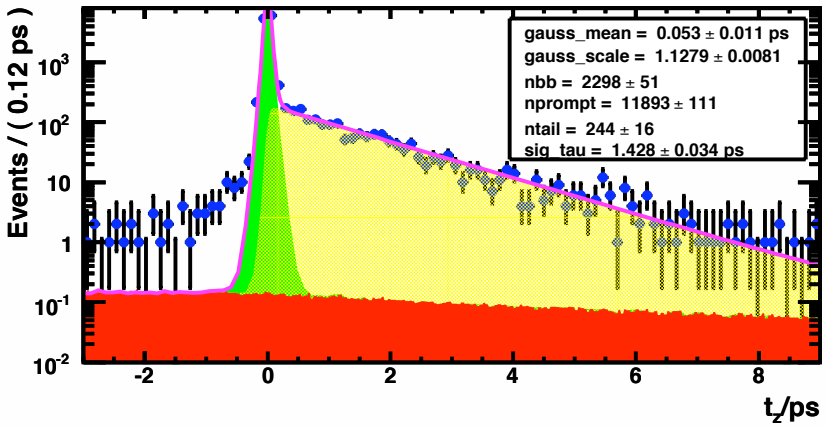

Figure 4.25: t_z distribution of J/ψ signal events in $p_T \in [3,4]\,\mathrm{GeV}/c$, $\eta \in [3,4]$ and their fit results

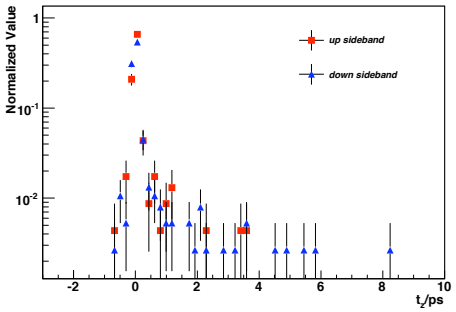

Figure 4.26: t_z distributions for the background events in different mass regions.

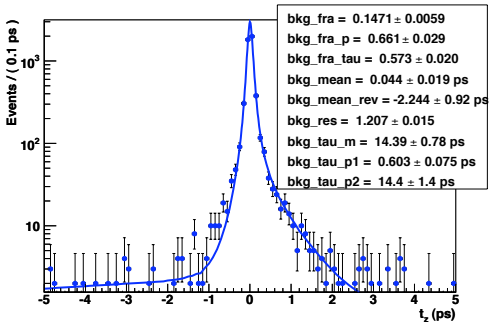

Figure 4.27: Background t_z distribution from the minimum bias sample and fit results.

is not reconstructed, Eq. (4.14) does not describe very well the distribution in the region [-2, -0.5] ps. But the fraction of these events are very small and can be neglected during our analysis.

For the background component, we can obtain the distribution from real data using the J/ψ mass upper sideband [20]. Since we use the distributions from the background events in the upper sideband to estimate the background distribution under the J/ψ mass peak, we must make sure that the two have the same distributions. Figure 4.26 shows the comparison of the t_z distributions in different mass regions where the red rectangles represent the distribution in the mass region [3.2, 3.5] GeV/c^2 and the blue triangles represent the distribution in the mass region [2.7,3.0] GeV/c^2 [21]. The two are identical and it is reasonable to use the t_z distribution in the upper mass region to estimate the distribution in the central mass region. The comparison is done for the minimum bias Monte Carlo sample. The same check should also be done for the real data analysis. Due to limited statistics of fully simulated background events, the background t_z distribution used in the analysis is a toy Monte Carlo distribution generated with the parameters from the fit of the t_z distribution of the background events seen in the minimum bias

[20] From Figure 4.2, we can see that there are still some J/ψ signal events in the lower sideband because of the radiative J/ψ decays, so we do not use this region to obtain the background t_z shape.

[21] Here, the comparison is done for the upper and lower mass regions instead of the marginal and central regions due to the lack of background events, but the similar graphs in the two regions already show that the physics does not change for the background events in these regions.

sample and is considered to be independent from other variables. The t_z distribution of the background events from minimum bias sample is shown in Figure 4.27. Since the background distribution in the real data is different from the one in the Monte Carlo simulation, we do not list the background fit function in this thesis. But we can still see that the background events have exponential components which may affect a lot the measurement of the J/ψ from b hadrons and this may reduce our precision on the cross section measurement if the background level is high.

After considering the background contribution, the total fit function for t_z is

$$F(t_z) = \int (n_{\rm bkg} \times F_{\rm bkg}(t_z|t_{\rm err}) + F_{J/\psi}(t_z|t_{\rm err}))\rho(t_{\rm err}){\rm d}t_{\rm err}, \qquad (4.16)$$

where $n_{\rm bkg}$ is the number of background events, $F_{\rm bkg}(t_z|t_{\rm err})$ is the t_z distribution obtained from the upper mass sideband (conditional probability). The $t_{\rm err}$ distribution of the background events is assumed to be the same as the one for J/ψ signal events, as expressed in Eq. (4.15). In the real data analysis, this assumption can be tested directly by comparing the $t_{\rm err}$ distribution from the upper sideband and $t_{\rm err}$ of the signal events by subtracting the background contribution.

In the above fit function, there are two measured variables: t_z and $t_{\rm err}$, 7 fit parameters: the number of prompt J/ψ (n_p), the number of J/ψ from b-hadron (n_b), the number of background events ($n_{\rm bkg}$), the number of tail events ($n_{\rm tail}$), the average lifetime of b-hadrons (τ), the average value of the prompt J/ψ t_z distribution ($t_{\rm mean}$) and the ratio between the actual and measured error (s). When calculating the final number of prompt J/ψ and J/ψ from b-hadrons, the b fraction in the tail events is considered to be the same as the one in the total J/ψ signal events. The comparison of the two fractions is shown in Figure 4.28 where the horizontal axis represents different p_T and η bins [22]. The errors of the b fractions are calculated at 95% confidence level. The b fractions of the tail events and of the signal events are represented by red triangles and blue rectangles respectively. We can see that the two agree and the difference between them will be included in the systematic errors. As the fraction of the tail events is around 1%, the systematic error caused is less than 1%.

[22] If there is no tail event in certain bins, the b fractions in the tail events are assumed to be 0.

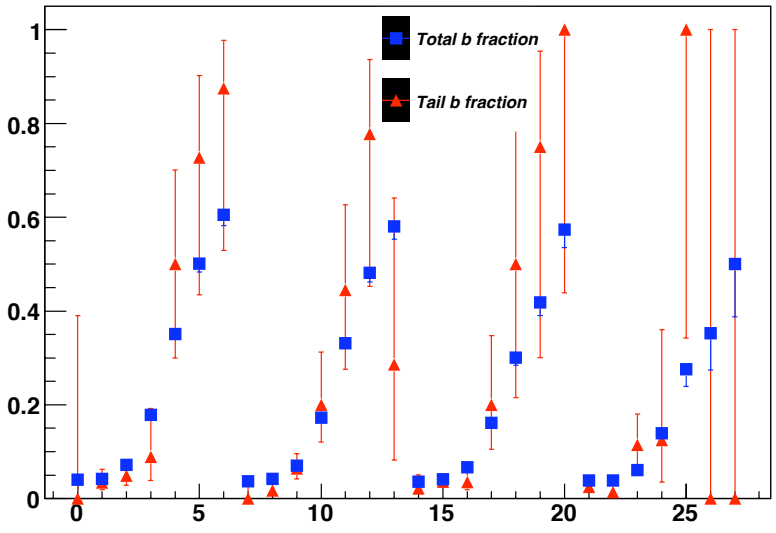

Figure 4.28: The comparison of the b-hadron fractions in the tail events (red triangle) and in the J/ψ signal events (blue rectangle). If there is no tail event, the b-hadron fraction is assumed to be 0.

Since the mass distribution offers further information for signal and background discrimination, we use a combined log-likelihood fit of the mass and t_z distributions to obtain the parameters. The two components are assumed to be independent (the correlation factors between mass and t_z are -0.07 and 0.02 for the background events and signal events). The final fit function is

$$F_{\text{combined}}(t_z, m) = \int (n_{\text{bkg}} \times F_{\text{bkg}}(t_z|t_{\text{err}}) M_{\text{bkg}}(m) + F_{J/\psi}(t_z|t_{\text{err}}) M_{\text{sig}}(m)) \rho(t_{\text{err}}) \mathrm{d}t_{\text{err}}. \tag{4.17}$$

After considering the parameters from the mass function, there are three measured parameters (mass, t_z, t_{err}) and 11 fit parameters (four extra parameters from the mass fit where the parameter n of the Crystal Ball function is fixed and a linear function is assumed for the background mass distribution). An extended unbinned likelihood fit is applied using RooFit [128].

Table 4.8: Number of fitted prompt J/ψ after selection and L0 trigger. The numbers of events in the table correspond to $0.79\,\mathrm{pb}^{-1}$ of Monte Carlo data with beam energy of 7 TeV.

$p_T\,(\mathrm{GeV}/c)$	$\eta \in [3-3.5]$	$\eta \in [3.5-4]$	$\eta \in [4-4.5]$	$\eta \in [4.5-5]$
$0-1$	1334 ± 41	13287 ± 125	28470 ± 183	35541 ± 205
$1-2$	45448 ± 233	73478 ± 284	74884 ± 295	56593 ± 251
$2-3$	38857 ± 217	42627 ± 225	33917 ± 198	16872 ± 137
$3-4$	12541 ± 127	11454 ± 118	7657 ± 97	2290 ± 52
$4-5$	4021 ± 72	3327 ± 66	2059 ± 49	416 ± 29
$5-6$	1575 ± 46	1262 ± 39	682 ± 29	143 ± 21
$6-7$	678 ± 31	517 ± 25	253 ± 20	31 ± 9

Table 4.9: Number of fitted J/ψ from b after selection and L0 trigger. The numbers of events in the table corresponds to $0.79\,\mathrm{pb}^{-1}$ Monte Carlo data with beam energy of 7 TeV.

$p_T\,(\mathrm{GeV}/c)$	$\eta \in [3-3.5]$	$\eta \in [3.5-4]$	$\eta \in [4-4.5]$	$\eta \in [4.5-5]$
$0-1$	80 ± 12	590 ± 30	1211 ± 43	1622 ± 49
$1-2$	2190 ± 57	3759 ± 72	3612 ± 72	2523 ± 59
$2-3$	3242 ± 67	3436 ± 68	2581 ± 59	1152 ± 39
$3-4$	2735 ± 59	2402 ± 54	1429 ± 43	367 ± 22
$4-5$	2219 ± 51	1648 ± 44	856 ± 32	177 ± 16
$5-6$	1540 ± 42	1158 ± 36	494 ± 24	63 ± 10
$6-7$	1017 ± 34	700 ± 28	346 ± 20	40 ± 7

4.9 Fit results

Using the fit function defined above, the fitted numbers of prompt J/ψ and J/ψ from b are summarized in Tables 4.8 and 4.9 in each of the bins of the analysis. The results show that with five times more data ($5\,\mathrm{pb}^{-1}$), the statistical errors for all the bins are less than 10 %. The fitted number of prompt J/ψ is a little smaller than the Monte Carlo input value (less than 2%). This is because the Crystal Ball function used for the mass distribution fit does not totally describe the signal shape, in particular the radiative tail. The bias from the fit is considered as systematic error.

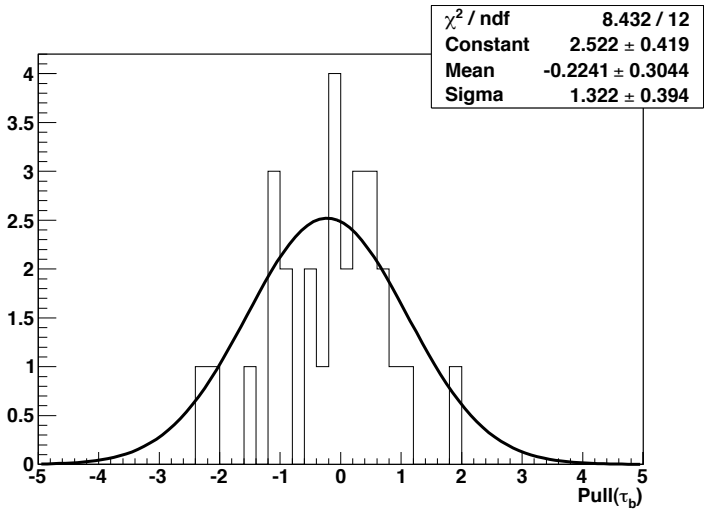

Figure 4.29: Pull distribution of the average b lifetime obtained from the individual t_z fits in the different p_T and η bins of the analysis.

The average fitted lifetime for all the bins is 1.366 ± 0.008 ps where the average lifetime is defined as

$$\tau_{\text{average}} = \frac{\sum_i \tau_i/\sigma_i^2}{\sum_i 1/\sigma_i^2}, \tag{4.18}$$

here τ_i and σ_i is the measured lifetime and its error in the i-th bin. The pull values of the lifetime for each bin are shown in Figure 4.29. Here, the pull is defined as

$$\text{pull}_{\text{i}} = \frac{\tau_{\text{i}} - \tau_{\text{average}}}{\sigma_{\text{i}}}. \tag{4.19}$$

The fit values of the pull distribution indicate that it is a reasonable hypothesis to assume that in each bin we have the same lifetime, but this hypothesis is not required in the fit.

Once we have obtained the number of J/ψ from the fit, we use the efficiency computed in the following section to correct and obtain the original number of J/ψ. The cross section is then calculated using Eq. (4.1). The efficiency in Eq. (4.1) is defined as

$$\epsilon_{\text{x}} = \epsilon_{\text{gen}} \times \epsilon_{\text{rec}} \times \epsilon_{\text{trigger}}, \tag{4.20}$$

where ϵ_{gen} is the acceptance efficiency, ϵ_{rec} is the reconstruction efficiency and $\epsilon_{trigger}$ is the trigger efficiency. We discuss them in detail in the next section.

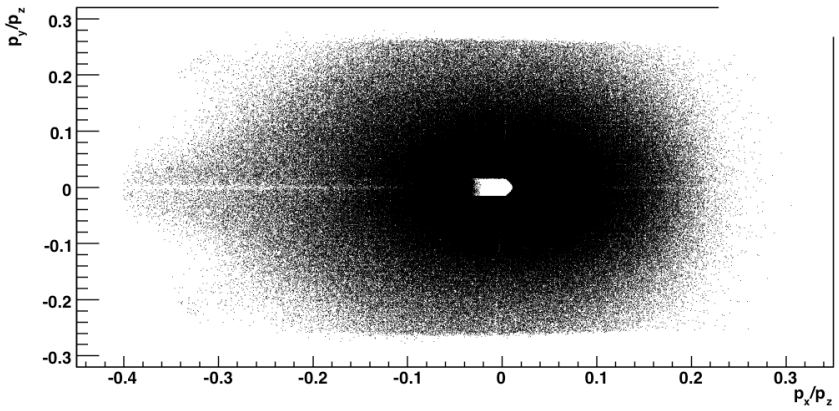

Figure 4.30: The distribution of μ^- from the reconstructed J/ψ in the detector. Here the horizontal is p_x/p_z and vertical axis is p_y/p_z.

4.10 Acceptance and efficiency

There are three main factors entering the total efficiency computed for the selected J/ψ. The first one is the generator level efficiency describing the acceptance effect indicated as ϵ_{gen}. The acceptance efficiency is estimated with a fully simulated Monte Carlo sample generated with J/ψ momentum direction in $[0, 400]$ mrad and it is defined as

$$\epsilon_{\text{gen}} = \frac{J/\psi \text{ with both } \mu \text{ in LHCb in each } p_T \text{ and } \eta \text{ bin}}{J/\psi \text{ generated in each } p_T \text{ and } \eta \text{ bin}}, \tag{4.21}$$

here both μ in LHCb means that the momentum direction of each μ is in $[10, 400]$ mrad. This is a little larger than the LHCb detector acceptance to avoid the loss of events due to the magnetic field as shown in Figure 4.30. It shows the μ^- distribution in the detector where the horizontal axis is p_x/p_z and the vertical axis is p_y/p_z, we can see that due to the magnetic field effect, the μ^- particles outside the acceptance region can still be detected (negative p_x part) and part of the μ^- particles in the detector region can not be detected (positive p_x region). Though the required μ acceptance is larger than the detector acceptance, there are still some μ which can be reconstructed but are not considered in the simulation. The amount of these μ is less than 1% and this is included in the systematic errors.

The acceptance efficiencies for J/ψ in different p_T and η bins are shown in Figure 4.31. The errors of the efficiencies are less than 0.01 in bins with

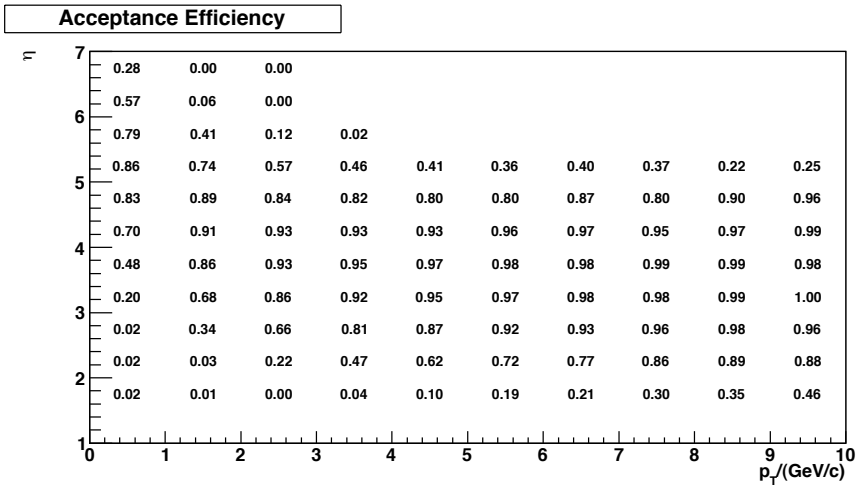

Figure 4.31: The acceptance efficiency for reconstructed J/ψ. The error in each bin is less than 0.01 for $p_T < 7\,\mathrm{GeV}/c$.

p_T less than $7\,\mathrm{GeV}/c$. We take the same acceptance efficiency for prompt J/ψ and J/ψ from b. The effect of polarization is discussed separately. In order to confirm that the two distributions are the same, Figure 4.32 shows the comparison of the acceptance efficiencies in $\eta \in [3, 3.5]$ for the prompt J/ψ (red triangle) and J/ψ from b-hadrons (blue rectangle) respectively [23]. The two agree very well.

The second factor of the efficiency is the reconstruction and selection efficiency for J/ψ which is indicated as ϵ_{rec} (and abbreviated later as reconstruction efficiency). It is defined as

$$\epsilon_{\mathrm{rec}} = \frac{J/\psi \text{ reconstructed and selected in each } p_T \text{ and } \eta \text{ bin}}{J/\psi \text{ with both } \mu \text{ in LHCb in each } p_T \text{ and } \eta \text{ bin}}. \qquad (4.22)$$

The reconstruction efficiency is shown in Figure 4.33 for all reconstructed J/ψ and we also assume that we have the same efficiency for prompt J/ψ and J/ψ from b in each p_T and η bin. The reconstruction efficiency includes all the effects of reconstructing and selecting a J/ψ [24]. The reconstruction efficiency also includes the Monte Carlo matching efficiency ($\sim 100\%$). The error in each bin is less than 0.03 in the region $p_T \in [0, 7]\,\mathrm{GeV}/c$ and $\eta \in [3, 5]$. The reconstruction efficiency for the prompt J/ψ and J/ψ from b-hadrons

[23] Other η regions shows similar results.

[24] In LHCb experiment, the reconstruction efficiency is further divided into reconstructible efficiency, reconstructed efficiency, selection efficiency, *etc*, in this thesis, only the total reconstruction efficiency is discussed.

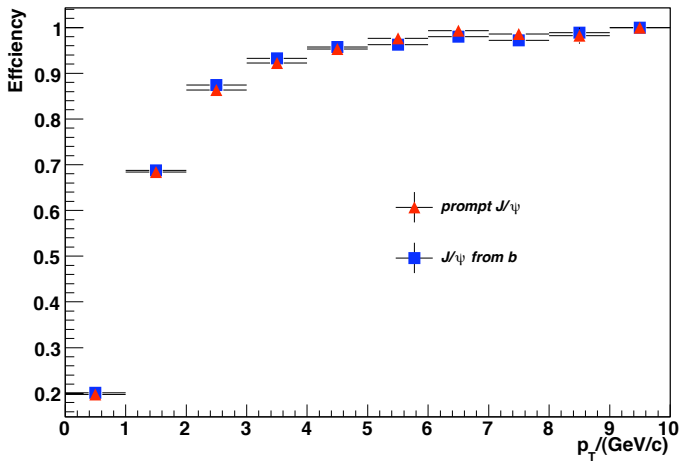

Figure 4.32: Comparison of the acceptance efficiencies in $\eta \in [3, 3.5]$ between the prompt J/ψ (red triangle) and J/ψ from b hadrons (blue rectangle).

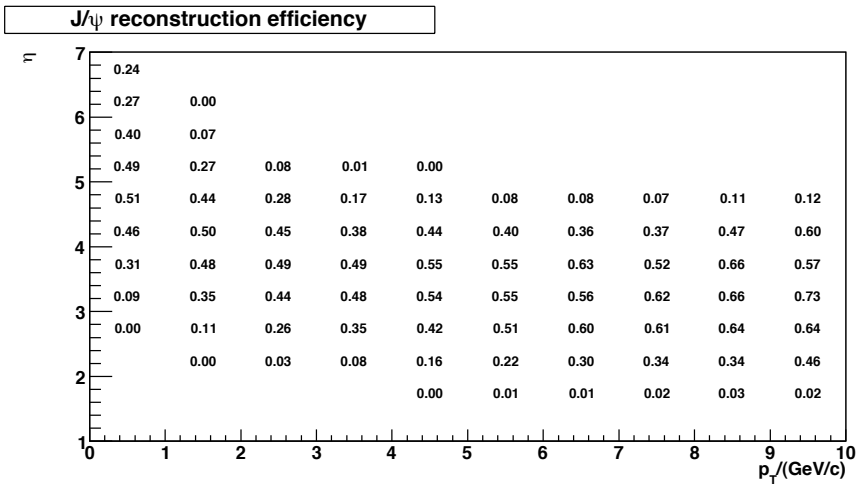

Figure 4.33: The reconstruction efficiency for J/ψ. The error in each bin is less than 0.03 in the region $p_T \in [0, 7]\,\mathrm{GeV}/c$ and $\eta \in [3, 5]$.

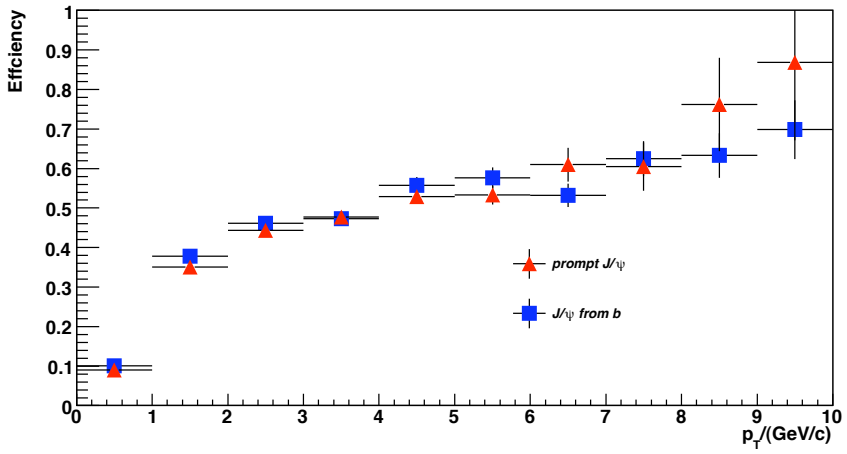

Figure 4.34: Comparison of the reconstruction efficiencies in $\eta \in [3, 3.5]$ for the prompt J/ψ (red triangle) and J/ψ from b-hadrons (blue rectangle).

are also considered to be the same and this is confirmed in Figure 4.34.

The third factor of the efficiency is the L0 trigger efficiency which is indicated as $\epsilon_{\text{trigger}}$ (the HLT trigger is not considered in this thesis). It is defined as

$$\epsilon_{\text{trigger}} = \frac{J/\psi \text{ reconstructed and passing L0 in each } p_T \text{ and } \eta \text{ bin}}{J/\psi \text{ reconstructed in each } p_T \text{ and } \eta \text{ bin}}. \quad (4.23)$$

Figure 4.35 shows the L0 trigger efficiencies for the prompt J/ψ and J/ψ from b-hadron in different p_T and η regions. The error in each bin in the region $p_T \in [0, 7]\,\text{GeV}/c$ and $\eta \in [3, 5]$ is less than 0.01. The L0 efficiency for b-hadron events is larger than the efficiency for prompt J/ψ as the events with b hadrons usually have particles with high transverse momentum and this increases the efficiency to trigger the b-hadron events. In order to understand better the L0 trigger, Figure 4.36 shows the efficiencies of different L0 sub-triggers for the prompt J/ψ and J/ψ from b-hadrons in $\eta \in [3,\ 3.5]$. The first graph is the comparison of the whole L0 trigger efficiency. The last graph shows the efficiencies of non-μ trigger in the L0 trigger; as expected, this trigger efficiency is larger for the b events than the prompt events. The other two graphs are L0Muon trigger and L0DiMuon trigger efficiencies. The efficiency of the prompt J/ψ and J/ψ from b-hadrons are similar for L0Muon but not for L0DiMuon due to the co-produced particles.

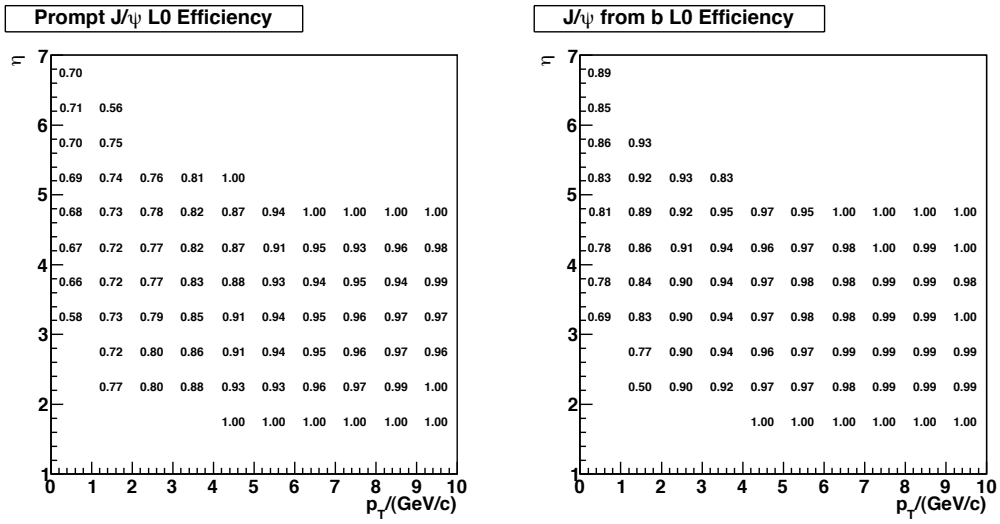

Figure 4.35: The L0 trigger efficiency for the reconstructed prompt J/ψ (left) and J/ψ from b hadrons (right). The error in each bin is around 0.01 in the region $p_T \in [0, 7]\,\mathrm{GeV}/c$ and $\eta \in [3, 5]$.

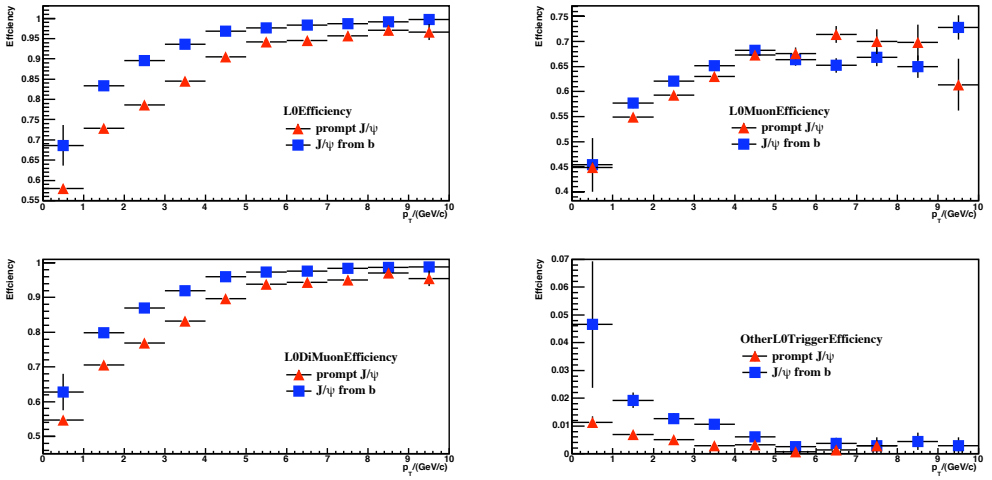

Figure 4.36: The comparison of different L0 triggers for the prompt J/ψ (red triangle) and J/ψ from b-hadrons (blue rectangle) in $\eta \in [3, 3.5]$.

Table 4.10: Total efficiencies (%) of prompt J/ψ.

p_T (GeV/c)	$\eta \in [3-3.5]$	$\eta \in [3.5-4]$	$\eta \in [4-4.5]$	$\eta \in [4.5-5]$
$0-1$	1.0 ± 0.1	9.8 ± 0.3	21.4 ± 0.4	28.4 ± 0.4
$1-2$	17.5 ± 0.2	30.0 ± 0.3	32.9 ± 0.3	28.1 ± 0.3
$2-3$	30.2 ± 0.3	35.2 ± 0.4	32.0 ± 0.4	18.4 ± 0.3
$3-4$	37.3 ± 0.6	39.3 ± 0.6	29.3 ± 0.5	11.3 ± 0.3
$4-5$	46.5 ± 1.1	46.5 ± 1.2	35.5 ± 1.1	9.0 ± 0.5
$5-6$	50.5 ± 1.7	50.1 ± 1.9	35.1 ± 1.7	6.0 ± 0.6
$6-7$	52.0 ± 2.3	58.0 ± 3.1	33.6 ± 2.1	6.9 ± 0.9

Table 4.11: Total efficiencies (%) of J/ψ from b.

p_T (GeV/c)	$\eta \in [3-3.5]$	$\eta \in [3.5-4]$	$\eta \in [4-4.5]$	$\eta \in [4.5-5]$
$0-1$	1.2 ± 0.1	11.5 ± 0.3	25.1 ± 0.4	34.0 ± 0.5
$1-2$	20.0 ± 0.2	35.0 ± 0.3	39.6 ± 0.3	34.3 ± 0.3
$2-3$	34.4 ± 0.3	41.4 ± 0.4	38.1 ± 0.4	21.7 ± 0.3
$3-4$	41.2 ± 0.6	44.5 ± 0.6	33.7 ± 0.5	13.0 ± 0.3
$4-5$	49.6 ± 1.1	51.0 ± 1.2	38.8 ± 1.1	10.0 ± 0.5
$5-6$	52.4 ± 1.7	53.0 ± 1.9	37.6 ± 1.7	6.0 ± 0.6
$6-7$	54.0 ± 2.3	60.4 ± 3.1	34.5 ± 2.1	6.9 ± 0.9

The total efficiency is the product of the three efficiencies. The values for the total efficiencies in the different bins are listed in Tables 4.10 and 4.11.

For the measurement with data collected during the first year, Monte Carlo samples are tuned to reproduce the detector occupancies, hits efficiencies and resolutions observed on data and then used to estimate the reconstruction efficiency.

4.11 Polarization effect on the efficiency

The above efficiencies are obtained from a Monte Carlo simulation where the J/ψ is produced without polarization. Studies show that different polarization schemes give different efficiencies. In this thesis, the variation of efficiency is only studied in the helicity frame without considering any az-

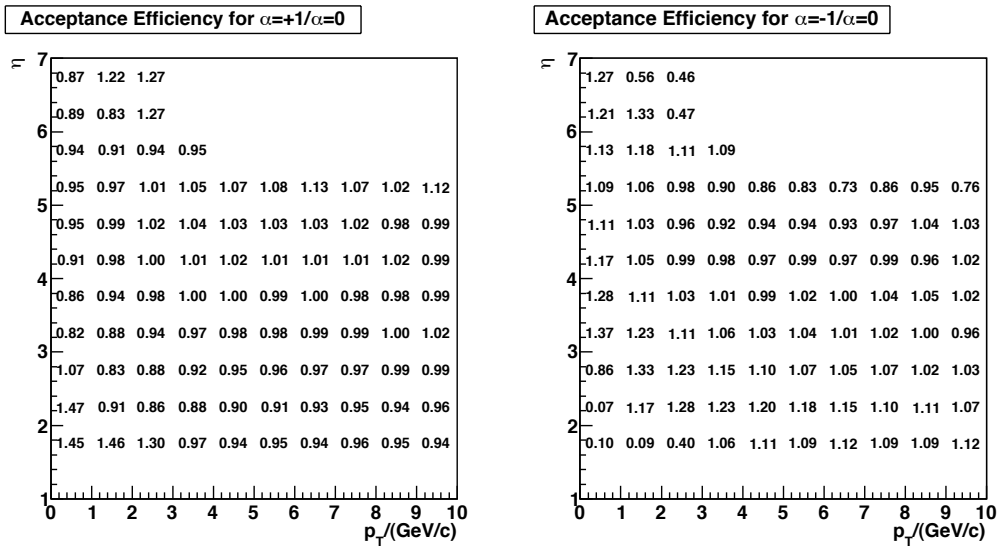

Figure 4.37: Polarization effect on acceptance efficiencies. The left graph shows the acceptance efficiency ratio between the transverse polarization and no polarization. The right graph shows the acceptance efficiency ratio between the longitudinal polarization and no polarization. The errors in bins with $p_T < 5\,\mathrm{GeV}/c$ are approximately 0.01.

imuthal dependence. The angular distribution of a polarized J/ψ ignoring the azimuthal part is described in Chapter 2 as:

$$\frac{1}{N}\frac{\mathrm{d}N}{\mathrm{d}\cos\theta} = \frac{1+\alpha\,\cos^2\theta}{2+2\times\alpha/3}. \tag{4.24}$$

Figures 4.37 and 4.38 show the acceptance and reconstruction efficiencies of different polarization scenarios. The efficiencies are obtained by weighting the unpolarized sample. The plots show that polarization affects a lot the acceptance and reconstruction efficiencies and that the effects depend greatly on p_T and η. For some of the bins, the difference is too large and it imposes to measure the polarization before extracting the cross section. For the bins in the region $p_T \in [0,7]\,\mathrm{GeV}/c$ and $\eta \in [3,5]$, the difference is not too large and we can possibly measure the cross section there before knowing the exact polarization.

Figure 4.39 shows the polarization dependence for different L0 triggers where the top plots are for the prompt J/ψ events and the bottom graphs are for the J/ψ from b decays and only the efficiencies of $\eta \in [3, 3.5]$ are given.

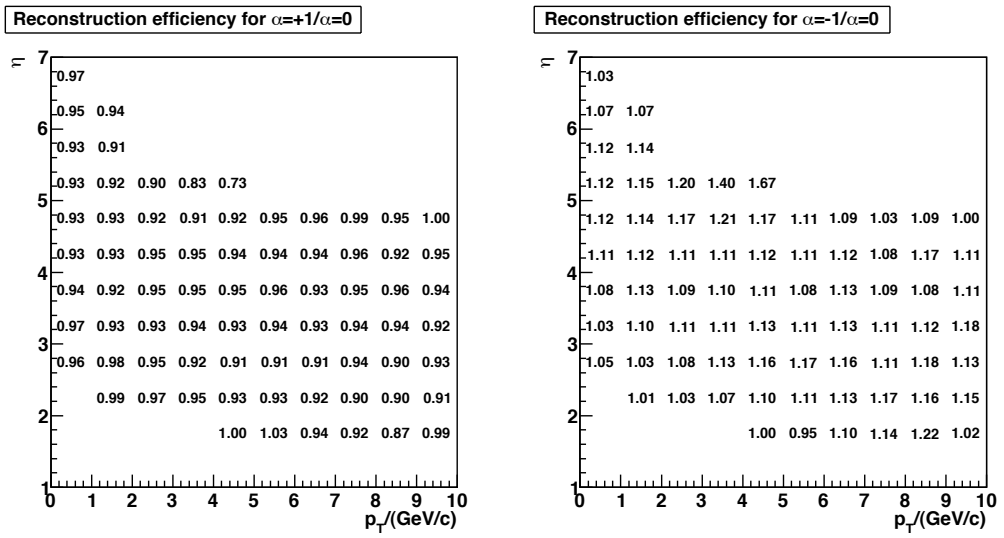

Figure 4.38: Polarization effect on reconstruction efficiency. The left graph shows the acceptance efficiency ratio between the transverse polarization and no polarization. The right graph shows the acceptance efficiency ratio between the longitudinal polarization and no polarization. The errors in bins with $p_T < 5\,\mathrm{GeV}/c$ are approximately 0.01.

From the left to the right, the triggers used are L0 trigger, L0Mfguon trigger and L0DiMuon trigger. The blue boxes show the efficiencies for the non-polarization case, the red triangles show the distributions of the transversely polarized J/ψ and the magenta reversed triangles show the distribution of the longitudinal polarized J/ψ. It shows that polarization affects little the L0 trigger efficiency and it will not be considered in this thesis.

4.12 Luminosity measurement

In LHCb, there are mainly two ways to measure the luminosity: direct methods [129] and indirect methods [130, 131]. The direct methods are based on measurements of the beam shape, their relative position and the angles between two beams, and then calculate the luminosity using

$$L = \sum_{\text{bunches}} f N_1 N_2 2c \cos^2(\phi/2) \int \rho_1(\vec{x}, t)\rho_2(\vec{x}, t)\mathrm{d}^3x\mathrm{d}t, \tag{4.25}$$

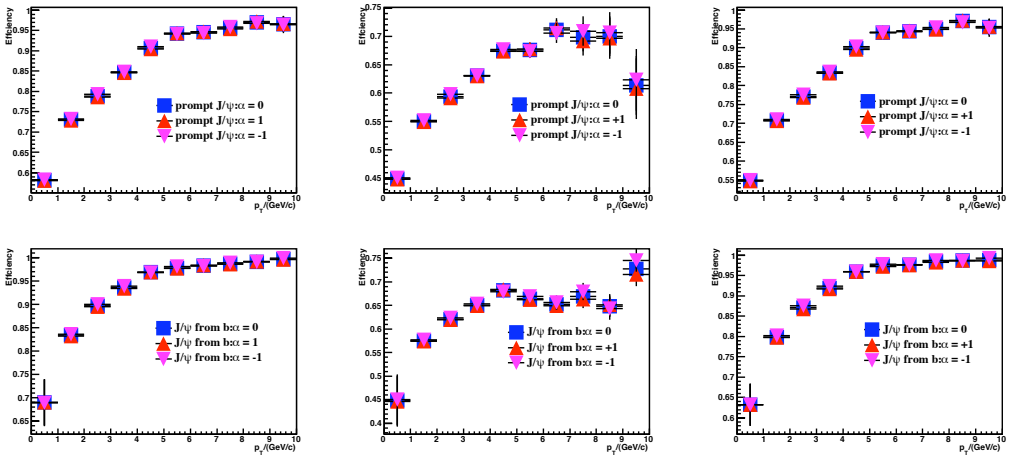

Figure 4.39: L0 trigger efficiency dependence on J/ψ polarization. The top plots are for the prompt J/ψ events and the bottom plots are for the J/ψ from b decays. The trigger used are L0 trigger (left), L0Muon trigger (middle) and L0DiMuon trigger (right). The blue boxes show the efficiencies for the non-polarization case, the red triangles show the distributions of the transversely polarized J/ψ and the magenta reversed triangles show the distributions of the longitudinally polarized J/ψ.

here f is the revolution frequency, N_1 is the number of particles in bunch 1, N_2 is the number of particles in bunch 2, c is the velocity of light, ϕ is the angle between the two beams, $\rho(\vec{x}, t)$ is the normalized distribution of the particle density in a bunch, the integration between the two gives the effective collision area of the two bunches. The main idea for the direct measurement is to measure the particle density function and the distribution is normally assumed to be a Gaussian function. One of the direct method is called Van der Meer scan: the luminosity variations are measured when changing the relative positions of the two beams. From the measurements of the trigger rates in different positions, we can obtain the information on the beam density function. The error of this method is around 10%. In LHCb, another method is also used: the information of the beams can be obtained by reconstructing the beam-gas interaction vertices using the VELO, the error of this method can reach $\sim$5% [129].

The indirect methods measure the cross section using Eq. (4.1). After obtaining the number of events for a decay channel with a well known production cross section, the luminosity during this time can be calculated. The

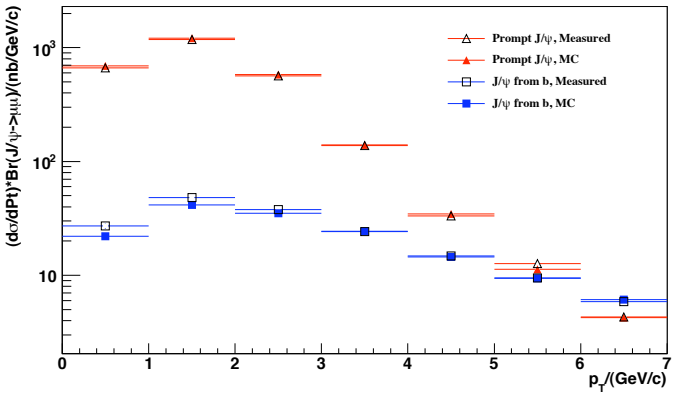

Figure 4.40: The p_T distribution of prompt J/ψ and J/ψ from b. The errors in the plot are from the efficiency and fit errors. The solid symbols are the simulated numbers and the hollow symbols are the fitted values.

LHCb experiment will use $\gamma\gamma \to \mu^+\mu^-$ or W/Z boson production to measure the luminosity indirectly and the errors of the indirect methods with 1 fb^{-1} can be less than 1% [130, 131].

During the time of our measurement, LHCb is at the beginning of physics running and because of the lack of statistics and understanding of the detector, the luminosity measurement during this time is only known to around 10%.

4.13 Results and error discussion

With the efficiency obtained above, we finally compute the differential cross section which is shown in Figure 4.40. The solid symbols are the simulated numbers and the hollow symbols are the fitted values. The errors shown on Figure 4.40 are only statistical errors on the number of events and on the efficiency due to the limited Monte Carlo statistics, added in quadrature. The total cross sections of prompt J/ψ and J/ψ from b, in the LHCb acceptance

are:

$$\sigma\,(\text{prompt } J/\psi,\, p_T(J/\psi) < 7\,\text{GeV}/c,\, 3 < \eta(J/\psi) < 5) \;=\; 43.79 \pm 0.15 \pm 0.44\,\mu\text{b}, \tag{4.26}$$

$$\sigma\,(J/\psi \text{ from } b,\, p_T(J/\psi) < 7\,\text{GeV}/c,\, 3 < \eta(J/\psi) < 5) \;=\; 2.715 \pm 0.067 \pm 0.027\,\mu\text{b}, \tag{4.27}$$

where the second error terms come from the $J/\psi \to \mu^+\mu^-$ branching ratio. The above results agree with the input value listed in Table 4.3 where it gives the above cross sections to be 44.5 ± 0.01 and 2.57 ± 0.01 μb respectively.

Considering the branching ratio of $b \to J/\psi X$, the production of b hadrons with its decay product J/ψ in $p_T(J/\psi) < 7\,\text{GeV}/c$, $3 < \eta(J/\psi) < 5$ is

$$\sigma\,(b \text{ hadrons},\, p_T(J/\psi) < 7\,\text{GeV}/c,\, 3 < \eta(J/\psi) < 5) \;=\; 234.1 \pm 5.8 \pm 2.3 \pm 20.2\,\mu\text{b}, \tag{4.28}$$

where the third error term comes from the $b \to J/\psi X$ branching ratio ($(1.16 \pm 0.10)\%$).

We discuss possible systematic errors due to the polarization identified in Sec. 4.11, and to the fit functions.

Since the polarization of both prompt J/ψ and J/ψ from b are unknown, the measurement is done assuming the sample to be non-polarized. The differences between the results obtained with a polarized Monte Carlo sample and with a non-polarized Monte Carlo sample are assigned as systematic errors. The analysis performed on the polarized sample is the same than the one presented in the thesis for the un-polarized sample, the polarized sample being obtained by weighting the non-polarized one and the efficiency used being the one obtained from the sample without polarization. The relative differences on the un-polarized scenario are shown in Figure 4.41.

The differences are shown for all J/ψ without separating the prompt J/ψ and J/ψ from b: since polarization does not affect the L0 efficiency which is the only efficiency that is different between prompt J/ψ and J/ψ from b, prompt J/ψ and J/ψ from b are affected by the same amount when changing the initial polarization to the same polarization scenario.

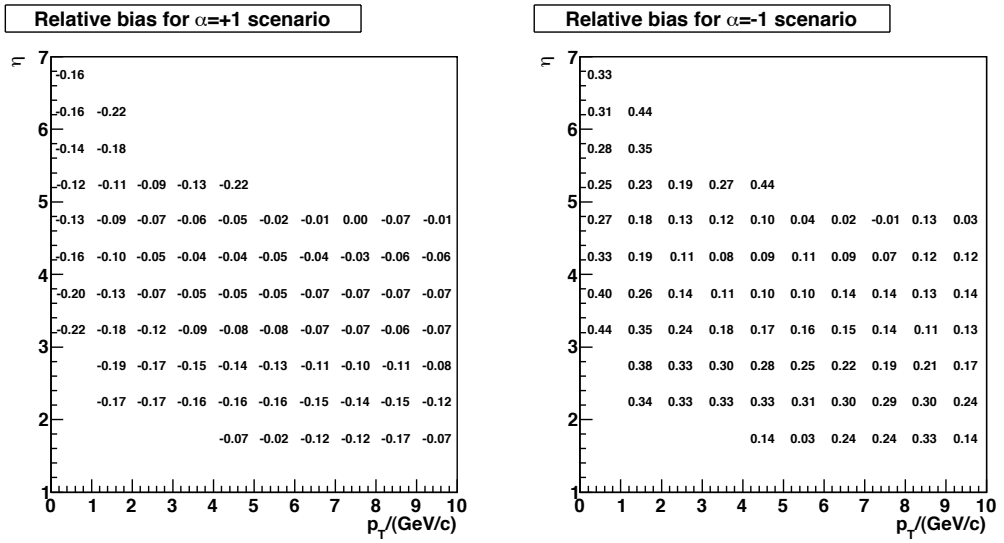

Figure 4.41: Relative bias on the un-polarized scenario due to different polarization scenarios. The left plot shows the bias if the actual polarization is $\alpha = +1$ and the right plot shows the bias if the actual scenario is $\alpha = -1$.

Besides the bias from the polarization, the bias due to the fit function is another source of systematic uncertainty. In order to take into account incorrect description of the J/ψ mass and t_z distributions by our fitting functions, the fitted numbers are compared with Monte Carlo input values and the differences are treated as systematic errors. The result shows that we underestimate by around 2 % the prompt J/ψ number while the number of J/ψ events from b decays is correctly estimated [25]. This error can be reduced with better understanding of the J/ψ mass shape.

There is also a systematic error from the truth matching algorithm because the reconstruction efficiency is calculated using the matched J/ψ. The inefficiency of the matching algorithm may lead to underestimate the efficiencies. The uncertainty from this effect is less than 1 %. The systematic error due to J/ψ signal events outside the $\pm 400\,\mathrm{MeV}/c^2$ mass window is 2 %. These events are from $J/\psi \to \mu^+\mu^-$ decays where photons are radiated from the μ. In the Monte Carlo simulation, the pseudo-rapidity of the muons from J/ψ is requested to be less than 5.3, but in reality, a small number of muons from outside this region can be reconstructed for example because of the magnetic field or multiple scattering. We assign a 1 % systematic error

[25] The biases are obtained by comparing the fitted values to the input values.

Table 4.12: Systematic errors on the production cross section measurements

Source	approximate value
Polarization	$0 - 20\,\%$ (depending on the bin)
Integrated luminosity	$10\,\%$
Branching fraction of $J/\psi \to \mu^+\mu^-$	$1\,\%$
Efficiency estimation	by Comparing with real data
Fit function (prompt J/ψ only)	$2\,\%$
Event loss outside the mass window	$2\,\%$
Monte Carlo Matching algorithm	$1\,\%$
Magnetic field effect on muon reconstruction	$1\,\%$

to account for muons which are reconstructed but which are missing from our Monte Carlo simulation due to the generator-level cut. The systematic errors from the total efficiency should be further studied with real data.

The systematic errors are summarized in Table 4.12.

4.14 Conclusion

In conclusion, we established the strategy to measure the cross section of prompt J/ψ and J/ψ from b with Monte Carlo data. The functions for fitting the different components are suggested and some ingredients will be obtained from real data. The result shows that with $5\,\mathrm{pb}^{-1}$ of data from LHCb, we can achieve relative statistical errors below 10% in every bin in the region $p_T \in [0, 7]\,\mathrm{GeV}/c$ and $\eta \in [3, 5]$. The systematic uncertainty from the polarization is dominant and should be further studied.

Chapter 5

J/ψ Polarization Measurement

The study in the previous chapter shows that the polarization of J/ψ affects a lot the differential cross section measurement. The systematic errors due to the unknown polarization may be larger than 30%. In order to reduce the polarization effect, we give the strategy for the polarization measurement in this chapter. Besides reducing the uncertainty on the experimental measurements, the polarization measurement is also very interesting for theory. As shown in Chapter 2, the polarization parameter (α) can be written as a combination of two different cross sections (see Eq. (2.24)) and most of the systematic errors from the theoretical calculations cancel and very good predictions can be made. Currently, most of the predictions do not agree with the CDF polarization measurements [17, 22, 23, 24, 25, 26, 27] and there is no theory model that can explain the measured differential cross section and polarization at the same time. Thus it is necessary to perform the polarization measurement at the high energy and in the forward region of LHCb.

In Chapter 2, we mentioned that in order to obtain the full information on polarization, we need to measure the results in the full angular space in at least two reference frames. In this thesis, the measurement is done in the full angular space but only in the helicity frame. The methods are similar for Gottfried-Jackson frame and Collins-Soper frame.

5.1 Polarization function

The polarization function in the full angular space given in Chapter 2 is:

$$P(\cos\theta,\phi)=\frac{1}{N}\frac{\mathrm{d}N}{\mathrm{d}(\cos\theta)\mathrm{d}\phi}\propto 1+\alpha_1\cos^2\theta+\alpha_2\sin 2\theta\cos\phi+\alpha_3\sin^2\theta\cos 2\phi, \tag{5.1}$$

where $\alpha_1,\alpha_2,\alpha_3$ are the polarization parameters to be measured. In different reference frames, the form of the polarization functions are the same while the polarization parameters have different values. In the helicity frame, the polarization axis (z' axis) is chosen to be the direction of the J/ψ momentum in the proton-proton center-of-mass frame, θ is defined as the angle between the momentum of the J/ψ decay product μ^+ in the J/ψ center-of-mass frame and the z' axis. ϕ is defined as the angle between the momentum of μ^+ in the J/ψ center-of-mass frame and the x' axis (see Chapter 2 for the definition).

As indicated in the above chapters, there are three components for the J/ψ production and only the polarizations of prompt J/ψ and J/ψ from b-hadrons are measured. Their polarization functions are noted as $P_{\mathrm{prompt}}(\cos\theta,\phi)$ and $P_b(\cos\theta,\phi)$ respectively. The polarization parameters to be measured are $\alpha_{p1},\alpha_{p2},\alpha_{p3}$ (prompt J/ψ) and $\alpha_{b1},\alpha_{b2},\alpha_{b3}$ (J/ψ from b-hadrons).

5.2 Polarization Measurement Strategy

In this thesis, the prompt and delayed components of J/ψ production are distinguished by fitting the experimental data and so do their polarization parameters. As in Chapter 4, the prompt J/ψ and J/ψ from b-hadrons are separated using the variable t_z. The signal events and background events are distinguished using the mass distribution. The measurement is done in all the 28 phase space regions defined in Chapter 4.

5.2.1 Fit Function

In each phase space region, the distributions of the reconstructed J/ψ can be written as

$$F(m,t_z,\cos\theta,\phi)=N_sF_s(m,t_z,\cos\theta,\phi)\epsilon_s(\cos\theta,\phi)+n_{\mathrm{bkg}}F_{\mathrm{bkg}}(m,t_z,\cos\theta,\phi), \tag{5.2}$$

Table 5.1: The correlation factors between different variables for signal (background) events

	t_z	m	cosθ	ϕ
t_z	-	0.008 (-0.074)	0.012 (0.72)	0.009 (0.18)
m	0.008 (-0.074)	-	-0.003 (0.018)	-0.009 (-0.015)
cosθ	0.012 (0.72)	-0.003 (0.018)	-	-
ϕ	0.009 (0.18)	-0.009 (-0.015)	-	-

where the indices "s" and "bkg" indicate the J/ψ signal and background events, m is the measured mass, and t_z is the lifetime variable defined in Chapter 4 to distinguish the prompt and delayed components. N_s is the number of J/ψ events before reconstruction, selection and trigger, $n_{\rm bkg}$ is the number of background events after reconstruction, selection and trigger. $\epsilon_s(\cos\theta, \phi)$ is the total efficiency of J/ψ including acceptance efficiency, reconstruction efficiency and trigger efficiency. It is also a function of p_T and η but since our measurement is done in small phase space regions, the dependence on p_T and η can be neglected in this small region. Thus $\epsilon_s(\cos\theta, \phi)$ is assumed to be independent of p_T and η in one given bin. One has to note that since $\epsilon_s(\cos\theta, \phi)$ is given as a function of $\cos\theta$ and ϕ, it does not depend on the polarization parameters $\alpha_1, \alpha_2, \alpha_3$.

$F_{\rm bkg}(m, t_z, \cos\theta, \phi)$ is the joint distribution of m, t_z, cosθ and ϕ, their marginal distributions are: $M_{\rm bkg}(m)$, $T_{\rm bkg}(t_z)$ and angular space distribution $P_{\rm bkg}(\cos\theta, \phi)$. The t_z and (cosθ, ϕ) background distributions can be obtained from the upper sideband of the mass distribution. As the analysis for t_z in Chapter 4, it is assumed that cosθ and ϕ are independent from m. Table 5.1 shows the correlation factors between the different variables for signal (background) events. The results in Table 5.1 show that the correlation between the angular space variables, mass and t_z are small for the signal events. For the background events, the correlations between the angular variables and t_z are a little larger, but due to the lack of background events in the minimum bias sample, we cannot make further studies on it and the correlations should be also checked for the real data. In the following analysis, we still assume the two to be independent. Figure 5.1 shows the cosθ and ϕ distributions for the background events in different mass regions where the red rectangles represent the distributions in the upper mass region [3.2, 3.5] GeV/c^2 and

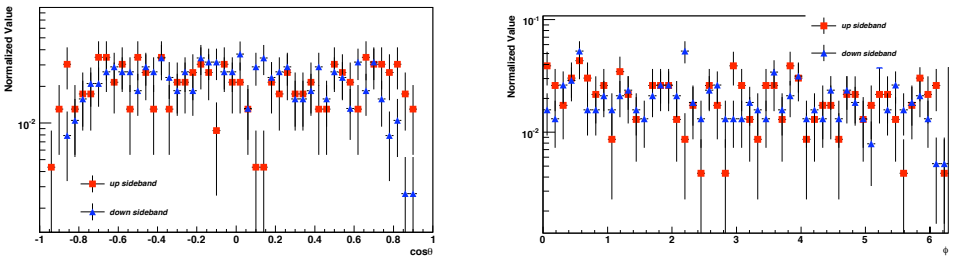

Figure 5.1: The comparison of cosθ (left) and ϕ (right) distributions in the upper (red square) and lower mass regions (blue triangle).

the blue triangles represent the distributions in the lower mass region [2.7, 3.0] GeV/c^2. The distributions in different mass regions agree very well and it is safe to use the distributions from the upper mass sideband to estimate the background distributions under the mass peak.

After the independence assumption, the background distribution $F_{\rm bkg}(m, t_z, \cos\theta, \phi)$ can be written as:

$$F_{\rm bkg}(m, t_z, \cos\theta, \phi) = M(m)_{\rm bkg} T(t_z)_{\rm bkg} P(\cos\theta, \phi)_{\rm bkg} \qquad (5.3)$$

and the signal distributions can be written as

$$F_s(m, t_z, \cos\theta, \phi) = M(m)_s \times (N_p T_p P_p \epsilon_p + N_b T_b P_b \epsilon_b + N_{\rm tail} T_{\rm tail} P_{\rm tail} \epsilon_{\rm tail}), \quad (5.4)$$

here the indices "p", "b" and "tail" represent the prompt J/ψ, J/ψ from b-hadrons and the tail events respectively. T and P are the t_z and (cosθ, ϕ) distributions of the different components. $N_p, N_b, N_{\rm tail}$ are the number of prompt J/ψ, J/ψ from b-hadrons and tail events before the reconstruction, selection and trigger. $\epsilon_{p,b,{\rm tail}}$ are the total efficiency of the different components. The discussion in Chapter 4 shows that the L0 efficiencies for the prompt J/ψ and J/ψ from b-hadrons are different and it is caused by other particles of the event. In the analysis, we assume that the shapes of the efficiencies of the two components as a function of cosθ and ϕ are the same and they only differ from each other by an overall factor which describes the different effects of the other particles in the event. Figure 5.2 shows the distributions of cosθ and ϕ for the L0 efficiencies which proves our assumption. The results are for J/ψ with $\eta \in [3, 3.5]$ and they are similar for other bins. The prompt J/ψ is represented by blue rectangles and the J/ψ from b-hadrons is represented by red triangles.

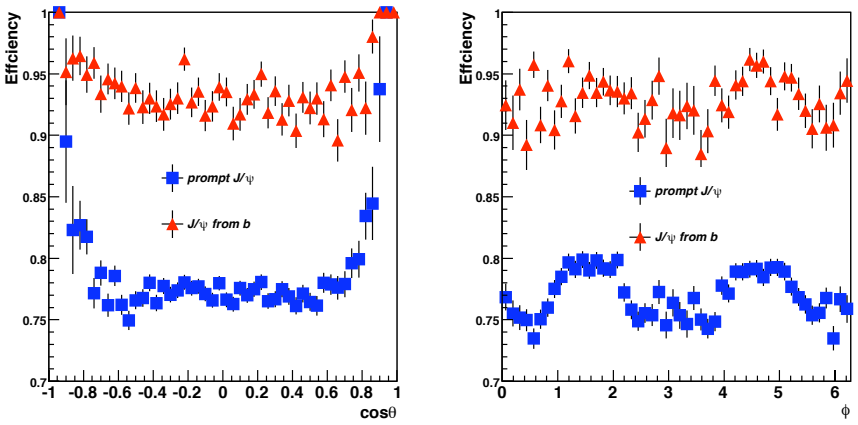

Figure 5.2: The comparison of the L0 efficiency as a function of cosθ (left) and ϕ (right) for prompt J/ψ (blue rectangle) and J/ψ from b-hadrons (red rectangle).

After the above assumption, the distribution for the signal events can be further written as:

$$F_s(m, t_z, \cos\theta, \phi) = M_s \times (N_p f_p T_p P_p + N_b f_b T_b P_b + N_{\rm tail} f_{\rm tail} T_{\rm tail} P_{\rm tail})\epsilon, \quad (5.5)$$

where ϵ is the normalized efficiency of the signal events (it is the same for all the components), $f_p, f_b, f_{\rm tail}$ are the ratios of efficiencies between the different components and the normalized efficiency. They are independent of cosθ and ϕ. If the number of prompt J/ψ, J/ψ from b-hadrons and tail events after reconstruction, selection and trigger are noted as $n_p, n_b, n_{\rm tail}$, then we have

$$\begin{aligned} n_p &= N_p \times f_p; \\ n_b &= N_b \times f_b; \\ n_{\rm tail} &= N_{\rm tail} \times f_{\rm tail} \end{aligned} \quad (5.6)$$

and the final fit function for the signal events can be written as

$$F_s(m, t_z, \cos\theta, \phi) = M_s \times (n_p T_p P_p + n_b T_b P_b + n_{\rm tail} T_{\rm tail} P_{\rm tail})\epsilon = M_s T P_s \epsilon. \quad (5.7)$$

In the following equations, we abbreviate the notation for the signal t_z and angular space distributions as TP_s. As in Chapter 4, it is assumed that the fraction of b-hadrons in the tail events are the same as the one in the J/ψ signal events and the relations of the polarization parameters between the

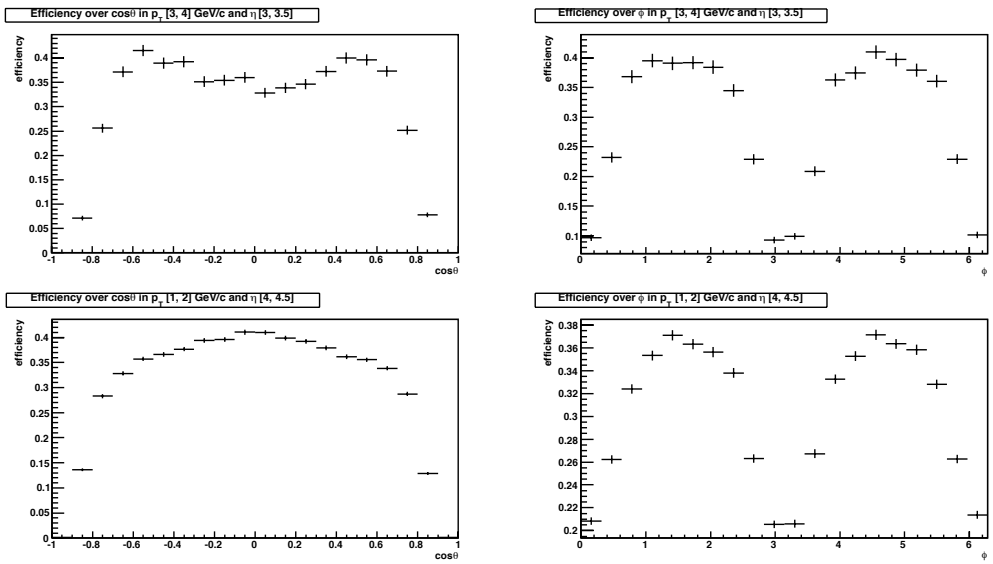

Figure 5.3: The reconstruction and acceptance efficiencies for J/ψ with $p_T \in$[3, 4] GeV/c, $\eta \in$[3, 3.5] (The upper two graphs) and $p_T \in$[1, 2] GeV/c, $\eta \in$[4, 4.5] (The bottom two graphs).

tail events and the other two components can be written as:

$$\alpha_i^{\text{tail}} = \frac{n_p}{n_p + n_b}\alpha_i^p + \frac{n_b}{n_p + n_b}\alpha_i^b \qquad i = 1, 2, 3. \tag{5.8}$$

Figure 5.3 shows the reconstruction and acceptance efficiencies for J/ψ events with $p_T \in [3, 4]$ GeV/c, $\eta \in [3, 3.5]$ (the upper two graphs) and $p_T \in$[1, 2] GeV/c, $\eta \in$[4, 4.5] (the bottom two graphs). We can see that the efficiencies over cosθ depends a lot on p_T and η and it may have large effects on the polarization measurement. In order to obtain a correct polarization measurement, the efficiencies in each p_T and η bin should be correctly measured which may need a huge amount of Monte Carlo events [1]. It is hard to produce such a big amount of simulated data in reality and in order to avoid the problem, the efficiency over cosθ and ϕ in each p_T, η bin is parametrized using three parameters.

[1] In the LHCb analysis for the polarization study, the efficiencies will be obtained from Monte Carlo.

5.2.2 Maximum Log-likelihood Fit

Usually the log-likelihood function for fitting the measured sample with a fit function F can be written as

$$L = \sum_i \ln(F_i) \stackrel{n\to\infty}{=} -n \int F \ln(F), \tag{5.9}$$

where i is the i-th measured value. When $n \to \infty$, the sum becomes the integration over the measured variables which are used in the fit and in the following equations, the integrated variables are not written out specially. The fit parameters that maximize the log-likelihood function are the estimated values of the variables [2]. In our measurement, the fit function is $F(m, t_z, \cos\theta, \phi)$. In order to reduce the dependence on the efficiency function, we hope to use only the signal part $F_s(m, t_z, cos\theta, \phi)$ to fit the reconstructed J/ψ distributions instead of the total function $F(m, t_z, \cos\theta, \phi)$, then the efficiency function can be extracted out. A weight function ($w(m)$) is needed to compensate for the contributions of the background part and the log-likelihood function can be written as:

$$\begin{aligned} L &= -\sum_{s+b} w(m) \ln(TP_s \times \epsilon) \qquad (5.10)\\ &= -\sum_{s} w(m) \ln(TP_s) - \sum_{b} w(m) \ln(TP_s) - \sum_{s+b} w(m) \ln\epsilon. \end{aligned}$$

As there are no fit parameters in the last term, it is a constant and can be neglected during the fit. When $n \to \infty$ ($n = n_s + n_{\rm bkg}$), the above function becomes

$$L \stackrel{n\to\infty}{=} -n_s \int M_s TP_s \times w(m) \ln(TP_s) - n_{\rm bkg} \int M_{\rm bkg} T_{\rm bkg} P_{\rm bkg} \times w(m) \ln(TP_s). \tag{5.11}$$

Comparing it with Eq. (5.9) to make an unbiased fit (the two should have similar formulas), we obtain

$$\int w(m) M_{\rm bkg}(m) {\rm d}m = 0; \tag{5.12}$$

$$\int w(m) M_s(m) {\rm d}m = c \neq 0, \tag{5.13}$$

[2] Limits can be imposed on the fit parameters to satisfy physics requirements

If the weight function $w(m)$ is set to satisfy the above requirements, Eq. (5.11) differs from Eq. (5.9) with only a factor c. Since this factor does not affect the estimated values from the fit, the fit results are unbiased. But the errors are underestimated due to the statistical fluctuation of background events which we will discuss below.

In the maximum log-likelihood fit, the fit function should be normalized. From Chapter 4 we know that the t_z fit function used is for the distribution after reconstruction, selection and trigger. It does not depend on the total efficiency.

For the polarization function, the normalized distribution should be

$$P(\cos\theta,\phi) = \frac{1+\alpha_1\cos^2\theta+\alpha_2\sin 2\theta\cos\phi+\alpha_3\sin^2\theta\cos 2\phi}{1+\alpha_1\times r_1+\alpha_2\times r_2+\alpha_3\times r_3}, \tag{5.14}$$

where r_1, r_2, r_3 are defined as

$$r_1 = \frac{\int\cos^2\theta\epsilon\mathrm{d}\cos\theta\mathrm{d}\phi}{\int\epsilon\mathrm{d}\cos\theta\mathrm{d}\phi}; \tag{5.15}$$

$$r_2 = \frac{\int\sin 2\theta\cos\phi\epsilon\mathrm{d}\cos\theta\mathrm{d}\phi}{\int\epsilon\mathrm{d}\cos\theta\mathrm{d}\phi}; \tag{5.16}$$

$$r_3 = \frac{\int\sin^2\theta\cos 2\phi\epsilon\mathrm{d}\cos\theta\mathrm{d}\phi}{\int\epsilon\mathrm{d}\cos\theta\mathrm{d}\phi}, \tag{5.17}$$

The r_1, r_2, r_3 values are obtained from the fully simulated Monte Carlo sample with finite events; they are calculated as:

$$r_1 = \frac{\sum_i\cos^2\theta_i}{N}; \tag{5.18}$$

$$r_2 = \frac{\sum_i\sin 2\theta_i\cos\phi_i}{N}; \tag{5.19}$$

$$r_3 = \frac{\sum_i\sin^2\theta_i\cos 2\phi_i}{N}, \tag{5.20}$$

where N is the number of events used in the defined phase space region.

Table 5.2: The r_1, r_2, r_3 values and their covariance matrix calculated for J/ψ events in $p_T \in [3,4]$ GeV/c, $\eta \in [3, 3.5]$.

	$r_1 = 0.214 \pm 0.002$	$r_2 = -0.072 \pm 0.004$	$r_3 = -0.225 \pm 0.004$
r_1	1	-0.0576	0.163
r_2	-0.0576	1	- 0.288
r_3	0.163	-0.288	1

Their covariance matrix can be obtained by:

$$\begin{aligned}
r_{11} &= \frac{\sum_i \cos^4\theta_i/N - r_1^2}{N^2}; \\
r_{22} &= \frac{\sum_i \sin^2 2\theta_i \cos^2\phi_i/N - r_2^2}{N^2}; \\
r_{33} &= \frac{\sum_i \sin^4\theta_i \cos^2 2\phi_i/N - r_3^2}{N^2}; \\
r_{12} &= r_{21} = \frac{\sum_i \cos^2\theta_i \sin 2\theta_i \cos\phi_i/N - r_1 r_2}{N^2}; \\
r_{13} &= r_{31} = \frac{\sum_i \cos^2\theta_i \sin^2\theta_i \cos 2\phi_i/N - r_1 r_2}{N^2}; \\
r_{23} &= r_{32} = \frac{\sum_i \sin 2\theta_i \sin^2\theta_i \cos 2\phi_i \cos 2\phi_i/N - r_1 r_2}{N^2}.
\end{aligned} \tag{5.21}$$

Table 5.2 lists the calculated values for J/ψ events in $p_T \in [3,4]$ GeV/c, $\eta \in [3, 3.5]$.

To summarize, the fit function for the polarization measurement is

$$L = -\sum_{s+b} w(m) \ln(n_p T_p P_p + n_b T_b P_b + n_{\rm tail} T_{\rm tail} P_{\rm tail}), \tag{5.22}$$

it is a 3-D fit with t_z, cosθ and ϕ as input parameters and the mass function as a weight function. Inside, there are 12 fit parameters where half of them are the polarization parameters ($\alpha_{p1,p2,p3}$, $\alpha_{b1,b2,b3}$), half of them come from t_z (see Chapter 4); besides there are three input constants r_1, r_2, r_3 to give the dependence on the efficiency. As described above, the fit errors are not correctly estimated and they should be modified before used. In this thesis, a toy Monte Carlo experiment is used to study the difference between the fitted errors and the real errors.

5.3 Toy Monte Carlo Production

The toy Monte Carlo experiments are produced with the following procedure. First, the mass distribution is obtained using a Crystal Ball function for the signal events and a linear function for the background with the parameters obtained from the minimum bias sample [3]. The t_z distribution is generated from Eq. (4.14) for the J/ψ signal events with mean set to be 0, scale set to be 1 and the average b lifetime set to be 1.4 ps. The b fraction in the toy Monte Carlo is set to be 0.07. The tail distribution is obtained with the method discussed in Chapter 4 and its fraction is set to be 0.01. The $t_{\rm err}$ distribution is obtained from the inclusive J/ψ sample. For the angular space distributions, the background distribution is generated as a flat distribution and the signal part is obtained through the following precedure:

1. The distributions of the J/ψ p_T and η are obtained directly from the distribution of fully simulated sample.

2. The generated J/ψ are decayed with different polarization settings to generate μ particles. The μ particles are required to be within the μ detector acceptance, that is: the angle between the μ momentum projection in the horizontal plane and the z axis is between 20 and 306 mrad, the angle between the μ momentum projection in the vertical plane and the z axis is between 16 and 258 mrad. We also require that the transverse momentum of the generated J/ψ is more than 0.7 GeV/c (one of the selection criteria for the J/ψ reconstruction).

3. The efficiency (including reconstruction, selection and trigger efficiency) is then added to the J/ψ events: since the selection criteria on the J/ψ particles do not affect the efficiency as a function of $\cos\theta$ and ϕ [4], they do not affect the normalized efficiency function and its effect is not considered during the simulation. The efficiency mainly depends on the efficiency (including reconstruction and selection efficiency [5]) of μ

[3] The parameter settings of the signal mass distribution is: $n = 1.46$, $\alpha = 1.78$, $\mu = 3.097$, $\sigma = 0.11$ (see Chapter 4). The probability density function of the background mass distribution is described by $(1 - 0.27 \times m)$ and it is normalized in the mass range studied ($[2.697, 3.497]$ GeV/c^2). The S/B in this region is set to be 1.5.

[4] The two selection criteria on J/ψ are the mass selection and vertex quality selection.

[5] The trigger efficiency is considered independently below since it applies to the whole events.

particles and the efficiencies of the two μ are considered to be independent. In fact, there are two possibilities that the efficiency of the two μ can be correlated, one is when the two μ are near each other and the reconstruction of one of the μ tracks correlates with the reconstruction of the other μ. This kind of correlation can be avoided by restricting the range of cosθ and ϕ we study. In the current simulation, the effect is not so obvious and we still use the full angular space range for the analysis. Another possible effect comes from the DiMuon L0 trigger as it requires the sum of two μ momenta to be larger than 1.3 GeV/c [6]. The effect of this trigger can be reduced by the requirement on the μ p_T selections [7]. Based on the assumption that the efficiency of the two μ are independent, the J/ψ efficiency can be written as

$$\epsilon = \epsilon(\mu^+) \times \epsilon(\mu^-) \times \epsilon(J/\psi, \text{event}), \tag{5.23}$$

where $\epsilon(\mu)$ is the efficiency for a single μ, $\epsilon(J/\psi, \text{event})$ is the efficiency of the selection criteria on J/ψ and the whole events (like L0 calorimeter trigger), it can be ignored since it is independent of $\cos\theta$ and ϕ. The μ efficiency can be further written as

$$\epsilon(\mu) = \epsilon(p, \eta, \phi_{\text{lab}}) = \epsilon(p) \times \epsilon(\eta, \phi_{\text{lab}}), \tag{5.24}$$

here p and η are the μ momentum and pseudo-rapidity, ϕ_{lab} is the angle between the μ momentum and the x axis. In order to simplify the simulation, it is assumed that the momentum part $\epsilon(p)$ is independent from the angular distribution part $\epsilon(\eta, \phi_{\text{lab}})$ which is assumed to be fully defined by the acceptance efficiency of the detector and is included in the above simulation. The only thing we need to consider is the efficiency dependence on the momentum which is given by

$$\epsilon(p) = \frac{0.7}{1. + \exp(13.1 - 3.6 \times p)}. \tag{5.25}$$

This efficiency includes the reconstructible efficiency, reconstructed efficiency, μ identification efficiency and selection efficiency, all of them can be obtained from real data. For the current analysis, all the parameters of Eq. (5.25) come from fully simulated Monte Carlo sample.

[6] This trigger may affect the $\cos\theta$ distribution if the two μ particles are close to each other as during the fast reconstruction at L0 level, these two μ are usually considered as single particles and they need to pass the single muon trigger with tighter requirement (see Chapter 3).

[7] For example, if we require the transverse momentum of both μ to be more than 1.4 GeV/c, the events passing this requirement should certainly pass the DiMuon l0 trigger.

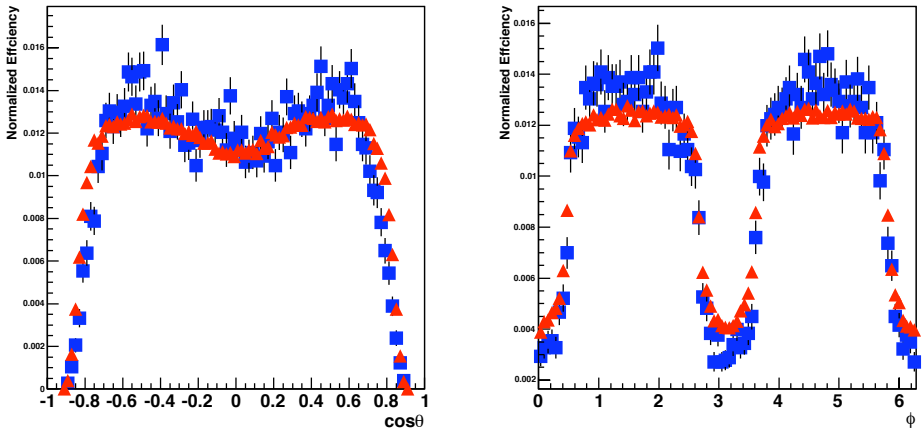

Figure 5.4: The comparison of efficiencies as a function of cosθ (left) and ϕ (right) for the toy Monte Carlo sample (red triangles) and fully simulated sample (blue squares).

Figure 5.4 shows the efficiency comparison between the toy Monte Carlo sample and the fully simulated sample for J/ψ events in $p_T \in [3, 4]$ GeV/c, $\eta \in [3, 3.5]$. We can see that even with the above simple assumptions, the distributions from the toy Monte Carlo are similar to the fully simulated sample and most of the conclusions obtained from it can be safely used for the fully simulated samples and for real data. There are still some differences between the two samples and if the efficiency obtained from the toy Monte Carlo sample is used in the fit, the bias on α_1 is around 0.2-0.3. Thus the toy Monte Carlo sample is only used for cross check of our fitting procedure and for the study of errors.

Since in our fit strategy, only the three parameters r_1, r_2, r_3 obtained from efficiencies are used, Table 5.3 shows the r_1, r_2, r_3 values and its error matrix from the toy Monte Carlo sample for J/ψ events in $p_T \in [3, 4]$ GeV/c and $\eta \in [3, 3.5]$, to be compared with values of the fully simulated samples (Table 5.2).

One has to note that, in the above toy simulation, the effects like the magnetic field, resolution of $\cos\theta$ and ϕ, radiative decays of J/ψ are not considered and the samples are generated with t_z, mass and angular distributions independent of each other. According to the above method, three samples with different polarization scenarios are generated, with the same polariza-

Table 5.3: The r_1, r_2, r_3 values and their error matrix for the toy Monte Carlo sample with J/ψ $p_T \in [3, 4]$ GeV/c, $\eta \in [3, 3.5]$.

	$r_1 = 0.2327 \pm 0.0003$	$r_2 = -0.1126 \pm 0.0006$	$r_3 = -0.1592 \pm 0.0007$
r_1	1	-0.134	0.118
r_2	-0.134	1	-0.349
r_3	0.118	-0.349	1

tion for the prompt J/ψ and $/\psi$ from b-hadrons. The polarization parameters for the three samples are $(\alpha_1 = 0, \alpha_2 = 0, \alpha_3 = 0)$, $(\alpha_1 = -0.5, \alpha_2 = -0.05, \alpha_3 = -0.05)$ and $(\alpha_1 = 0.5, \alpha_2 = 0.05, \alpha_3 = 0.05)$. In the following analysis, only the results of the first sample are shown, if not specified, other samples have similar results.

5.4 Weight Function

There are a lot of different methods for choosing the weight functions which satisfy Eq. (5.13), different weight functions may give different errors and in order to reduce the errors, a research on the following series of functions is performed:

$$w(m) = \begin{cases} +1 & m \in [3.097 - m_0, 3.097 + m_0] \\ -1 & m \in [2.697, 2.697 + m_0] \cup [3.497 - m_0, 3.497] \\ 0 & \text{else,} \end{cases} \quad (5.26)$$

where m_0 is a variable which can be changed, it defines the different selection windows used. Eq. (5.26) is based on the assumption that the background function is a linear function. For other background shapes, similar methods can be used: first, obtain the background shape from the mass fit [8] and then choose the regions so that the number of events in the central region is the same as the number of events in the sidebands. The weight of the events in the two regions are set to be +1 and -1 respectively. The weight function obtained using the above method satisfies the requirement of Eq. (5.13). Using this

[8]Some other methods can also be used to obtain the background shape like the combination of same charge muons if the background events are all combinatorial.

weight function, the contributions of the background events are cancelled but part of the signal events are also cancelled. The effective number of signal events left is defined by $n_{sig} \times c$. In order to reduce the errors, the weight function should be set to get a larger effective number of signal events. On the other hand, the background contribution cancels exactly when $n \to \infty$. For a finite statistics, the background contributions may have residuals due to the statistical fluctuations and this may induce extra errors. Thus when choosing the weight function, we should both increase the effective signal events and reduce the fluctuations due to the finite number of events, the ideal case is when the following formula:

$$\frac{n_s \int w(m) M_s(m) dm}{n_{\text{bkg}} \sqrt{\int w^2(m) M_b(m) dm}} \tag{5.27}$$

has the maximum value. In this case, the errors of the polarization parameters are the smallest. In the thesis, we only find the best weight function using the function series defined in Eq. (5.26) and show the effect of different weight functions by varying m_0. The study is performed for the J/ψ events with $p_T \in [2, 3]$ GeV/c, $\eta \in [3.5, 4]$. First, the fit is performed for the weight function with different m_0 and the errors of the polarization parameters are obtained. In order to know the difference between the fit errors and the real errors, the fit is performed 100 times and the pull of the results are filled into histograms. Here pull is defined as:

$$\text{pull} = \frac{\text{Fit Value - Input Value}}{\text{Fit Error}}. \tag{5.28}$$

The σ of the pull distribution is the difference between the two errors (real error and fit error). Figure 5.5 shows the pull distributions for the polarization parameters of prompt J/ψ and J/ψ from b-hadrons with $m_0 = 0.2$ GeV/c^2 and the fit parameters on the graph are $\alpha_{p1}, \alpha_{p2}, \alpha_{p3}, \alpha_{b1}, \alpha_{b2}, \alpha_{b3}$ respectively. From the graphs, we can see that the mean values of the pull distributions agree with 0, this means our fit method is unbiased. The σ of the pull distributions are from 1.15 to 2.10, which as expected shows that the fit errors are underestimated.

The results performed for different m_0 are shown in Figure 5.6 where the blue rectangles represent the fit errors (left axis), the red stars represent the σ of the pull distributions (right axis) and the magenta line shows the real errors calculated by (fit errors)$\times\sigma$ (left axis). From the graph, we can

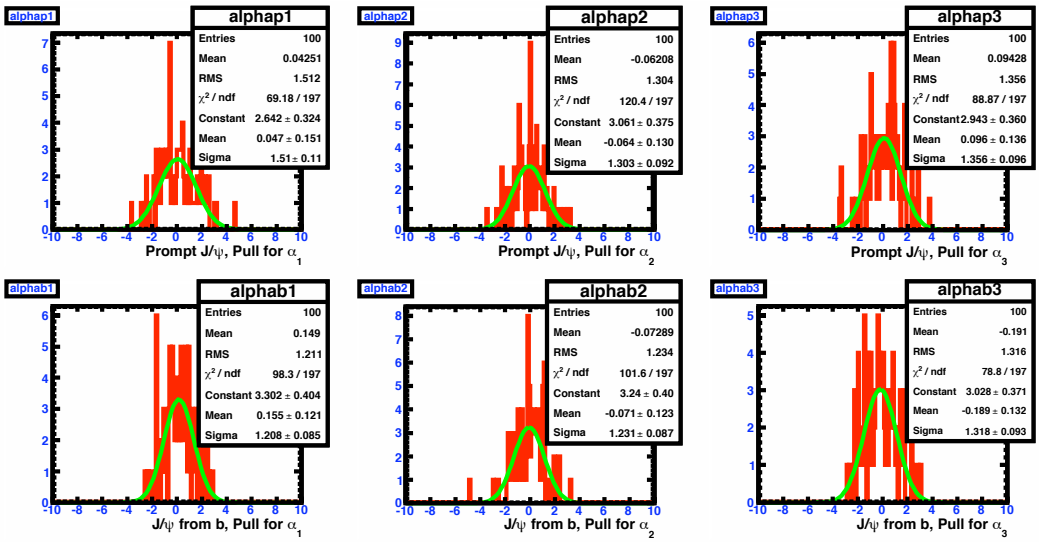

Figure 5.5: The pull distributions for the polarization parameters of prompt J/ψ and J/ψ from b-hadrons, the fit parameters on the graph are $\alpha_{p1}, \alpha_{p2}, \alpha_{p3}, \alpha_{b1}, \alpha_{b2}, \alpha_{b3}$ respectively.

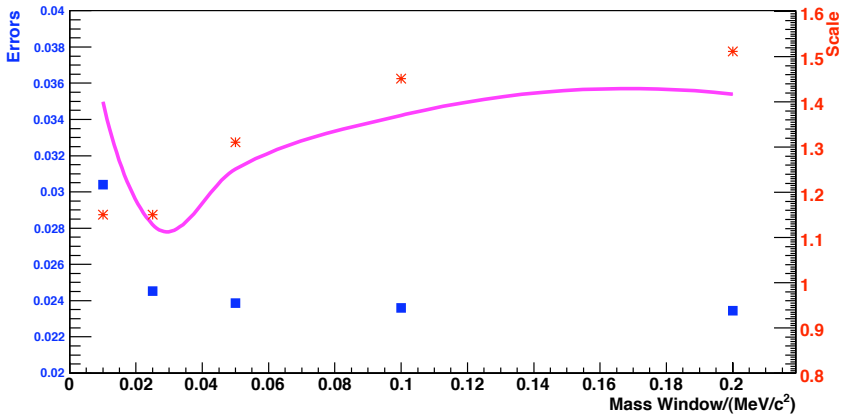

Figure 5.6: The effects of the weight functions (Eq.(5.26)) on the errors of the polarization parameter α_{p1}, where the blue rectangles represent the fit errors (left axis), the red stars represent the σ of the pull distributions (right axis) and the magenta line shows the real errors (left axis). The real errors are calculated using (fit errors)$\times\sigma$

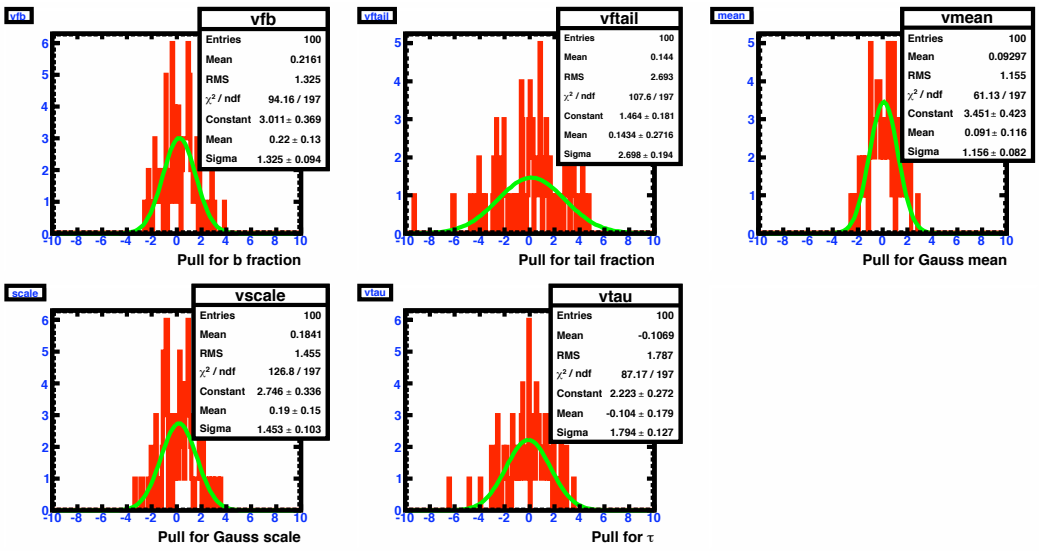

Figure 5.7: The pull distributions of the parameters in the t_z component.

see that when the chosen mass window is large, the errors are larger due to the large statistic fluctuation of the background event subtraction. When the mass window is small, the σ of the pull distribution is close to 1 but due to the reduced the number of effective signal events, the statistical error increases and the real error becomes larger. When $m_0 \in [0.025, 0.03]$ GeV/c^2, the real errors are the smallest and the differences between the real errors and the fit errors are around 1.1. In the discussion below, we use the weight function defined in Eq. (5.26) with $m_0 = 0.025$ GeV/c^2. Of course, there are other ways to choose the weight functions [132], but no matter which weight functions are used, the difference between the real errors and fit errors should be considered.

Since the analysis uses a combined fit over t_z, cosθ and ϕ, the pull distributions for the fit parameters in the t_z distribution are also shown in Figure 5.7. They give similar results as for the polarization parameters: the results are unbiased while the errors are underestimated. In the graph, only the fractions of b-hadrons and tail events are given instead of the exactly measured numbers as the expected numbers for them in the fit are the effective numbers instead of the real numbers. Since it is assumed that the mass distribution is independent from the other two variables, the fractions (b fraction, tail fraction) are considered to be the same than the fractions which would be obtained from the weighted sample. Figure 5.8 shows the

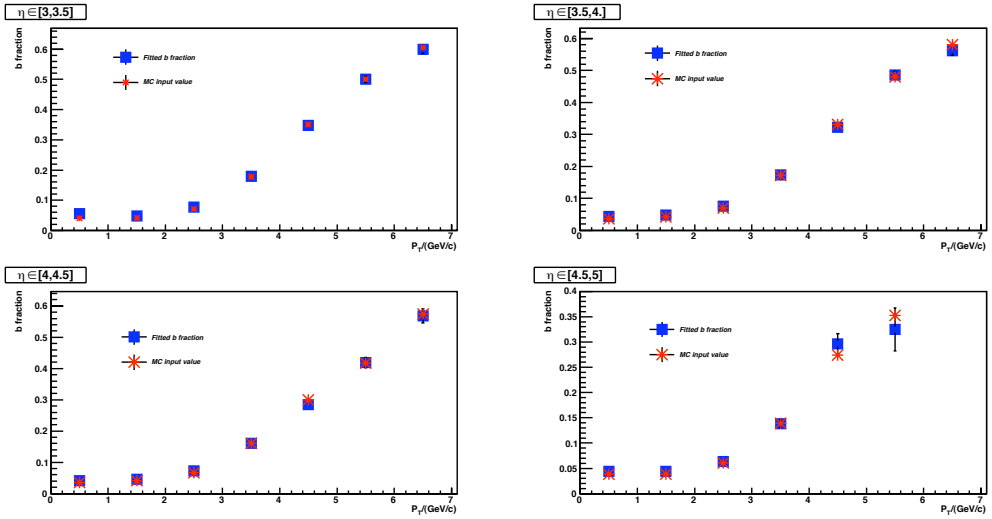

Figure 5.8: The comparison for the b fractions as a function of p_T between the fit results (blue rectangles) and input values (red stars). Different graphs represent different η regions: $[3, 3.5], [3.5, 4], [4, 4.5], [4.5, 5]$.

comparison of the b fractions as a function of p_T between the fit results (blue rectangles) and input values (red stars). Different graphs represent different η regions: $[3, 3.5], [3.5, 4], [4, 4.5], [4.5, 5]$. We can see that the two agree very well. Compared with the results obtained in Chapter 4, the two results are similar both for the fit numbers and for the fit errors.

5.5 Resolution Effect

The fit function for the polarization Eq. (5.14) does not include the resolution effects of $\cos\theta$ and ϕ. A study is needed to make sure that it may not bias our analysis. We use another toy Monte Carlo sample to study its effect for the cosθ part. The toy Monte Carlo is generated with the distributions $1 + \alpha\cos^2\theta$ and different resolutions are then used for cosθ, that is for each $\cos\theta$ generated, it is smeared by a Gaussian function with the resolutions. For the regions around cos$\theta = -1$ and cos$\theta = +1$, a trick is applied which assumes that the function $(1+\alpha\cos^2\theta)$ is periodical to avoid unphysical values with $|\cos\theta| > 1$. The fit results of the α parameters for different resolutions are then listed in Table 5.4. Here, several resolution combinations are considered:

Table 5.4: The effect of different resolution values on the fit results of the α parameters with the input value $\alpha = 0.5$. The resolution range listed below is from the middle to the edge, for example, 0.001-0.005 means that the resolution is 0.001 when $\cos\theta = 0$ and the resolution is 0.005 when $\cos\theta = \pm 1$.

$\cos\theta$ Resolution	0.1	0.2	0.5	1
α Fit Results	0.498 ± 0.003	0.5 ± 0.003	0.503 ± 0.003	0.477 ± 0.003
$\cos\theta$ Resolution	0.001-0.005	0.005-0.025	0.01-0.05	0.05-0.25
α Fit Results	0.505 ± 0.003	0.494 ± 0.003	0.481 ± 0.003	0.168 ± 0.003
$\cos\theta$ Resolution	0.005-0.001	0.025-0.005	0.05-0.01	0.25-0.05
α Fit Results	0.5 ± 0.003	0.503 ± 0.003	0.516 ± 0.003	0.894 ± 0.003

1. The resolutions are the same over cosθ range (the first two lines): the fit results Table 5.4 shows that in this situation, the resolutions affect little the fit results.

2. The resolutions are different over cosθ range, it is larger at the edge than in the middle (the third and forth lines): in this case, the fit results are sensitive to the resolutions and the systematic bias is around 2% when the resolutions are from 0.01 to 0.05 (from the middle to the edge).

3. The resolutions are different over cosθ range, it is larger in the middle than at the edge (the last two lines): the same as the second case.

Figure 5.9 shows the difference between the measured cosθ and the true generated values in the fully simulated sample and we can see that there are mainly two components, most of the events are in the central part with small values and the resolutions of these events for different cosθ are listed in Table 5.5. From the resolutions listed in the table, we can see that the effect of the resolutions from these events are negligible. The other part of the resolution is a long tail which is mainly due to the low transverse momentum muons from J/ψ and the fraction of these events is less than 1% which means that its effect on the polarization measurement should be smaller than 1%. In all, the effect of the $\cos\theta$ resolution in the angular space is less than 1% and when constructing the fit function, it is reasonable to ignore the resolution contributions.

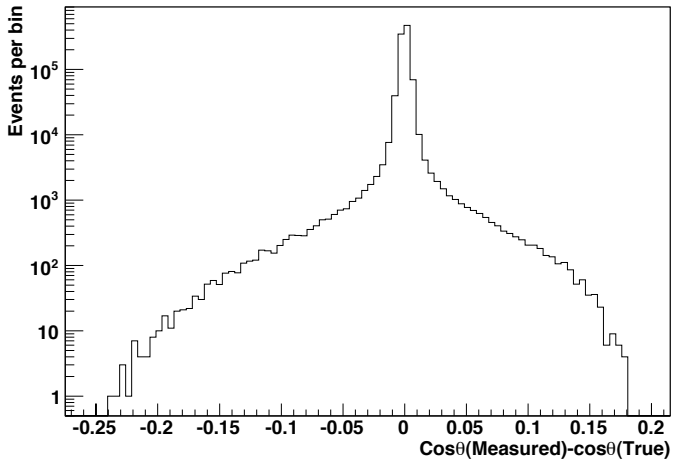

Figure 5.9: The distribution for the difference between the measured cosθ and input values.

Table 5.5: Resolutions seen for the fully simulated samples in different cosθ regions.

Range of cosθ	[-1,-0.9] $\cup$ [0.9,1]	[-0.55,-0.45] $\cup$ [0.45,0.55]	[-0.1,0.1]
Resolution	0.001	0.003	0.0035

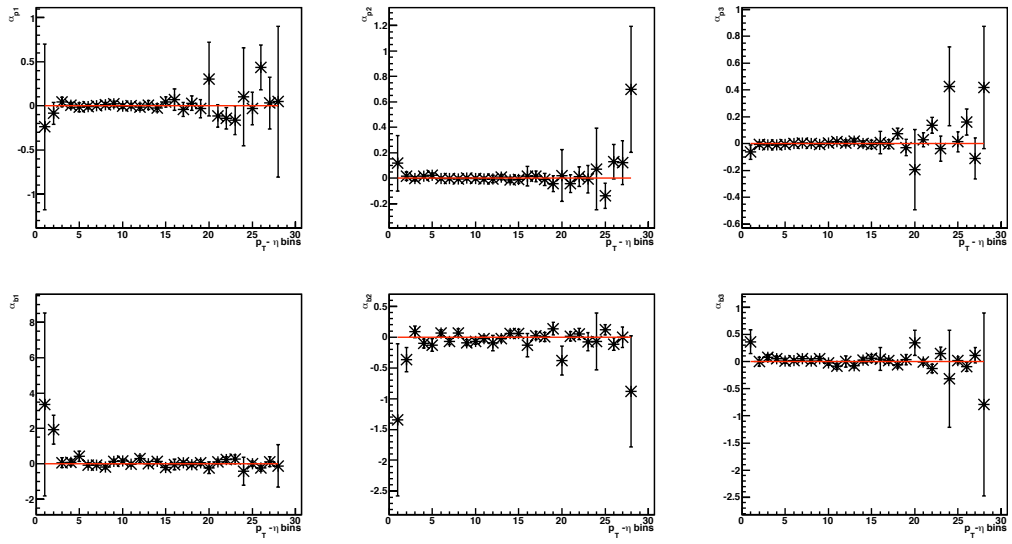

Figure 5.10: The fit results for the polarization parameters of prompt J/ψ and J/ψ from b-hadrons in different p_T and η bins. The upper three graphs are for $\alpha_{p1}, \alpha_{p2}, \alpha_{p3}$ and the lower three graphs are for $\alpha_{b1}, \alpha_{b2}, \alpha_{b3}$. The horizontal axis represents the 28 phase space bins.

5.6 Fit Results for the Fully Simulated Sample

According to the above fit method, Figure 5.10 shows the fit results for the polarization parameters of prompt J/ψ and J/ψ from b-hadrons in different p_T and η bins. The upper three graphs are for $\alpha_{p1}, \alpha_{p2}, \alpha_{p3}$ and the lower three graphs are for $\alpha_{b1}, \alpha_{b2}, \alpha_{b3}$. The horizontal axis represents the 28 phase space bins. The red line is the input value which is 0. From the graph we can see that the fit results in different bins agree very well with the input values and the large errors in some bins are due to the lack of statistics. We list the values for α_{p1}, α_{b1} in Table 5.6 and Table 5.7 for all the bins as the two parameters are the most interesting ones for theory.

5.6.1 Error Analysis

There are several sources for the errors of the polarization parameters:

1. The modified fit errors: in the above sections, we mentioned that the fit errors σ_{fit} are underestimated and the factors between the real errors

Table 5.6: The fit results for α_{p1} (input value $\alpha_{p1} = 0$)

p_T (GeV/c)	$\eta \in [3 - 3.5]$	$\eta \in [3.5 - 4]$	$\eta \in [4 - 4.5]$	$\eta \in [4.5 - 5]$
$0 - 1$ (GeV/c)	-0.24 ± 0.94	-0.09 ± 0.12	0.04 ± 0.05	0.00 ± 0.04
$1 - 2$ (GeV/c)	-0.02 ± 0.05	-0.01 ± 0.03	0.00 ± 0.02	0.01 ± 0.02
$2 - 3$ (GeV/c)	0.02 ± 0.03	-0.00 ± 0.03	0.00 ± 0.03	-0.01 ± 0.04
$3 - 4$ (GeV/c)	0.01 ± 0.05	-0.02 ± 0.04	0.05 ± 0.06	0.07 ± 0.12
$4 - 5$ (GeV/c)	-0.04 ± 0.08	0.03 ± 0.08	-0.03 ± 0.10	0.30 ± 0.42
$5 - 6$ (GeV/c)	-0.12 ± 0.13	-0.14 ± 0.12	-0.16 ± 0.16	0.10 ± 0.55
$6 - 7$ (GeV/c)	-0.03 ± 0.19	0.44 ± 0.26	0.03 ± 0.29	0.05 ± 0.86

Table 5.7: The fit results for α_{b1} (input value $\alpha_{b1} = 0$)

p_T (GeV/c)	$\eta \in [3 - 3.5]$	$\eta \in [3.5 - 4]$	$\eta \in [4 - 4.5]$	$\eta \in [4.5 - 5]$
$0 - 1$ (GeV/c)	3.35 ± 5.19	1.94 ± 0.82	0.06 ± 0.28	0.08 ± 0.19
$1 - 2$ (GeV/c)	0.43 ± 0.28	-0.07 ± 0.12	-0.07 ± 0.10	-0.18 ± 0.11
$2 - 3$ (GeV/c)	0.14 ± 0.13	0.17 ± 0.10	-0.03 ± 0.10	0.28 ± 0.20
$3 - 4$ (GeV/c)	0.00 ± 0.11	0.15 ± 0.11	-0.22 ± 0.12	-0.04 ± 0.29
$4 - 5$ (GeV/c)	0.05 ± 0.12	-0.05 ± 0.12	0.06 ± 0.17	-0.22 ± 0.34
$5 - 6$ (GeV/c)	0.12 ± 0.14	0.23 ± 0.16	0.26 ± 0.25	-0.42 ± 0.79
$6 - 7$ (GeV/c)	0.01 ± 0.15	-0.24 ± 0.17	0.12 ± 0.28	-0.12 ± 1.2

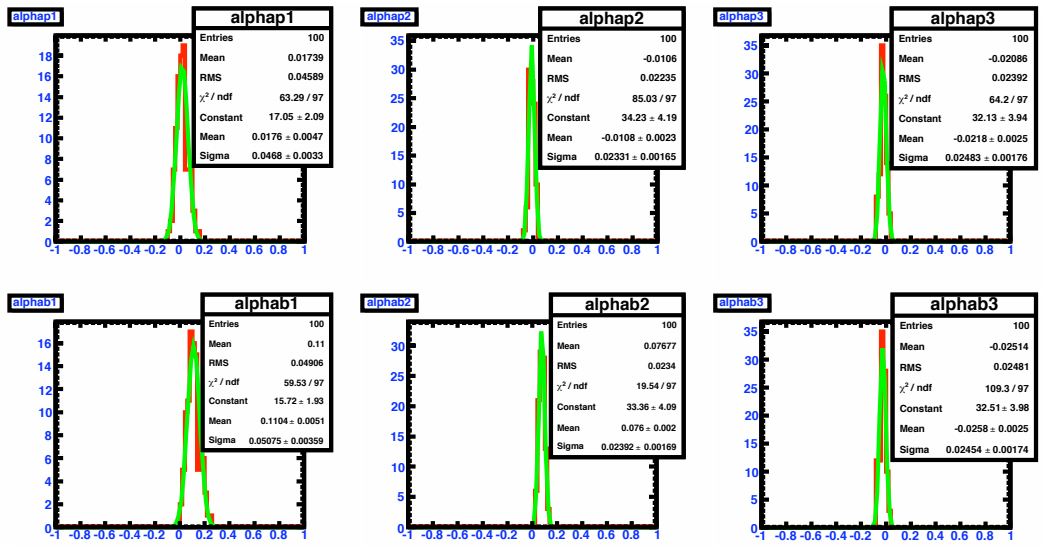

Figure 5.11: The errors of the polarization parameters induced by the statistical errors of r_1, r_2, r_3.

and the fit errors are from toy Monte Carlo for each p_T and η bins. According to the above study, we choose the factor to be 1.1 for all the bins for simplicity. The real errors from the fit are then $1.1\sigma_{\rm fit}$ [9].

2. The errors transferred from the errors on the estimation of r_1, r_2, r_3. In fact, due to the finite fully simulated Monte Carlo samples, the r_1, r_2, r_3 values obtained with Eq. (5.20) have statistical errors and this may be transferred to the final fit parameters. The effect can be estimated using the following method: first, a group of r_1, r_2, r_3 are generated according to the error matrix in Table 5.2 and these generated r_1, r_2, r_3 are used to obtain the fit results which are then filled into the histograms as shown in Figure 5.11. The results in the graph are for $p_T \in$ [3,4] GeV/c, $\eta \in$ [4,4.5]. The σ of the histograms are the errors induced by the statistical errors of r_1, r_2, r_3. The errors for the 28 bins are listed in Table 5.8 and Table 5.9 for α_{p1} and α_{b1} respectively.

3. Systematic errors from incorrect efficiency shapes: since the fully simulated sample may have lots of difference with respect to real data, the efficiencies given by the Monte Carlo do not totally agree with real

[9] For the real data analysis, more precise studies should be performed for each bin to obtain the correct factors.

Table 5.8: The errors induced by r_1, r_2, r_3 for α_{p1} in different bins.

p_T (GeV/c)	$\eta \in [3-3.5]$	$\eta \in [3.5-4]$	$\eta \in [4-4.5]$	$\eta \in [4.5-5]$
$0-1$ (GeV/c)	0.68	0.10	0.04	0.03
$1-2$ (GeV/c)	0.05	0.02	0.02	0.02
$2-3$ (GeV/c)	0.03	0.03	0.02	0.04
$3-4$ (GeV/c)	0.05	0.04	0.06	0.08
$4-5$ (GeV/c)	0.06	0.07	0.06	0.36
$5-6$ (GeV/c)	0.07	0.10	0.14	0.48
$6-7$ (GeV/c)	0.11	0.17	0.19	0.70

Table 5.9: The errors induced by r_1, r_2, r_3 on α_{b1} in different bins.

p_T (GeV/c)	$\eta \in [3-3.5]$	$\eta \in [3.5-4]$	$\eta \in [4-4.5]$	$\eta \in [4.5-5]$
$0-1$ (GeV/c)	1.10	0.15	0.04	0.03
$1-2$ (GeV/c)	0.06	0.02	0.02	0.02
$2-3$ (GeV/c)	0.03	0.03	0.02	0.05
$3-4$ (GeV/c)	0.05	0.04	0.05	0.07
$4-5$ (GeV/c)	0.06	0.06	0.06	0.17
$5-6$ (GeV/c)	0.08	0.13	0.19	0.49
$6-7$ (GeV/c)	0.11	0.12	0.21	2.45

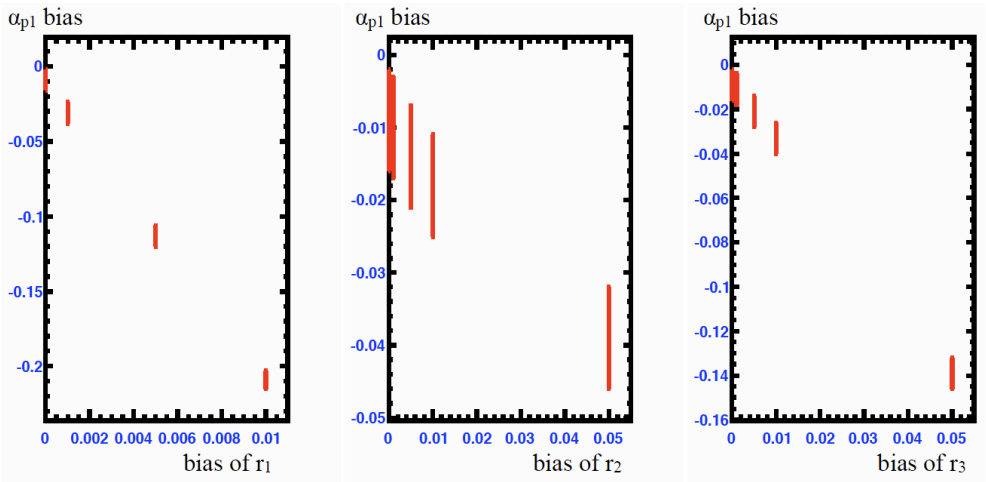

Figure 5.12: The effect on the α_{p1} fit results caused by the bias of r_1, r_2, r_3.

Table 5.10: The final results for the polarization parameter α_{p1} (input value $\alpha_{p1} = 0$).

p_T (GeV/c)	$\eta \in [3 - 3.5]$	$\eta \in [3.5 - 4]$	$\eta \in [4 - 4.5]$	$\eta \in [4.5 - 5]$
$0 - 1$ (GeV/c)	-0.24 ± 1.24	-0.09 ± 0.18	0.04 ± 0.09	0.00 ± 0.07
$1 - 2$ (GeV/c)	-0.02 ± 0.09	-0.01 ± 0.06	0.00 ± 0.06	0.01 ± 0.06
$2 - 3$ (GeV/c)	0.02 ± 0.07	-0.00 ± 0.06	0.00 ± 0.06	-0.01 ± 0.08
$3 - 4$ (GeV/c)	0.01 ± 0.09	-0.02 ± 0.08	0.05 ± 0.10	0.07 ± 0.17
$4 - 5$ (GeV/c)	-0.04 ± 0.11	0.03 ± 0.12	-0.03 ± 0.14	0.30 ± 0.59
$5 - 6$ (GeV/c)	-0.12 ± 0.16	-0.14 ± 0.17	-0.16 ± 0.23	0.10 ± 0.78
$6 - 7$ (GeV/c)	-0.03 ± 0.24	0.44 ± 0.33	0.03 ± 0.38	0.05 ± 1.18

Table 5.11: The final results for the polarization parameter α_{b1} (input value $\alpha_{b1} = 0$).

p_T (GeV/c)	$\eta \in [3 - 3.5]$	$\eta \in [3.5 - 4]$	$\eta \in [4 - 4.5]$	$\eta \in [4.5 - 5]$
$0 - 1$ (GeV/c)	3.35 ± 5.81	1.94 ± 0.92	0.06 ± 0.31	0.08 ± 0.22
$1 - 2$ (GeV/c)	0.43 ± 0.32	-0.07 ± 0.14	-0.07 ± 0.12	-0.18 ± 0.13
$2 - 3$ (GeV/c)	0.14 ± 0.16	0.17 ± 0.13	-0.03 ± 0.13	0.28 ± 0.23
$3 - 4$ (GeV/c)	0.00 ± 0.14	0.15 ± 0.14	-0.22 ± 0.14	-0.04 ± 0.33
$4 - 5$ (GeV/c)	0.05 ± 0.15	-0.05 ± 0.15	0.06 ± 0.20	-0.22 ± 0.41
$5 - 6$ (GeV/c)	0.12 ± 0.18	0.23 ± 0.23	0.26 ± 0.34	-0.42 ± 1.00
$6 - 7$ (GeV/c)	0.01 ± 0.21	-0.24 ± 0.23	0.12 ± 0.38	-0.12 ± 2.78

data. The effects are shown on the calculated r_1, r_2, r_3 from the fully simulated sample. A proper method is then needed to control the computation of r_1, r_2, r_3 using the events from real data and the possible biases induced should be considered. The effect of the bias is studied by giving the r_1, r_2, r_3 values a bias. As the effect on α_{p1} is larger than on the other polarization parameters, only the results for it are shown in Figure 5.12. From the graph, we can see that in order to obtain a precision of 0.01 for α_{p1}, the estimation for r_1, r_2, r_3 should be better than 0.001, 0.01, 0.01 respectively.

In the real analysis, we can use the decay channel $B^+ \to J/\psi K^+$ to check the obtained r_1, r_2, r_3 values as the J/ψ polarization in this decay is well known. The production of $B^+ \to J/\psi K^+$ is around 1/3000 of the J/ψ production, for 5 pb^{-1} of data at $\sqrt{s} = 14$ TeV, it is expected to reconstruct around 2000 $B^+ \to J/\psi K^+$. The r_1, r_2, r_3 are then checked in the full phase space region instead of in each bin due to the lack of statistics. The comparison will be done after weighting the phase space of the two J/ψ samples to be the same. With the above 2000 J/ψ from $B^+ \to J/\psi K^+$, the errors for r_1 are around 0.004 while for the r_2 and r_3, they are around 0.008. Thus the systematic errors due to the efficiency estimation are around 0,05 for α_{p1}.

The final errors for the measurement can be written as

$$\sigma = \sqrt{1.21\sigma^2_{\text{fit}} + \sigma^2_{\text{sta}} + \sigma^2_{\text{bias}}}, \tag{5.29}$$

where σ_{fit} is the error from the fit, σ_{sta} is the error caused by the finite fully simulated sample and σ_{bias} is the error due to the incorrect description of the efficiency shape. Table 5.10 and Table 5.11 list the results for α_{p1} and α_{b1} in all the phase space regions.

5.7 Conclusion

In this chapter, the strategy for the J/ψ polarization measurement using $J/\psi \to \mu^+\mu^-$ channel is given. The analysis is performed in the full angular space in the helicity frame by a 3-D fit over t_z, cosθ and ϕ in 28 p_T and η bins. In order to avoid generating huge amount of Monte Carlo samples to obtain the efficiencies in each bin, a new method on the fit is applied to

summarize the efficiency shape into three constant parameters. All the errors from the efficiency function can be estimated by considering their effects on the three parameters. Based on the three parameters estimated from the same Monte Carlo data of 0.79 pb^{-1}, errors on the polarization parameters for the majority of the bins are determined to be around 0.1 for the prompt J/ψ and around 0.2 for the J/ψ from b decays.

Chapter 6

J/ψ Analysis Status in LHCb

In this chapter, we give a brief summary of the experimental status for the J/ψ differential cross section measurement performed by the LHCb J/ψ working group until the end of May. The amount of data used is around 14 nb^{-1} with both polarities of the magnetic field [1]. First the selection criteria are chosen for the real data according to the studies with Monte Carlo sample in Chapter 4 and according to the current understanding of the detector. The number of J/ψ is then obtained for each p_T bin from a mass fit. The differential cross section of J/ψ production is then given after correction using the efficiency from the tuned Monte Carlo.

The analysis in Chapter 4 is based on the Monte Carlo sample generated in 2006. As more and more data are collected, the Monte Carlo simulation improves a lot to reproduce the current detector response. In the following analysis, the Monte Carlo sample used to be compared with the real data is the tuned Monte Carlo generated in 2009 and 2010. Due to the lack of understanding of the detector like the alignment, the selection criteria optimized in Chapter 4 using the DC06 minimum bias sample generated at $\sqrt{s} = 14$ TeV are not suitable. Looser selection criteria based on the selection criteria discussed in Chapter 4 are applied on the real data.

The J/ψ candidates are reconstructed with two long tracks identified as IsMuon (StdLooseMuon, see Chapter 4) as in the Monte Carlo study. The two tracks that form J/ψ candidate are required to have different charges.

[1] Nearly half of the data collected in April and May is with the magnetic field pointing upwards and half is with the magnetic field pointing downwards.

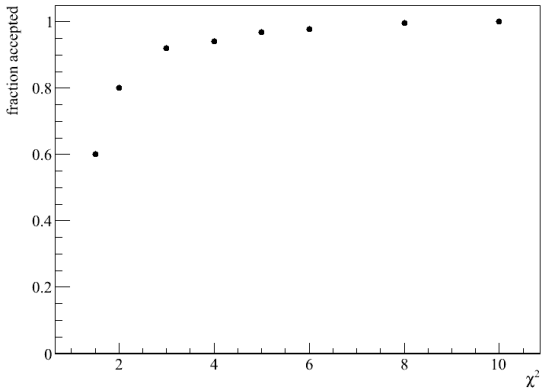

Figure 6.1: The efficiency of J/ψ signal events as a function of track quality:χ^2/nDoF.

The transverse momentum of each muon candidate is required to be larger than 0.7 GeV/c. But due to the not so good alignment between different sub-detectors, a looser requirement on the track fit quality is set. Figure 6.1 shows the efficiency of J/ψ signal events as a function of χ^2/nDoF. We can see that if we still choose the selection criteria which requires the χ^2/nDoF to be less than 2, the efficiency is only around 60%. A requirement of χ^2/nDoF to be less than 4 is then chosen with a higher efficiency around 90% while the S/B drops little.

In the Monte Carlo study, the combined DLL between the muon and pion hypothesis is required to be larger than -1 to reduce misidentified pions and kaons. For the current data, this information is not yet avaible due to the lack of statistics to calibrate the DLL function and it is not used in the selection. One has to note that the muon identification works very well in LHCb. Figure 6.2 shows the misidentification rate for π to μ and the efficiency of μ as a function of momentum (p) and their comparison with the Monte Carlo results using a reconstructed K_S sample. The results from real data are marked with red color. From the plot, we can see that the two agree very well.

The J/ψ vertex is then reconstructed with the muon candidates passing the above selection criteria and a selection on the vertex fit quality is required to reduce possible combinational background. The comparison of the Monte Carlo results (yellow filled area) and the real data results (black data points) for the vertex fit quality is shown in Figure 6.3 where $p(\chi^2)$ gives

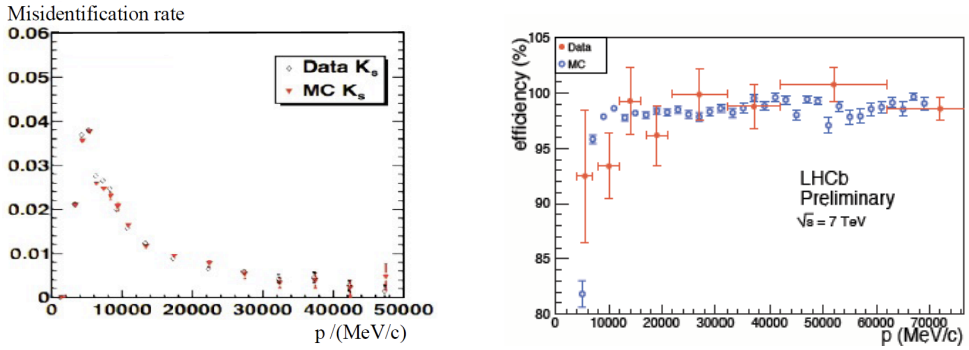

Figure 6.2: The misidentification rate of π to μ (left) and the identification efficiency of μ (right) and its comparison with the Monte Carlo results using a K_S sample. The results from real data are marked with red color.

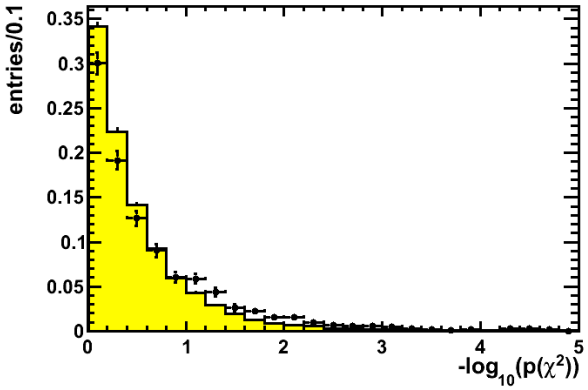

Figure 6.3: The comparison of the Monte Carlo results (yellow filled area) and the real data results (black data points) for the vertex quality.

the probability of a vertex fit χ^2 to be larger than the measured value with the nDoF of the J/ψ vertex fit to be 1. From the figure, we can see that the vertex quality from real data has worse quality (χ^2). A looser selection criterion is chosen. Figure 6.4 shows the efficiencies and S/B as a function of $-\log_{10}p(\chi^2)$. The red points in the left plot represent the Monte Carlo results while the black ones represent the real data results. We can see that the vertex quality cut improves little on the S/B. This is the same as in the Monte Carlo results shown in Chapter 4. We can also see that a tighter cut as before ($p(\chi^2) > 0.01$ for Monte Carlo in Chapter 4) may result in an efficiency around 90%. Thus a looser selection of $p(\chi^2) > 10^{-5}$ is chosen and keeps nearly all the J/ψ candidates.

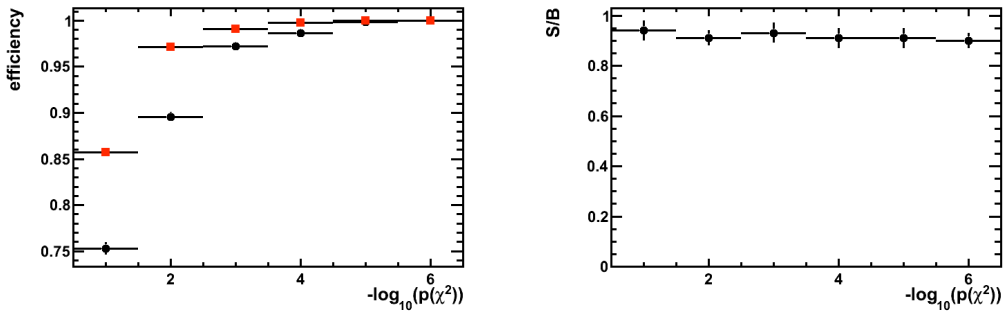

Figure 6.4: The efficiency (left) and S/B (right) as a function of $-\log_{10}p(\chi^2)$. The red points in the left figure represent the Monte Carlo results while the black ones represent the real data results.

Table 6.1: $J/\psi \to \mu^+\mu^-$ selection criteria

Quantity	Cut value
μ	Long track with muon detector
track	hits (StdLooseMuon)
μ: p_T	$> 0.7\,\mathrm{GeV}/c$
μ: track quality χ^2/nDoF	< 4 (2 before)
J/ψ Mass Window	$\pm 0.4\,\mathrm{GeV}/c^2$
J/ψ Vertex χ^2 probability (nDoF=1)	$p(\chi^2) > 10^{-5}$ ($\sim$0.02 before)
Event: Number of primary vertices	> 0
Event: Multi-J/ψ	Clone selection criteria (see Chapter 4)

Besides the above selection criteria, two extra selections are added to require at least one reconstructed primary vertex and to kill the clone candidates as discussed in Chapter 4. The whole selection criteria used are then listed in Table 6.1.

The di-muon invariant mass distributions with the above selection criteria is shown in Figure 6.5. As discussed in Chapter 4, a Crystal Ball function is used to fit the J/ψ signal while a linear function is used to fit the background. The obtained resolution of J/ψ mass distribution is 15.8 ± 0.4 MeV/c^2 with $S/B \sim 1$. The low S/B ratio is due to several reasons. First, the detector is not yet well aligned and the track quality is poor which reduces the discriminating power against ghost tracks. Moreover only part of the Muon detector information is used (StdLooseMuon without further DLL information). As discussed in Chapter 4, most of the tracks misidentified as muons

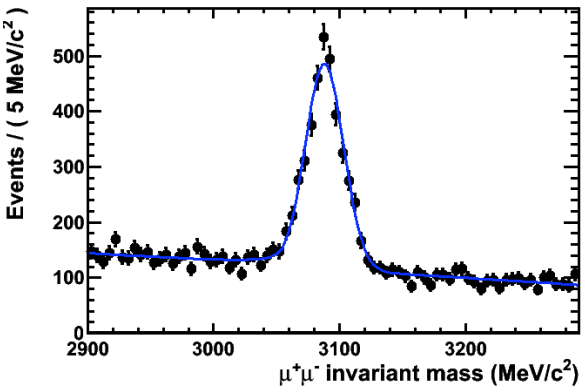

Figure 6.5: The di-muon invariant mass distribution.

are π and K that decay into muons and since no further information from other sub-detectors is used, the muon sample is less clean than the one used in the Monte Carlo study. It is also observed that track multiplicity is larger in data than Monte Carlo which makes the situation even worse. Another reason is due to relatively low J/ψ production compared to the Monte Carlo sample. With better understanding of the LHCb detector, the S/B ratio will certainly increase. The number of J/ψ reconstructed with the above selection criteria is $2,946 \pm 98$. This is not enough to be divided into p_T and y [2] bins and we only measure the cross section as a function of p_T and without distinguishing the prompt and displaced components. With more data, this will be certainly done. In fact the t_z variable defined in Chapter 4 is also reconstructed as shown in Figure 6.6. The green filled region shows the background contribution from sidebands. A clear contribution from the b component can be seen in the positive region.

Table 6.2 lists the fitted number of signal J/ψ in different p_T bins using the mass function above, together with the mass resolution in each bin.

As discussed in Chapter 4, the efficiency in LHCb is divided into three parts: acceptance efficiency (ϵ_{acc}), reconstruction efficiency (ϵ_{rec}) and trigger efficiency ($\epsilon_{\text{trigger}}$). They are currently obtained from Monte Carlo sample generated at $\sqrt{s} = 7$ TeV and the results are listed in Table 6.3. For the trigger efficiency, the current triggers applied on the J/ψ sample are L0 SingleMuon trigger and HLT1 trigger which confirms the L0 SingleMuon trigger.

[2]For the real data analysis, the study will be performed in y bins instead of η bins.

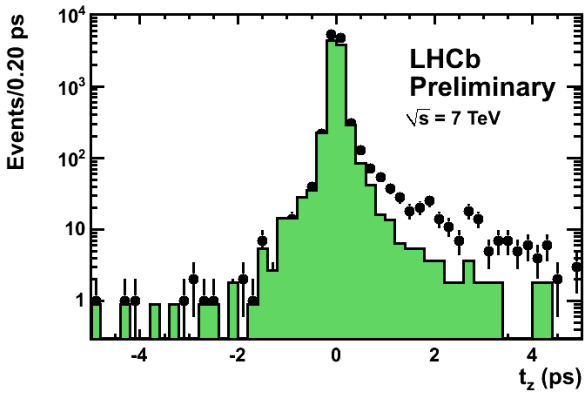

Figure 6.6: t_z distribution in data, for the J/ψ signal region (black points) and for the J/ψ mass sidebands (green histogram)

Table 6.2: The number of fitted J/ψ signal events in different p_T bins together with their mass resolutions.

p_T (GeV/c)	total	$0-1$	$1-2$	$2-3$	$3-4$
Signal numbers	2946 ± 98	507 ± 51	833 ± 55	740 ± 55	387 ± 23
Mass resolution	15.2 ± 0.4	12.6 ± 1.1	13.3 ± 0.7	16.2 ± 0.9	$15.6 \pm 1.$
p_T (GeV/c)	$4-5$	$5-6$	$6-7$	$7-8$	$8-9$
Signal numbers	251 ± 17	149 ± 13	69 ± 10	35 ± 6	25 ± 5
Mass resolution	17.3 ± 1.2	16.6 ± 1.2	18.9 ± 2.9	26.3 ± 3.7	17.8 ± 2.7

Table 6.3: Different efficiencies of J/ψ from Monte Carlo.

p_T (GeV/c)	$0-1$	$1-2$	$2-3$	$3-4$	$4-5$
$\epsilon_{\rm acc}$	0.88 ± 0.01	0.88 ± 0.01	0.91 ± 0.01	0.93 ± 0.01	0.95 ± 0.01
$\epsilon_{\rm rec}$	0.64 ± 0.01	0.61 ± 0.01	0.59 ± 0.01	0.58 ± 0.01	0.62 ± 0.01
$\epsilon_{\rm trigger}$	0.79 ± 0.01	0.83 ± 0.01	0.87 ± 0.01	0.90 ± 0.01	0.93 ± 0.01
$\epsilon_{\rm tot}$	0.44 ± 0.01	0.45 ± 0.01	0.47 ± 0.01	0.49 ± 0.01	0.55 ± 0.01
p_T (GeV/c)	$5-6$	$6-7$	$7-8$	$8-9$	
$\epsilon_{\rm acc}$	0.96 ± 0.01	0.97 ± 0.01	0.98 ± 0.01	0.98 ± 0.01	
$\epsilon_{\rm rec}$	0.67 ± 0.01	0.70 ± 0.01	0.73 ± 0.01	0.75 ± 0.01	
$\epsilon_{\rm trigger}$	0.94 ± 0.01	0.95 ± 0.01	0.96 ± 0.01	0.97 ± 0.01	
$\epsilon_{\rm tot}$	0.60 ± 0.01	0.65 ± 0.01	0.69 ± 0.01	0.71 ± 0.01	

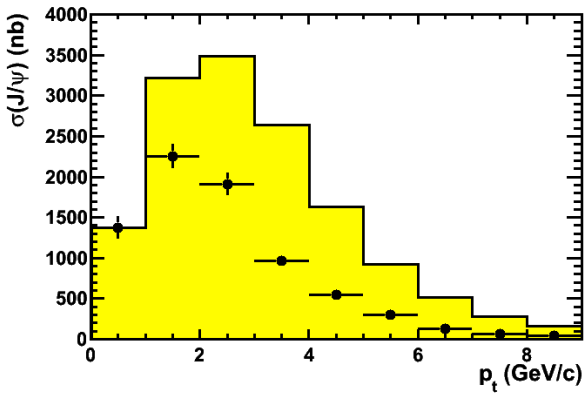

Figure 6.7: The J/ψ differential cross section and its comparison with Monte Carlo generated at $\sqrt{s} = 7$ TeV. Only statistical errors are included.

According to Table 6.2 and Table 6.3, the differential cross section is then calculated as shown in Figure 6.7 where the errors are statistical errors only. The luminosity is set to be 14 nb^{-1} during the calculation. The Monte Carlo differential cross section generated at $\sqrt{s} = 7$ TeV with color octet model implemented is also shown as a comparison (yellow filled area) and we can see that the real data has a harder spectrum than the Monte Carlo. The total cross section in the region $p_T \in [0, 9]$ GeV/c and $y \in [2.5, 4]$ is 7.6 ± 0.3 μb while the Monte Carlo value is 14.2 μb.

$$\sigma\,(\text{inclusive J}/\psi,\, p_T(J/\psi) < 9\,\text{GeV}/c,\, 2.5 < y < 4) \;=\; 7.6 \pm 0.3\,\mu\text{b}$$

To conclude, the J/ψ differential cross section measurement now progresses very well in LHCb. But due to the lack of statistics, the full analysis is not yet performed and the study will be improved with more data.

Conclusion

The LHC has been running at $\sqrt{s} = 7$ TeV for two months since its first collision at this center-of-mass energy on March 30th. The LHCb experiment has already collected around 14 nb^{-1} of collision data during this period and lots of particles like K_S, J/ψ, $\Upsilon(1S)$, *etc* have been re-discovered one by one. With this amount of data, around 3000 J/ψ signal events have been reconstructed, and the analysis on J/ψ production has started. But the data is not yet enough for a full analysis of the differential cross section and polarization measurements. It is foreseen that with further running in the following months, LHCb will collect enough J/ψ events for these meaurements. In this thesis, we give the strategy for the above measurements using Monte Carlo data together with some preliminary results from real data.

At the beginning of this thesis, a simple review of the J/ψ (also b-hadron) production mechanism and its comparison with experimental results are given: though currently NRQCD describes the measured p_T spectrum of J/ψ from CDF very well, none of the theories describe the polarization correctly. Even for the explanation of differential cross section spectrum, the contributions of different components are not clear especially after higher-order CSM terms are calculated which shows that the COM terms may contribute less than expected before. Thus new measurements at a higher energy and in a new phase space region are needed for further understanding of the underlying mechanism. LHCb offers a perfect environment for such a study. As one of four detector experiments at LHC, it offers huge amount of J/ψ for the research on the differential cross section and polarization measurements and its unique acceptance amongst the four experiments offers information which can not be reached by other experiments. As an experiment dedicated to the b physics, all the sub-detectors of LHCb are optimized for b physics and are also suitable for precise measurements in charm physics.

The strategies of the differential cross section and polarization measurements are given using Monte Carlo data. First the J/ψ selection criteria are optimized using the minimum bias sample and the di-muon invariant mass spectrum with a clear J/ψ mass peak is obtained, we found that the mass resolution of J/ψ is around 11 MeV/c^2 and the S/B within the $\pm 3\sigma$ mass region is around 18. According to the fit number, it is expected that 250 J/ψ are reconstructed every second at $\sqrt{s} = 14$ TeV during LHCb nominal running, that is 6.5×10^6 J/ψ per pb^{-1} of data. The phase space region focused is set to be $p_T \in [0, 7]$ GeV/c, $\eta \in [3, 5]$ according to the reconstructed J/ψ $p_T - \eta$ distribution. In order to reduce the dependence on the phase space, the above region is further divided into 28 bins with a width of 1 GeV/c in p_T and a width of 0.5 in η. The J/ψ cross section and polarization measurements are performed in each of the 28 bins.

There are three main sources for the J/ψ production: direct J/ψ production, J/ψ from excited charmonium states and J/ψ from b-hadrons. In order to understand the J/ψ production mechanism, the contributions of different components are needed to be distinguished. In this thesis, we only distinguish the prompt component (the first two sources) and the J/ψ from b-component by our defined time variable t_z. From the reconstructed t_z shape, we found there is an unexpected tail distribution due to primary vertices which fail to be reconstructed. The tail distribution may affect a lot our measurements and a method is developed to obtain its distribution from real data. After understanding the different components in the t_z distribution, a combined fit of mass and t_z is performed to obtain the number of prompt J/ψ and J/ψ from b-hadrons. The efficiency to obtain the absolute cross section of J/ψ is then calculated. In LHCb, it is divided into three parts: acceptance efficiency, reconstruction efficiency and trigger efficiency. For current measurements, they are obtained from Monte Carlo. After being corrected by the efficiency, the differential cross sections are obtained and they agree very well with the Monte Carlo input values. The research shows that the statistical errors in nearly all the 28 bins are less than 10% with 0.79 pb^{-1} of data (with 5 pb^{-1} of data at $\sqrt{s} = 14$ TeV, the statistical errors for both prompt and delayed components are less than 10% for all the bins). The systematic errors of the experiment can also be controlled at this level. During the analysis, we found that the polarization of J/ψ may affect a lot the differential cross section measurement as different polarization scenarios may have different efficiencies. For some bins of the above phase space region, the difference be-

tween the efficiencies of the fully polarized sample and un-polarized sample can be larger than 30%. Thus a measurement of the polarization is needed to obtain a better precision for the J/ψ differential cross section measurement.

The polarization measurement in LHCb will be done in at least two reference frames and in the full angular space region. In this thesis, only the measurement in the helicity reference frame is done and it should be similar for the other reference frames. In order to perform the analysis, the efficiency as a function of $\cos\theta$ and ϕ in different phase space regions are needed and a huge amount of simulated data is needed for the efficiency estimation. This is very hard to realize in reality and a simplified method using the maximum log-likehood method is then developed to summarize the 2-D efficiencies into 3 parameters: r_1, r_2, r_3. The r_1, r_2, r_3 values are obtained from Monte Carlo but it could be checked using the J/ψ from $B^+ \to J/\psi K^+$ during the real data analysis. As all the errors related with the efficiency may reflect on these three parameters, the error estimation for the polarization measurement becomes simpler. To measure the polarization parameters of the prompt and delayed components, a 3-D fit is then performed over $t_z, \cos\theta, \phi$ with a weight function of m. According to analysis with 0.79 pb^{-1} of data, the errors for most of the bins are around 0.1 for the prompt J/ψ and 0.2 for the J/ψ from b-hadrons.

As LHCb already collected around 14 nb^{-1} of data, part of the study on the J/ψ could already be performed using real data. The J/ψ mass spectrum is reconstructed with looser selection criteria due to the lack of the understanding of the detector. The mass resolution is about 16 MeV/c^2 with the S/B ratio around 1. The measurement of the J/ψ differential cross section is performed only as a function of p_T and the J/ψ from b component is not distinguished from the prompt component due to the lack of statistics. The efficiencies used are obtained from Monte Carlo samples. The measured cross section in the region $p_T \in [0, 9]$ GeV/c and $y \in [2.5, 4]$ is 7.6 ± 0.3 μb (statistical error only) with a harder spectrum than Monte Carlo.

In the thesis, only the prompt component and the J/ψ from b component are distinguished. Based on the above study, further distinction between the direct production and the production from excited charmonium states can also be studied. Further on, in order to understand the contribution of different terms, the measurements with extra variables can also be performed to include the effect of the associated J/ψ products (like $J/\psi + J/\psi$, $J/\psi +$

$\gamma \cdots$). It is foreseen that until the end of this year, LHCb will offer a fully analyzed results on the differential cross section, polarization and other J/ψ measurements for the production mechanism study.

Bibliography

[1] The Large Hadron Collider: Conceptual Design. CERN-AC-95-05-LHC.

[2] Armstrong W W, *et al.* ATLAS: Technical Proposal for a General Purpose *pp* Experiment at the Large Hadron Collider at CERN. CERN-LHCC-94-43.

[3] CMS, the Compact Muon Solenoid: Technical proposal. CERN-LHCC-94-38.

[4] ALICE: Technical Proposal for a Large Ion Collider Experiment at the CERN LHC. CERN-LHCC-95-71.

[5] Amato S, *et al.* LHCb Technical Proposal. CERN-LHCC-98-04.

[6] Augustin J E, *et al.* Discovery of a Narrow Resonance in e^+e^- Annihilation. Phys. Rev. Lett., 1974, 33:1406–1408.

[7] Aubert J J, *et al.* Experimental Observation of a Heavy Particle J. Phys. Rev. Lett., 1974, 33:1404–1406.

[8] Herb S W, *et al.* Observation of a Dimuon Resonance at 9.5 GeV in 400 GeV Proton-Nucleus Collisions. Phys. Rev. Lett., 1977, 39:252–255.

[9] Cacciari M, Frixione S, Mangano M L, *et al.* QCD Analysis of First b Cross-Section Data at 1.96 TeV. JHEP, 2004, 07:033.

[10] Acosta D E, *et al.* Measurement of the J/ψ Meson and b-Hadron Production Cross Sections in $p\bar{p}$ Collisions at $\sqrt{s} = 1960$ GeV. Phys. Rev., 2005, D71:032001.

[11] Abulencia A, *et al.* Measurement of the B^+ Production Cross Section in $p\bar{p}$ Collisions at $\sqrt{s} = 1960$ GeV. Phys. Rev., 2007, D75:012010.

[12] Aaltonen T, *et al.* Measurement of the b-Hadron Production Cross Section Using Decays to $\mu^- D^0 X$ Final States in $p\bar{p}$ Collisions at $\sqrt{s} =$ 1.96 TeV. Phys. Rev., 2009, D79:092003.

[13] Mangano M L. The Saga of Bottom Production in $p\bar{p}$ Collisions. AIP Conf. Proc., 2005, 753:247–260.

[14] Abe F, *et al.* Production of J/ψ Mesons from χ_c Meson Decays in $p\bar{p}$ Collisions at $\sqrt{s} = 1.8$ TeV. Phys. Rev. Lett., 1997, 79:578–583.

[15] Abe F, *et al.* J/ψ and $\psi(2S)$ Production in $p\bar{p}$ Collisions at $\sqrt{s} = 1.8$ TeV. Phys. Rev. Lett., 1997, 79:572–577.

[16] Cacciari M, Greco M. J/ψ Production via Fragmentation at the Tevatron. Phys. Rev. Lett., 1994, 73:1586–1589.

[17] Cho P L, Wise M B. Spin Symmetry Predictions for Heavy Quarkonia Alignment. Phys. Lett., 1995, B346:129–136.

[18] Braaten E, Fleming S. Color Octet Fragmentation and the ψ' Surplus at the Tevatron. Phys. Rev. Lett., 1995, 74:3327–3330.

[19] Cacciari M, Greco M, Mangano M L, *et al.* Charmonium Production at the Tevatron. Phys. Lett., 1995, B356:553–560.

[20] Cho P L, Leibovich A K. Color Octet Quarkonia Production. Phys. Rev., 1996, D53:150–162.

[21] Cho P L, Leibovich A K. Color Octet Quarkonia Production II. Phys. Rev., 1996, D53:6203–6217.

[22] Beneke M, Rothstein I Z. ψ' Polarization as a Test of Colour Octet Quarkonium Production. Phys. Lett., 1996, B372:157–164.

[23] Braaten E, Kniehl B A, Lee J. Polarization of Prompt J/ψ at the Tevatron. Phys. Rev., 2000, D62:094005.

[24] Vanttinen M, Hoyer P, Brodsky S J, *et al.* Hadroproduction and Polarization of Charmonium. Phys. Rev., 1995, D51:3332–3339.

[25] Beneke M. Nonrelativistic Effective Theory for Quarkonium Production in Hadron Collisions. arXiv:hep-ph/9703429.

[26] Baranov S P. Highlights from the k_T Factorization Approach on the Quarkonium Production Puzzles. Phys. Rev., 2002, D66:114003.

[27] Abulencia A, *et al.* Polarization of J/ψ and $\psi(2S)$ Mesons Produced in $p\bar{p}$ Collisions at $\sqrt{s} = 1.96$ TeV. Phys. Rev. Lett., 2007, 99:132001.

[28] Bjorken J D, Glashow S L. Elementary Particles and SU(4). Phys. Lett., 1964, 11:255–257.

[29] Glashow S L, Iliopoulos J, Maiani L. Weak Interactions with Lepton-Hadron Symmetry. Phys. Rev., 1970, D2:1285–1292.

[30] Richter B. $e^+e^- \rightarrow$ Hadrons. Plenary Session Report at XVII International Conference on High Energy Physics, London, England, Jul 1–10, 1974.

[31] Appelquist T, De Rujula A, Politzer H D, *et al.* Charmonium Spectroscopy. Phys. Rev. Lett., 1975, 34:365.

[32] Brambilla N, *et al.* Heavy Quarkonium Physics. arXiv:hep-ph/0412158.

[33] Amsler C, *et al.* Review of Particle Physics. Phys. Lett., 2008, B667:1.

[34] Abe F, *et al.* The CDF Detector: an Overview. Nucl. Instr. Meth., 1988, A271:387–403.

[35] Blair R, *et al.* The CDF-II Detector: Technical Design Report. FERMILAB-PUB-96-390-E.

[36] Collins J C, Soper D E, Sterman G. Factorization of Hard Processes in QCD. Adv. Ser. Direct. High Energy Phys., 1988, 5:1.

[37] Bodwin G T. Factorization of The Drell-Yan Cross-Section in Perturbation Theory. Phys. Rev., 1985, D31:2616.

[38] Qiu J W, Sterman G. Power Corrections in Hadronic Scattering. 1. Leading $1/Q^2$ Corrections to the Drell-Yan Cross-Section. Nucl. Phys., 1991, B353:105–136.

[39] Qiu J W, Sterman G. Power Corrections to Hadronic Scattering. 2. Factorization. Nucl. Phys., 1991, B353:137–164.

[40] Gribov V N, Lipatov L N. Deep Inelastic *ep* Scattering in Perturbation Theory. Sov. J. Nucl. Phys., 1972, 15:438–450.

[41] Altarelli G, Parisi G. Asymptotic Freedom in Parton Language. Nucl. Phys., 1977, B126:298.

[42] Dokshitzer Y L. Calculation of the Structure Functions for Deep Inelastic Scattering and e^+e^- Annihilation by Perturbation Theory in Quantum Chromodynamics. Sov. Phys. JETP, 1977, 46:641–653.

[43] Fritzsch H. Producing Heavy Quark Flavors in Hadronic Collisions: A Test of Quantum Chromodynamics. Phys. Lett., 1977, B67:217.

[44] Halzen F. CVC for Gluons and Hadroproduction of Quark Flavors. Phys. Lett., 1977, B69:105.

[45] Gluck M, Owens J F, Reya E. Gluon Contribution to Hadronic J/ψ Production. Phys. Rev., 1978, D17:2324.

[46] Barger V D, Keung W Y, Phillips R J N. On ψ and Υ Production via Gluons. Phys. Lett., 1980, B91:253.

[47] Amundson J F, Eboli O J P, Gregores E M, *et al.* Colorless States in Perturbative QCD: Charmonium and Rapidity Gaps. Phys. Lett., 1996, B372:127–132.

[48] Amundson J F, Eboli O J P, Gregores E M, *et al.* Quantitative Tests of Color Evaporation: Charmonium Production. Phys. Lett., 1997, B390:323–328.

[49] Einhorn M B, Ellis S D. Hadronic Production of the New Resonances: Probing Gluon Distributions. Phys. Rev., 1975, D12:2007.

[50] Ellis S D, Einhorn M B, Quigg C. Comment on Hadronic Production of Psions. Phys. Rev. Lett., 1976, 36:1263.

[51] Carlson C E, Suaya R. Hadronic Production of ψ/J Mesons. Phys. Rev., 1976, D14:3115.

[52] Chang C H. Hadronic Production of J/ψ Associated with a Gluon. Nucl. Phys., 1980, B172:425–434.

[53] Berger E L, Jones D L. Inelastic Photoproduction of J/ψ and Υ by Gluons. Phys. Rev., 1981, D23:1521–1530.

[54] Baier R, Ruckl R. Hadronic Production of J/ψ and Υ: Transverse Momentum Distributions. Phys. Lett., 1981, B102:364.

[55] Baier R, Ruckl R. On Inelastic Leptoproduction of Heavy Quarkonium States. Nucl. Phys., 1982, B201:1.

[56] Baier R, Ruckl R. Hadronic Collisions: A Quarkonium Factory. Z. Phys., 1983, C19:251.

[57] Artoisenet P, Lansberg J P, Maltoni F. Hadroproduction of J/ψ and Υ in Association with a Heavy Quark Pair. Phys. Lett., 2007, B653:60–66.

[58] Halzen F, Herzog F, Glover E W N, *et al.* The J/ψ as a Trigger in $p\bar{p}$ Collisions. Phys. Rev., 1984, D30:700.

[59] Glover E W N, Martin A D, Stirling W J. J/ψ Production at Large Transverse Momentum at Hadron Colliders. Z. Phys., 1988, C38:473.

[60] Albajar C, *et al.* J/ψ and ψ' Production at the CERN $p\bar{p}$ Collider. Phys. Lett., 1991, B256:112–120.

[61] Abe F, Amidei D, Anway-Wiese C, *et al.* Inclusive J/ψ, $\psi(2S)$, and b-quark production in $p\bar{p}$ collisions at $\sqrt{s}$ =1.8 TeV. Phys. Rev. Lett., 1992, 69(26):3704–3708.

[62] Kramer M. Quarkonium Production at High-Energy Colliders. Prog. Part. Nucl. Phys., 2001, 47:141–201.

[63] Braaten E, Doncheski M A, Fleming S, *et al.* Fragmentation Production of J/ψ and ψ' at the Tevatron. Phys. Lett., 1994, B333:548–554.

[64] Zhang Y J, Gao Y J, Chao K T. Next-to-leading Order QCD Correction to $e^+e^- \to J/\psi + \eta_c$ at $\sqrt{s} = 10.6$ GeV. Phys. Rev. Lett., 2006, 96:092001.

[65] Artoisenet P, Campbell J M, Lansberg J P, *et al.* Υ Production at Fermilab Tevatron and LHC Energies. Phys. Rev. Lett., 2008, 101:152001.

[66] Campbell J M, Maltoni F, Tramontano F. QCD corrections to J/ψ and Υ production at hadron colliders. Phys. Rev. Lett., 2007, 98:252002.

[67] Bodwin G T, Braaten E, LePAGE G P. Rigorous QCD Predictions for Decays of P Wave Quarkonia. Phys. Rev., 1992, D46:1914–1918.

[68] Bodwin G T, Braaten E, Lepage G P. Rigorous QCD analysis of inclusive annihilation and production of heavy quarkonium. Phys. Rev., 1995, D51:1125–1171.

[69] Caswell W E, Lepage G P. Effective Lagrangians for Bound State Problems in QED, QCD, and Other Field Theories. Phys. Lett., 1986, B167:437.

[70] Gong B, Li X Q, Wang J X. QCD Corrections to J/ψ Production via Color Octet States at Tevatron and LHC. Phys. Lett., 2009, B673:197–200.

[71] Lansberg J P. On the Mechanisms of Heavy-Quarkonium Hadroproduction. Eur. Phys. J., 2009, C61:693–703.

[72] Boer W, Sander C. Global Electroweak Fits and Gauge Coupling Unification. Phys. Lett., 2004, B585:276–286.

[73] Maltoni F, *et al.* Analysis of Charmonium Production at Fixed-Target Experiments in the NRQCD Approach. Phys. Lett., 2006, B638:202–208.

[74] Braaten E, Chen Y Q. Signature for Color Octet Production of J/ψ in e^+e^- Annihilation. Phys. Rev. Lett., 1996, 76:730–733.

[75] Collins J C, Soper D E. Angular Distribution of Dileptons in High-Energy Hadron Collisions. Phys. Rev., 1977, D16:2219.

[76] Faccioli P, Lourenco C, Seixas J, *et al.* J/ψ Polarization from Fixed-Target to Collider Energies. Phys. Rev. Lett., 2009, 102:151802.

[77] Bardeen W A, Buras A J, Duke D W, *et al.* Deep Inelastic Scattering Beyond the Leading Order in Asymptotically Free Gauge Theories. Phys. Rev., 1978, D18:3998.

[78] Mele B, Nason P. The Fragmentation Function for Heavy Quarks in QCD. Nucl. Phys., 1991, B361:626–644.

[79] Peterson C, Schlatter D, Schmitt I, *et al.* Scaling Violations in Inclusive e^+e^- Annihilation Spectra. Phys. Rev., 1983, D27:105.

[80] Kartvelishvili V G, Likhoded A K, Petrov V A. On the Fragmentation Functions of Heavy Quarks Into Hadrons. Phys. Lett., 1978, B78:615.

[81] Cacciari M, Greco M, Nason P. The p_T Spectrum in Heavy-Flavour Hadroproduction. JHEP, 1998, 05:007.

[82] Bargiotti M, Vagnoni V. Heavy Quarkonia Sector in PYTHIA 6.324: Tuning, Validation and Perspectives at LHC(b). CERN-LHCB-2007-042.

[83] Nason P, *et al.* Bottom Production. arXiv: hep-ph/0003142.

[84] Sjostrand T, Zijl M. A Multiple Interaction Model for the Event Structure in Hadron Collisions. Phys. Rev., 1987, D36:2019.

[85] Kienzle W, Oriunno M, Perrot A L, *et al.* TOTEM, Total Cross Section, Elastic Scattering and Diffraction Dissociation at the LHC: Technical Proposal. Technical Report CERN-LHCC-99-007. LHCC-P-5, CERN, Geneva, Mar, 1999.

[86] Adriani O, Bonechi L, Bongi M, *et al.* Technnical Proposal for the CERN LHCf Experiment: Measurement of Photons and Neutral Pions in the Very Forward Region of LHC. Technical Report CERN-LHCC-2005-032. LHCC-P-007, CERN, Geneva, Sep, 2005. revised version submitted on 2005-10-04 11:34:56.

[87] Schneider O, Nakada T. LHCb trigger. Prepared for 4th International Conference on B Physics and CP Violation (BCP 4), Ago Town, Mie Prefecture, Japan, 19–23 Feb 2001.

[88] Van Tilburg, J and Merk, M. Track Simulation and Reconstruction in LHCb. Amsterdam, 2005, presented on 01 Sep 2005.

[89] LHCb Technical Design Report: Reoptimized Detector Design and Performance. CERN-LHCC-2003-030.

[90] LHCb Magnet: Technical Design Report. CERN-LHCC-2000-007.

[91] LHCb VELO TDR: Vertex Locator. Technical Design Report. CERN-LHCC-2001-011.

[92] Gassner J, Lehner F, Steiner F. The Mechanical Design of the LHCb Silicon Trigger Tracker. CERN-LHCB-2004-110.

[93] Needham M. Silicon Tracker Simulation Performance. LHCb-2003-015.

[94] An Improved Digitization Procedure for the Outer Tracker. LHCb-2001-055.

[95] Forty R. Track Seeding. LHCb-2001-109.

[96] Tilburg J. Matching VELO Tracks with Seeding Tracks. LHCb-2001-103.

[97] Kalman R E. A New Approach to Linear Filtering and Prediction Problems. Transactions of the ASME–JOURNAL of Basic Engineering, 1960, 82(Series D):35–45.

[98] LHCb: RICH Technical Design Report. CERN-LHCC-2000-037.

[99] LHCb Calorimeters: Technical Design Report. CERN-LHCC-2000-036.

[100] LHCb Muon System Technical Design Report. CERN-LHCC-2001-010.

[101] Polycarpo E, Gandelman M. The Performance of the LHCb Muon Identification Procedure. CERN-LHCB-2007-145.

[102] Lanfranchi G, Cid Vidal X, Furcas S, *et al.* The Muon Identification Procedure of the LHCb Experiment for the First Data. Technical Report LHCb-PUB-2009-013. CERN-LHCb-PUB-2009-013, CERN, Geneva, Aug, 2009.

[103] LHCb Trigger System Technical Design Report. CERN-LHCC-2003-031.

[104] Barbosa-Marinho P R, *et al.* LHCb Online System Technical Design Report: Data Acquisition and Experiment Control. CERN-LHCC-2001-040.

[105] Arnault C. http://www.cmtsite.org/.

[106] http://lhcb-release-area.web.cern.ch/LHCb-release-area/DOC/gauss/.

[107] Sjostrand T, Mrenna S, Skands P Z. PYTHIA 6.4 Physics and Manual. JHEP, 2006, 05:026.

[108] Corcella G, *et al.* HERWIG 6.5: an Event Generator for Hadron Emission Reactions With Interfering Gluons (Including Supersymmetric Processes). JHEP, 2001, 01:010.

[109] Chang C H, Wang J X, Wu X G. BCVEGPY2.0: A Upgrade Version of the Generator BCVEGPY with an Addendum about Hadroproduction of the P-wave B_c States. Comput. Phys. Commun., 2006, 174:241–251.

[110] Chang C H, Driouichi C, Eerola P, *et al.* BCVEGPY: An Event Generator for Hadronic Production of the B_c Meson. Comput. Phys. Commun., 2004, 159:192–224.

[111] Ryd A, *et al.* EvtGen: A Monte Carlo Generator for B-Physics. EVTGEN-V00-11-07.

[112] Agostinelli S, *et al.* GEANT4: A Simulation Toolkit. Nucl. Instrum. Meth., 2003, A506:250–303.

[113] http://lhcb-release-area.web.cern.ch/LHCb-release-area/DOC/boole.

[114] http://lhcb-release-area.web.cern.ch/LHCb-release-area/DOC/moore.

[115] http://lhcb-release-area.web.cern.ch/LHCb-release-area/DOC/brunel.

[116] http://lhcb-release-area.web.cern.ch/LHCb-release-area/DOC/davinci.

[117] http://lhcb-release-area.web.cern.ch/LHCb-release-area/DOC/panoramix/.

[118] http://ganga.web.cern.ch/ganga/.

[119] LHCb TDR Computing Technical Design Report. CERN-LHCC-2005-019.

[120] Drees M, Kim C S. Associate $J/\psi + \gamma$ Production: A Clean Probe of Gluon Densities. Z. Phys., 1992, C53:673–678.

[121] Gastmans R, Troost W, Wu T T. Cross-Sections for Gluon + Gluon $\rightarrow$ Heavy Quarkonium + Gluon. Phys. Lett., 1987, B184:257.

[122] Pumplin J, *et al.* New Generation of Parton Distributions with Uncertainties from Global QCD Analysis. JHEP, 2002, 07:012.

[123] Eidelman S, *et al.* Review of Particle Physics. Physics Letters B, 2004, 592:1+.

[124] Golonka P, Was Z. PHOTOS Monte Carlo: A Precision Tool for QED Corrections in Z and W Decays. Eur. Phys. J., 2006, C45:97–107.

[125] http://lhcb-release-area.web.cern.ch/LHCb-release-area/DOC/davinci/releases/latest/doxygen /classes.html.

[126] Gaiser J. Charmonium Spectroscopy from Radiative Decays of the J/ψ and ψ'. SLAC-0255.

[127] Needham M. Studies of Momentum Scale Calibration Using $J/\psi \to \mu^+\mu^-$. CERN-LHCB-2008-036.

[128] http://roofit.sourceforge.net/intro.html.

[129] Ferro-Luzzi M. Proposal for an Absolute Luminosity Determination in Colliding Beam Experiments Using Vertex Detection of Beam Gas Interactions. Nucl. Instrum. Meth., 2005, A553:388–399.

[130] De Lorenzi F, McNulty R, Moran D, *et al.* Indirect Luminosity Measurements with LHCb. Technical Report LHCb-PROC-2009-029. CERN-LHCb-CONF-2009-029, Sep, 2009.

[131] Anderson J, McNulty R. Luminosity Measurements at LHCb Using Dimuon Pairs Produced via Elastic Two Photon Fusion. Technical Report LHCb-2008-001. CERN-LHCb-2008-001, CERN, Geneva, Mar, 2010.

[132] Xie Y. Formalism for Simulation-based Optimization of Measurement Errors in High Energy Physics. arXiv:hep-ex/0901.3305.

Acknowledgement

I would like to give my deepest thanks to all the people who have helped me during my thesis study.

Please let me first show my sincere gratitude to my supervisor in Tsinghua University, Professor Yuanning Gao, who deserves for this. He is an insightful advisor and a fantastic friend one can ever image to have. His wide knowledge, his logical way of thinking, his great ideas are always of great value for me. I will keep forever the memories we worked together in LAL, in CERN, and in Tsinghua University, they are the biggest fortune in my life. He is such a nice and responsible person that though he was seriously ill during the days of my defense, he kept on working with me, taking care of all the arrangement, correcting my slides. I was totally moved when I knew that he was so sick that he had to go to hospital just after my defense. I will never find any words to describe my thanks to him.

As a co-tutelle student between China and France, I am indebted thanks to my French advisor Maire-Hélène Schune in Laboratoire de l'Accélérateur Linéaire. Marie-Hélène is a kind lady who you can trust whenever you meet problems. She is talent and energetic in research work, and can always give you proper suggestions when you tell her the problems. My special thanks and kudos go to all the help offered by her in dealing with different kinds of documental issues which are more troublesome for co-tutelle students. I still remember the long mail discussion about how to deal with Carte de sèjour, dormitory *etc.* Thanks, Marie-Hélène.

I owe a lot of gratitudes to Patrick Robbe, who supervises me directly in France. I am so lucky to work with a brilliant advisor and generous friend like him. He talks little, but every word he mentions turns out very helpful in latter research work or everyday life. When I look back to these days in France, there are full of memories of staying with him: working together,

discussing together, eating together and long night shifts together. All these small memories collect together and make a vivid life in LAL and CERN. And even when I was in China, he took care about my research work. During the period of thesis writing, Patrick spent a lot of time and effort in helping me with the improvement and turned the badly written thesis into the current one. Thanks, Patrick.

I would also like to thank all the committee members: Lydia Roos, thanks for accepting the invitation as the president of the committee and also thanks for all the kind helps during the three years. Olivier Schneider, thanks for being my referee and sending me feedback with most detailed corrections and interesting suggestions on the original manuscript. As the leader of flavor group where I worked in during the three years, the questions raised by him and discussions with him made the process of my study go well. Changzheng Yuan, thanks for being the referee, both for my Chinese and English thesis, his corrections are really helpful in making it more smooth.

I would also like to thank all the friends in both laboratories in China and France. These people deserve special thought: Shaomin Chen, the professor in Tsinghua group, who was my teacher in data analysis and helped me a lot during the five years. Jacques Lefrançois, Ioana Videau and Bernard Jean-Marie, the three kind elders in Orsay group, who always kindly offer their help to young guys like me. ZhenWei Yang, the young teacher who came to the laboratory in Tsinghua University nearly at the same time as me, we shared all the happiness during my thesis period. He acts like a big brother; whenever I had any problems, I could come to him asking for suggestions. Sergey Barsuk, who shared the office with me in France. He is a expert in the LHCb experiment, short discussions with him whenever I met problems are always of great help for the thesis work. He is also a good teacher in Russian, and turns me into a "Russian speaking" person. My thanks and appreciations also go to Stephane T'Jampens, Zhiqing Zhang, Yuehong Xie, Frederic Machefert, and Benoit Viaud, their sound advice and thoughful discussion deserves special mention. He Jibo, Heng Yang, Liu Bo, Li Bo, Ruan Manqi, Tian Junpin, Zhang Feng, Zhang Haibin, and Zhang Yanxi, the stay with these guys in Tsinghua Univeisity is really a happy experience. Andrey, Aurélien, Denis, Joao, Leonid, Michelle, Viktor, and Yasmine, to know and to hang up with them really made the life in Paris much colorful, especially Paris nights. They made me more involving in the western culture which are so different from the one in China. Thanks all guys, it is really my

luck to spend my thesis period with you.

I would also like to thank God to make me the luckiest guy in the world. You bring Jiashuang to my life during the hardest time of thesis writing. Her femininity made these days full of happiness and joy. Thanks, Jiashuang, for standing beside me during my defense, her constant encouragement and support turned the defense into a much more successful one.

Last but not least, I would like to thank all my family members, especially my parents, who are always there, supporting me no matter what I do and no matter how bad the situation is. I dedicate this dissertation to them.